IMPACTS OF VARYING MODEL PHYSICS ON SIMULATED STRUCTURES IN CLOUD SYSTEMS

by

Andrew Thomas Lesage

A dissertation submitted to the faculty of
The University of Utah
in partial fulfillment of the requirements for the degree of

Doctor of Philosophy

Department of Atmospheric Sciences

The University of Utah

August 2018

The University of Utah Graduate School

STATEMENT OF DISSERTATION APPROVAL

The dissertation of **Andrew Thomas Lesage**
has been approved by the following supervisory committee members:

Steven K. Krueger ,	Chair(s)	**18 Aug 2017** Date Approved
Zhaoxia Pu ,	Member	**18 Aug 2017** Date Approved
William James Steenburgh ,	Member	**18 Aug 2017** Date Approved
Adam Christopher Varble ,	Member	**18 Aug 2017** Date Approved
Robert Stoll ,	Member	**18 Aug 2017** Date Approved

by **Kevin Perry** , Chair/Dean of
the Department/College/School of **Atmospheric Sciences**
and by **David Kieda** , Dean of The Graduate School.

ABSTRACT

Three studies were performed which, in different ways, evaluated System for Atmospheric Modeling (SAM) model performance in a variety of cases: 1) CONSTRAIN, a North Atlantic marine cold air outbreak case, 2) radiative convective equilibrium (RCE) simulations, and 3) Dynamics of the Madden-Julian Oscillation (DYNAMO) shallow cumulus.

In the CONSTRAIN study, a dozen different model physics setups were used, some of which were compared with sets of runs with varying turbulence parameterization scheme and varying grid spacings. In the SHOC vs NOSHOC comparisons, the choice of parameterization scheme had little influence on runs without cloud ice. LES-scale run comparisons between the different model physics showed runs with radiation increased the precipitation and cloud cover but more precipitation reduced cloud cover causing these effects to largely cancel. Ice sedimentation increased precipitation while decreasing cloud amount and entrainment. Double-moment microphysics runs resulted in more supercooled water and less ice.

For the RCE simulation, model runs were performed varying in sea surface temperature, turbulence parameterization scheme, microphysics scheme, and grid spacing. Grid spacing had a large influence on cloud water path and SW radiation. The microphysics scheme selection had a large influence on CWP and IWP, shifting to greater CWP and less IWP in the double-moment runs. SHOC and double-moment microphysics produced a higher upper-tropospheric cloud fraction. Using radiative kernels to evaluate cloud feedbacks the runs with SHOC had a negative net cloud feedback while the single-moment NOSHOC run had a positive net cloud feedback.

For DYNAMO, shallow cumulus in calmer periods of the Madden-Julian oscillation (MJO) at Gan Island were selected as case studies based on satellite imagery, ground-based sky imagers, and combined KAZR/S-Pol radar data. Model runs at 2, 1, 0.5, and 0.1 km grid spacing were performed for the two cases. The model tended to underestimate mid-

level cloud in Case 1 and overestimate shallow cumulus in Case 2 except for the high resolution runs which overestimated shallow cumulus for both. For larger grid spacings, the observation cloud profile generally stayed within one standard deviation of the model in the lowest 4 km.

For my family, for their love and support.

CONTENTS

LIST OF FIGURES

LIST OF TABLES

ACKNOWLEDGEMENTS

CONSTRAIN runs using the M2005 microphysics were run by Peter Bogenschutz. Most of the other CONSTRAIN simulations were done by Steve Krueger. RCE runs at 0.5 km grid spacing were performed by Marat Khairoutdinov.

Research on the CONSTRAIN and RCE cases was supported by the Office of Science (BER), U. S. Department of Energy, and by the National Science Foundation Science and Technology Center for Multi-Scale Modeling of Atmospheric Processes, managed by Colorado State University under cooperative agreement No. ATM-0425247. Funding for the DYNAMO research was supported by the National Oceanic and Atmospheric Administration (NOAA) Climate Variability Program Grant NA130AR4310158.

CombRet and total sky imager data were obtained from the Atmospheric Radiation Measurement (ARM) Program sponsored by the U.S. Department of Energy, Office of Science, Office of Biological and Environmental Research, Climate and Environmental Sciences Division.

Meteosat data were obtained from the UCAR/NCAR Earth Observing Laboratory.

I acknowledge the use of Rapid Response imagery from the Land, Atmosphere Near real-time Capability for EOS (LANCE) system operated by the NASA/GSFC/Earth Science Data and Information System (ESDIS) with funding provided by NASA/HQ.

I would like to thank my committee members Professor Zhaoxia Pu, Professor W. James Steenburgh, Associate Professor Rob Stoll, Research Assistant Professor Adam Varble, and particularly my advisor Professor Steven Krueger for providing the opportunity to study and work on research at the University of Utah.

CHAPTER 1

INTRODUCTION

The grey zone is the range of grid spacing in atmospheric model simulations that lies between high resolution scales which can more adequately resolve turbulence ($<$ 1 km) to low resolution scales which require convective parameterization ($>$ 10 km). This range is critical in handling modeling questions from topics as diverse as tropical cyclones (Sun et al., 2014), stratocumulus (Boutle et al., 2014), the convective boundary layer (Shin and Hong, 2015), and the Madden-Julian Oscillation (MJO) (Wang et al., 2015). While cloud resolving models (CRMs) are able to capture more detail then global climate models (GCMs), parameterization of subgrid scale turbulence is essential through the grey zone.

Turbulence parameterization seeks to predict temporal changes in prognostic variables such as temperature, moisture, and velocity variables. Turbulence parameterization methodology has had an important role in handling clouds in atmospheric modeling. Early versions of turbulence parameterizations used a diagnostic equation to solve for K, the eddy viscosity (Pielke, 1974). Other lower order schemes which prognose the turbulent kinetic energy (TKE) equation (Khairoutdinov and Kogan, 1999) specify K as well through shear and stability profiles (Bretherton et al., 2004).

Lower-order turbulence closure schemes predict the mean variables, which are the first order moments, and use closure assumptions for the second-order moments. Second-order moments are variances and co-variances and third-order moments are used in skewness variables. Even second-moment schemes at times had difficulty with vertical transport of TKE (Yamada and Mellor, 1975). Third-moment turbulence closure schemes have been used to better represent TKE in the boundary layer and in-cloud (Krueger, 1988).

As GCMs continue to develop and shift to smaller grid spacings new approaches are being utilized. The use of a Multiscale Modeling Framework (MMF), which couples a 2-D CRM with a GCM by running the CRM at each GCM grid box (Randall et al., 2003;

Bogenschutz and Krueger, 2013), is one way to handle smaller scales in a GCM. However, these models still rely on parameterization for smaller cloud features, such as the superparameterized Community Atmospheric Model (SP-CAM) used in Bogenschutz and Krueger (2013). The higher-order turbulence closure scheme used with the SP-CAM is the Simplified Higher-Order Closure (SHOC). For at least as long as high-resolution climate scale modeling is computationally expensive for even large facilities, parameterization will remain a critical component of cumulus and turbulence impacts on simulations. Many parameterization focused intercomparison studies have been performed through the Global Energy and Water Cycle Experiment (GEWEX) Cloud System Study (GCSS) (Krueger et al., 2016). These intercomparison studies have looked at deep convection (Xu et al., 2002), continental shallow convection (Brown et al., 2002), midlatitude frontal clouds (Xie et al., 2005), and midlatitude cirrus clouds (Lin et al., 2002).

This dissertation aims to evaluate the impacts of variations in model setup in a variety of studies. There are many parameters which can be tuned in a model which can significantly alter the model output. Some of these include grid spacing, microphysics scheme, turbulence parameterization scheme, SST, and radiation scheme. There is a long-standing need for atmospheric modeling to improve at representing cloud physics, precipitation processes, and many other aspects beyond the scope of this work. Microphysics and turbulence parameterization schemes are important tools for these models; however, not all model combinations are representative in all situations. Evaluating the performance of a variety of model setups is essential to ensuring that the model can be utilized for a diverse set of meteorological situations.

The three studies in this dissertation are: 1. CONSTRAIN, a UK Met Office field campaign from which a cold air outbreak day was selected with model runs varying in model physics and grid spacing; 2. radiative convective equilibrium (RCE), 50-day simulations with a simple framework which provided for comparison of various model configurations and evaluation of radiative feedbacks with a warming SST; and 3. Dynamics of the Madden-Julian Oscillation (DYNAMO), a tropical Indian Ocean field campaign from which model runs were performed focusing on shallow cumulus.

The CONSTRAIN case is performed in two parts. The first of which is a comparison between two turbulence parameterization schemes at a variety of grid spacings to ascertain

the dependencies of turbulence scheme selection and model resolution. One of the primary goals in taking on this study was to evaluate the differences in model output based on turbulence parameterization scheme selection and since turbulence parameterizations are more important at courser grid spacings, this necessitated a range of grid spacing selections for the analysis. The second part of this study looks at a dozen different large eddy simulation (LES) scale model simulations with varying model physics such as radiation, precipitation, microphysics, and ice only/no ice configurations to identify the influence of these elements on model evaluation of the case, particularly as it relates to clouds and precipitation. Results from these LES simulations are part of a broader set of models involving other groups of researchers for an intercomparison study for this case.

The RCE case is also examined in two parts. The first uses a large number of model runs to evaluate the model dependence on turbulence parameterization scheme, SST, microphysics scheme, and grid spacing. From this assessments of precipitation, cloud fraction, and cloud radiative effect can be determined across the spectrum of model parameter combinations. The second part uses cloud radiative kernels to evaluate radiative feedbacks as a result of changing cloud patterns in a warmer climate. In climate science cloud feedbacks are one of the aspects of climate change which has the most uncertainty.

The DYNAMO case looks at two periods with shallow cumulus in the Madden-Julian Oscillation (MJO) selected through a variety of observational datasets. The observational data comes from Meteosat-7, MODIS, total sky imager, KAZR, and S-pol radar observations. Model runs for the two cases are performed and evaluated based on how realistically the model represents the clouds detected in the observations across a range of grid spacings.

The rest of this dissertation is organized as follows. Chapter 2 presents a description of the System for Atmospheric Modeling (SAM) model used in all three studies along with the SHOC turbulence parameterization scheme also used in all three. Following that will be the three main chapters, each focusing on one of the studies with background, the methodology, results, and a summary/discussion. Chapter 3 covers the CONSTRAIN cold-air outbreak case study simulations. Chapter 4 details the RCE modeling and results. Chapter 5 examines the DYNAMO case observations and model runs. Chapter 6 describes the conclusions.

CHAPTER 2

MODEL BACKGROUND

2.1 System for Atmospheric Modeling

The System for Atmospheric Modeling (SAM) was developed as a three-dimensional cloud resolving model to study cumulus convection and is described in detail in Khairoutdinov and Randall (2003). SAM uses anelastic equations of motion in the dynamical core integrated with a third-order Adams-Bashforth scheme. Variables are staggered on an Arakawa C grid. The advection is handled with a three-dimensional positive definite monotonic scheme (Smolarkiewicz and Grabowski, 1990).

Radiation in SAM can be treated in either a specified or interactive framework. Interactive radiation in SAM is handled with either the Community Atmospheric Model (CAM) (Collins et al., 2004) radiation (Kiehl et al., 1998) or the Rapid Radiative Transfer Model (RRTM) (Mlawer et al., 1997; Iacano et al., 2008) schemes from the National Center for Atmospheric Research (NCAR) Community Climate System Model (CCSM). Radiative transfer in CAM is computed for each grid column using simulated cloud water and cloud ice to determine optical and cloud radiative properties (Kiehl et al., 1998). In RRTM a correlated *k*-distribution is used to closely represent line-by-line results (Mlawer et al., 1997).

Microphysics in SAM uses either the original SAM single-moment microphysics scheme (Khairoutdinov and Kogan, 2000) or the Morrison double-moment microphysics scheme (Morrison et al., 2005). The single-moment microphysics is a bulk microphysics scheme with prognostic equations for water/ice moist static energy, total water, and precipitating water. Condensed water phases are diagnosed based on temperature. Single-moment SAM microphysics does not allow for supercooled water. For double-moment microphysics, the Morrison scheme prognoses both the mixing ratios and number concentration for cloud ice, rain, snow, and graupel in addition to the number concentration for cloud water. More prognostic equations are used for processes such as freezing, melting, riming,

and collection. The double-moment scheme also allows for supercooled water.

The model has periodic lateral boundary conditions. The Monin-Obukhov similarity theory is used for the surface fluxes. SAM has incorporated ISCCP, MODIS, and MISR cloud simulators (Klein and Jakob, 1999) with ISCCP simulator results used in this study.

For the turbulence closure scheme SAM comes with two options in the original, a 1.5-order closure using a prognostic equation for the subgrid-scale turbulent kinetic energy (SGS TKE) (Khairoutdinov and Kogan, 1999), and a simple Smagorinsky closure (Khairoutdinov and Randall, 2003). The former is used throughout this dissertation and will be referred to as NOSHOC. These low-order closure models use "all-or-nothing" condensation where the grid box must be saturated throughout for cloud to form and the grid box can only be either completely cloudy or completely clear.

SAM is used in all three studies in this dissertation. SAM is run at LES scales as 100 m grid spacing runs in the CONSTRAIN and DYNAMO cases. SAM is run at Cloud-Resolving Model (CRM) scales (500 m - 2 km) in CONSTRAIN, RCE, and DYNAMO. Additionally, runs with larger grid spacings in the grey zone between CRM and Global Climate Model (GCM) scales are performed in CONSTRAIN and RCE.

2.2 Simplified Higher-Order Closure

A third closure scheme was added to SAM, by Peter Bogenschutz, called the Simplified Higher-Order Closure (SHOC) which is detailed in Bogenschutz and Krueger (2013). Similar to the NOSHOC method, SHOC also prognoses SGS TKE. A joint PDF is used to diagnose SGS condensation and SGS buoyancy flux (Golaz et al., 2002a). The joint PDF is based on vertical velocity, liquid water potential temperature, and total water mixing ratio. The PDF shape is assumed to be an Analytic Double Gaussian 1 PDF (Golaz et al., 2002b). Double Gaussian PDFs have been shown to fit cloud layers better for course-grid models than alternatives tested which included Single Delta Functions, Double Delta Functions, Single Gaussians, Lewellen-Yoh, and Analytic Double Gaussian 2 PDFs (Larson et al., 2002; Bogenschutz et al., 2010).

NOSHOC does not diagnose SGS condensation. NOSHOC diagnoses SGS buoyancy flux from the moist Brunt-Väisälä frequency. SHOC uses the diagnostic second-moment closure of Redelsperger and Sommeria (1986) and the diagnostic closure for the third

moment of vertical velocity from Canuto et al. (2001). Unlike standard SAM, SHOC does not use an all-or-nothing approach for cloud cover, but instead can have partly cloudy grid boxes.

A key difference between NOSHOC and SHOC is in the handling of the turbulence length scale which is the size of the largest turbulent eddies that affect a given location. In NOSHOC, the turbulence length scale is proportional to vertical grid size. Bogenschutz and Krueger (2013) note that having a turbulence length scale set to the vertical grid spacing is appropriate for high resolution simulations where the grid size is in the inertial subrange. However, when the turbulence length scale is too large, SGS TKE gets underestimated and resolved TKE overestimated. In SHOC, the turbulence length scale is instead related to SGS TKE and eddy length scales which have been shown to be effective for the convective boundary layer (Teixeira and Cheinet, 2004). Eddy diffusion schemes have been shown to perform well when the SGS TKE profile can be predicted (Cheng et al., 2010).

SHOC was designed in order to improve model representation of the SGS TKE. It was utilized for trade-wind cumulus, stratocumulus, stratocumulus to cumulus transition, and continental cumulus cases (Bogenschutz and Krueger, 2013). In those cases the parameterization scheme was able to better represent buoyancy flux and dissipation rates along with reducing sensitivity to horizontal grid spacing. SHOC is computationally inexpensive compared to other higher-order turbulence closure schemes, Utility at larger grid spacings relative to the default scheme in SAM would further increase savings on computational expense.

In the CONSTRAIN and RCE studies both NOSHOC and SHOC are used and compared against each other in evaluating model runs at larger grid spacings while in the DYNAMO study only SHOC is used as the turbulence parameterization scheme. The CONSTRAIN and RCE analysis will further test the viability of SHOC as a suitable option for turbulence parameterization.

CHAPTER 3

CONSTRAIN

3.1 Background

Marine cold air outbreaks are a common feature in higher latitudes of both the Northern and Southern Hemisphere. A cold air outbreak involves a polar or cold continental air mass being advected into an area with a warmer ocean (Brümmer, 1996; Fletcher et al., 2016a). Cold air outbreak cases have been shown to have convection morph from organized rolls to open cellular convection, which can have significant impacts on transport of heat and moisture (Brümmer, 1999; Brümmer and Pohlmann, 2000).

A climatology of marine cold air outbreaks shows that they are more frequent in the Southern Hemisphere but stronger in the Northern Hemisphere (Fletcher et al., 2016a). That study found that the stronger events tended to be in the cold air region of extratropical cyclones. Additionally, surface fluxes, fueled by the cold air advecting over comparatively warmer waters, cause the boundary layer to deepen, warm, and moisten during a marine cold air outbreak. The clouds in marine cold air outbreaks were generally at low altitude and a high cloud fraction (Fletcher et al., 2016b).

A common mixed-phase cloud structure in the Arctic is a supercooled liquid cloud that precipitates ice (Hobbs and Rangno, 1998). These cloud layers can collapse with rapid ice precipitation though can maintain a steady-state with the right temperature, ice concentration, and ice crystal habit (Harrington et al., 1999; Avramov and Harrington, 2010).

A lack of liquid water content and excessive conversion of liquid to ice has been found in Arctic stratus cases (Morrison and Pinto, 2006; Klein et al., 2009). In the Morrison and Pinto study the more complex microphysics parameterization was able to better represent the mixed-phase stratus while the simpler schemes had an overabundance of ice rather than supercooled water. The Klein et al. paper covers the intercomparison project for the Atmospheric Radiation Measurement (ARM) Mixed-Phase Arctic Cloud Experiment

(M-PACE) for which most of the 17 single-column models and 9 cloud-resolving models significantly underestimated liquid water path. A sensitivity test removing cloud ice indicated that mixed-phase interactions were primarily the cause of this underestimation. Similar to the Morrison and Pinto study, the more complex microphysics models were more likely to be closer to representing liquid water reasonably.

Much like the Arctic cold air outbreak studies, Southern Ocean modeling often underestimates postfrontal low and midlevel clouds in the marine boundary layer (Huang et al., 2014). The Southern Ocean experiences even larger rates of supercooled liquid water and mixed-phase clouds than the oceans of the extratropical Northern Hemisphere (Morrison et al., 2011). Low ice nuclei concentrations in the Southern Ocean due to less land influence in the Southern Hemisphere than the Northern Hemisphere likely explains this increased prevalence of supercooled liquid water (Burrows et al., 2013; Chubb et al., 2013).

The Grey Zone Project was designed to explore model behavior with and without convective parameterization at grid spacings throughout the grey zone in order to better understand model performance. A case study selected for intercomparison is from CONSTRAIN, a Met Office field campaign in January 2010 over the North Atlantic ocean. The specific day selected is a cold air outbreak event on 31 January 2010. The case is 14.5 hrs in duration with initial conditions and forcings generated from a high resolution limited area model simulation (LAM) performed by Paul Field on the Met Office Unified Model (UM) (Field et al., 2014). This run was a quasi-lagrangian LES where the domain was advected from 66 °N 11 °W to 60 °N 8.7 °W to simulate a transition from stratocumulus to cumulus. The surface is forced with an increasing SST throughout the simulation. The first 1.5 hrs of the simulation are a spin-up period.

Model simulations for this event have been compared to aircraft, satellite, and radar observations (Field et al., 2014; McBeath et al., 2014). In the Field et al. (2014) study their control run was unable to represent the stratiform cloud cover region with sufficient cloud cover, though an adjustment for the shear-dominated boundary layer allowing for mixing into regions of weak static stability was able to match the 100% cloud coverage in the stratus region of the observations. Aircraft found much higher liquid water and ice water contents in the 2.0-2.7 km altitude range than their control run, with only their no ice run able to come close for liquid water content.

3.2 Methodology

For the CONSTRAIN case, SAM runs using the standard SAM 1.5-order turbulence closure (NOSHOC) at 0.1 km grid spacing were used as an LES scale equivalent baseline run for each set of model physics. From there, many other runs were performed, outlined in Table 3.1 and Table 3.2 for NOSHOC and SHOC, respectively. Sets of runs at varying grid resolution with NOSHOC were run for full physics, no radiation, and no ice configurations. Sets of runs with SHOC were performed for full physics, no radiation, no ice, ice only, no ice sedimentation, and no ice/sedimentation/precipitation configurations. Additional runs were performed as listed in the tables. Most of these simulations were run by Steve Krueger. Peter Bogenschutz ran LES and 3 km SHOC and NOSHOC simulations for the Morrison double-moment microphysics scheme (referred to in this chapter as M2005). The model physics for all of the model physics configurations is shown in Table 3.3.

The model dimensions for NOSHOC CONSTRAIN runs are shown in Table 3.4. Horizontal domains were set to 96 km for 0.5, 1, and 3 km grid spacing runs. For the 30 km runs, a domain of 960 km was used and for 0.1 km runs a domain of either 32 km or 64 km was used. Grid spacing in the vertical at low levels is 50 m or lower for the LES scale runs of 0.1 km grid spacing in the horizontal and 100 m for the runs with larger horizontal grid spacing. LES scale runs mostly used either 89 or 128 vertical levels while the runs with higher horizontal grid spacing had 47 or 67 vertical levels.

The model dimensions for SHOC CONSTRAIN runs are shown in Table 3.5. All SHOC runs have a 100 m vertical grid spacing in the lowest levels and either 47 or 67 vertical levels. SHOC runs have horizontal domains of 96 km except for the runs with larger than a 3 km horizontal grid spacing. Those runs have a domain expanded to fit 32 grid points in the horizontal.

3.3 Results

3.3.1 Grid Spacing and SHOC

From the large variety of model physics, four of the configurations have been selected to highlight the effects of grid spacing and SHOC vs NOSHOC in the model runs. The sets of runs selected are the double-moment microphysics, the single-moment no ice runs with and without SHOC, and the single-moment no ice sedimentation runs.

Model results for these sets of runs for cloud water path + ice water path (CWP+IWP) are shown in Figure 3.1. For the M2005 runs (Figure 3.1a), the LES run shows a higher CWP+IWP than the 3 km runs for most of the model period until the final two hours when the 3 km runs are higher. There is very little difference between the 3 km runs despite the differing turbulence parameterization schemes. For the no ice runs with and without SHOC (Figure 3.1b,d) the CWP trends are similar for the LES, SHOC, and NOSHOC runs with the exception of the 3 km NOSHOC run. The LES run without ice sedimentation (Figure 3.1c) stays fairly level while the SHOC runs start out higher than the LES after spin-up and eventually decline to lower values than the LES. The SHOC runs without ice sedimentation have similar CWP + IWP for the three different grid spacings.

Plots of surface precipitation rate are shown in Figure 3.2. For the M2005 runs (Figure 3.2a) the surface precipitation rate is similar for all three runs the first 10 hours. The LES surface precipitation rate rises more sharply than the 3 km runs afterwards before dropping in the final hour. For the no ice runs (Figure 3.2b,d) there is a sizable disparity with grid spacing regardless of turbulence parameterization scheme. Among the no ice runs the LES and 0.5 km SHOC and NOSHOC runs have the highest surface precipitation rates and the 1 km SHOC and NOSHOC runs the lowest. The 3 km and SHOC 8 km runs have surface precipitation rates in between. The differences between SHOC and NOSHOC no ice runs are small despite the large changes in surface precipitation rates with grid spacing. For the no ice sedimentation runs (Figure 3.2c) the surface precipitation rate is higher for the 1 km and 3 km SHOC runs than the 0.5 km and LES runs for the first 12 hours, after which the smaller grid spacing runs catch up to and pass the larger grid spacing runs.

Cloud fraction results are shown in Figure 3.3. For the M2005 (Figure 3.3a) LES run the skies are overcast while there is slightly less cloud cover for the 3 km SHOC run and roughly 80% cloud cover for the 3 km NOSHOC run. No ice SHOC runs (Figure 3.3b) have overcast or close to it conditions throughout the duration of the run. The largest grid spacing run, 8 km, has the lowest cloud fraction later in the run. The no ice runs without SHOC (Figure 3.3d) are similar to the SHOC runs except the 3 km run cloud fraction drops early on in the run and rebounds towards the end of the run. The runs without ice sedimentation (Figure 3.3c) experience a decreasing cloud fraction over time

with the larger grid spacing runs maintaining overcast conditions later though eventually track close to the LES run.

The mean inversion height is derived in the model as the average height level of the maximum vertical potential temperature gradient. Model output for this variable is shown in Figure 3.4. In these four model physics setups the initial inversion height is just below 1.5 km and ends between 2.4 km and 3.1 km. The 3 km SHOC run for M2005 (Figure 3.4a) had slightly lower inversion heights than the 3 km NOSHOC and the LES runs. No ice SHOC runs (Figure 3.4b) were highly clumped together while NOSHOC runs (Figure 3.4d) had a larger grid spacing dependence with a lower inversion height for the runs with a larger grid spacing. No sedimentation runs (Figure 3.4c) had a higher inversion height with larger grid spacing though the three SHOC runs were all close together.

While there is little difference between SHOC and NOSHOC for runs without ice, this pattern does not remain the case for runs that contain both cloud water and cloud ice. Results for SHOC and NOSHOC full physics runs are shown in Figure 3.5. The LES run is marked the same on both panels. The SHOC run at 0.5 km resolution is similar to the LES run, albeit higher in cloud fraction, but the 1 km and 3 km SHOC runs start out with overcast conditions before transitioning to coverage similar to the LES run (Figure 3.5a). In the NOSHOC full physics runs, all of the runs are fairly similar shape to each other throughout the model period with slightly higher cloud fractions at larger grid spacings (Figure 3.5b).

Last hour average profiles of the total cloud water + ice (QN) are shown in Figure 3.6. The last hour was used in order to be a maximum distance away from the model spin-up period. The altitude of the maximum QN is slightly below the inversion height for all of the model setups. For the M2005 runs (Figure 3.6a) the magnitude of QN is slightly higher for the 3 km SHOC run than the 3 km NOSHOC or the LES runs. For the no ice runs (Figure 3.6b,d) the magnitude of QN is very similar for both SHOC and NOSHOC runs except for lower values in the SHOC 8 km and NOSHOC 3 km runs. For the no sedimentation runs (Figure 3.6c) the SHOC runs have a lower QN than the LES.

Turbulent kinetic energy (TKE) is comprised of resolved and subgrid-scale (SGS) components. NOSHOC has a turbulence length scale based on the vertical grid size while SHOC bases the turbulence length scale on the large-eddy scale and SGS TKE. Resolved

TKE final-hour averaged profiles for the model setups are shown in Figure 3.7. In all model setups (with the exception of 1 km no ice runs at higher altitude) the total TKE increases with increased grid spacing. The maximum values of TKE are at the surface and at the QN maximum. Above the cloud layer TKE drops off significantly.

SGS TKE final-hour mean profiles are shown in Figure 3.8. SGS TKE increases with grid spacing, as expected, for most runs, though there is less of an increase for NOSHOC no ice runs. When SGS TKE is a small fraction of the total TKE this reduces the importance of how SHOC and NOSHOC handle the turbulence length scale.

3.3.2 LES Comparisons

In total, 12 different model physics configurations were used at 0.1 km LES grid sizes. All of these varying setups are compared to each other below for cloud fraction, precipitation, and TKE in Figure 3.9. For cloud fraction (Figure 3.9a) the LES configurations which had overcast skies for the final hour mean profile were the no ice run (green) and the M2005 microphysics run (purple) which ended up having almost no ice. The ice only/no sedimentation run (dark blue) and the no sedimentation run (pink) had similar profiles with a maximum cloud fraction around .4 at roughly 2.25 km altitude. The full physics run (black) and no radiation run (fuschia) had virtually identical profiles with smaller cloud fractions lower in the atmosphere. The configurations with the shallowest cloud maxima were the no precipitation (red), no radiation or precipitation (yellow) and ice only (light blue) runs.

For precipitation flux (Figure 3.9b) the models split into two main categories. One of these has precipitation flux maxima just below 2 km which included the no ice, the M2005 microphysics, and no sedimentation runs. The other has precipitation flux maxima closer to 1 km which are the full physics, no radiation runs and ice only runs. Despite the large differences in maximum precipitation flux, the surface precipitation flux is much closer for the seven model runs than at other altitudes.

Total TKE (Figure 3.9c) shows patterns similar to the cloud fraction and precipitation flux. The six runs with cloud fraction maxima between 2-3 km, runs with no ice, no ice sedimentation, or virtually no ice (M2005), have a local max of total TKE co-located with their cloud fraction maximum. However, for all runs except for no ice, the highest total

TKE value is at the lowest model level. Total TKE drops off towards 0 above cloud top while staying elevated at lower levels, including the no cloud run (orange) which is the first to drop off towards 0. SGS TKE (Figure 3.9d) shows a similar pattern to total TKE for most of the model runs except the magnitude of SGS TKE is a minute fraction of the total. Two notable exceptions are the no cloud/radiation/precipitation run which has the largest low-level SGS TKE despite having the smallest low-level total TKE and the M2005 microphysics run which has the lowest low-level SGS TKE despite having the highest low-level total TKE.

LES comparisons looking at the effects of radiation and precipitation are shown in Figure 3.10. Surface precipitation rates were roughly 0.5 mm d^{-1} higher in the full physics run than the run without radiation (Figure 3.10a). Despite the 50% gap in precipitation the difference in the CWP + IWP (Figure 3.10b) and cloud fraction (Figure 3.10c) between the full physics and no radiation runs was small. When precipitation is turned off the run with radiation escalates in CWP + IWP much faster than the no radiation variant and shows an increase in cloud fraction while the no radiation variant has a declining trend the last 9 hours of the run. Runs without precipitation had much higher CWP + IWP and cloud fractions than the equivalent runs with precipitation.

Effects of cloud ice and ice sedimentation for LES runs are shown in Figure 3.11 and Figure 3.12. The surface precipitation rate was higher for the runs which allow ice sedimentation than those which do not (Figure 3.11a). The difference between the runs with both liquid and ice and those with ice only were small in the latter 10 hours of the run regardless of ice sedimentation. The inversion height was higher for the runs without sedimentation than those with sedimentation (Figure 3.11b). A gap developed between the full physics and ice only runs with sedimentation that does not exist in the equivalent runs without sedimentation.The full physics run has a higher cloud fraction and QN than the ice only run at a higher altitude (Figure 3.12a,b). The runs without ice sedimentation had much higher cloud fractions with a maximum at roughly 2.25 km altitude. Total TKE was higher throughout the entire profile for the no ice sedimentation runs, which shows these runs have higher entrainment than the runs which allow for ice sedimentation (Figure 3.12c).

The effects of the microphysics scheme selection along with additional no ice and no

ice sedimentation choices on LES runs is shown in Figure 3.13. Surface precipitation rate increases faster in the full physics and no ice sedimentation runs; however, the M2005 microphysics run has the highest surface precipitation rate of the four towards the end of the run (Figure 3.13a). The no ice run is the slowest to develop precipitation. The microphysics scheme makes a significant difference in IWP as the M2005 run only develops a minute fraction of IWP relative to the single-moment full physics run (Figure 3.13b). Instead of ice the M2005 run is producing supercooled water. CWP + IWP stays lower for the runs with higher precipitation and is highest for the no ice run (Figure 3.13c). Inversion height generally trends upward over time though is much slower for the full physics run which decreases slightly in inversion height the first five hours (Figure 3.13d). The runs with less ice resulted in more clouds and higher entrainment while the runs with more ice had higher precipitation and fewer clouds which resulted in less entrainment.

3.4 Summary and Discussion

For the CONSTRAIN cold air outbreak case, model simulations were performed with 12 different model physics setups at an LES-scale grid spacing of 100 m. Runs with and without SHOC were performed at larger grid spacings to look at dependence of turbulence parameterization scheme and grid size.

This case was based on an LES which simulated a transition from stratocumulus to cumulus clouds. However, most model runs either decreased in cloud fraction substantially shortly after the simulation began (NOSHOC full physics or ice only, latter not shown) or maintained overcast or near overcast conditions throughout the simulation (no ice and the LES run of M2005). The no sedimentation runs and lower resolution full physics SHOC runs show a steady decrease to just below half coverage by the end of the run.

In the CONSTRAIN runs, the choice of turbulence parameterization scheme mattered little for no ice and M2005 runs which contained extremely little ice. The small differences between SHOC and NOSHOC for runs without ice (no ice and M2005) suggests that turbulence parameterization scheme is less impactful when only liquid water clouds (including supercooled water) are present.

However, this result did not carry over to runs with both cloud liquid and ice. For full physics runs, the choice of SHOC vs NOSHOC significantly changed cloud fraction

and other variables (not shown). The large differences between SHOC and NOSHOC full physics runs with both liquid water clouds and cloud ice makes it likely that ice processes are responsible for significant differences between the two parameterization schemes.

For the process-denial runs radiation increased the precipitation and clouds in the simulations; however, since runs with precipitation decreased clouds, these two influences largely cancel when comparing cloud fraction for precipitation-allowing runs with and without radiation. Runs with ice sedimentation had higher precipitation but less cloud cover and entrainment. The full physics runs with single-moment microphysics produced cloud ice while the run with double-moment microphysics produced supercooled water instead, a more realistic result for a North Atlantic cold air outbreak case.

The no ice runs and M2005 runs behaved similarly to their equivalents in other studies. In Field et al. (2014) the CWP in observations was most closely matched by their no ice run. The no ice runs in this study had the highest CWP+IWP values among the model runs tested by a large margin with M2005 being the next highest. M2005 was also effectively a no ice run due to it holding on to supercooled water rather than converting too much to ice as the single-moment runs did. It has been shown in other intercomparisons that the more complicated microphysics schemes are better able to maintain supercooled water (Morrison and Pinto, 2006; Klein et al., 2009), a pattern with which the M2005 results are consistent. While this study only used one single-moment microphysics scheme and only one double-moment microphysics scheme, the similarity in results here when it comes to supercooled water compared to other studies suggests that these models are likely representative of single-moment and double-moment microphysics schemes generally.

Table 3.1. NOSHOC model simulations performed for the CONSTRAIN case study.

	NOSHOC				
Grid Spacing	30 km	3 km	1 km	.5 km	.1 km
Full Physics	x	x	x	x	x
No Prec.					x
No Rad.	x	x	x	x	x
No Rad./Prec.					x
No Ice		x	x	x	x
Ice Only					x
Ice Only, No Sed.					x
No Sed.					x
Ice Only, No R/S/P					x
No Cloud/R/P					x
No Ice/R/P					x
M2005		x			x

Table 3.2. SHOC model simulations performed for the CONSTRAIN case study.

	SHOC					
Grid Spacing	30 km	8 km	4 km	3 km	1 km	.5 km
Full Physics	x			x	x	x
No Prec.					x	x
No Rad.	x			x	x	x
No Ice	x	x		x	x	x
Ice Only	x			x	x	x
No Sed.				x	x	x
Ice Only, No R/S/P		x	x		x	
M2005				x		

Table 3.3. Model physics (microphysics, radiation, cloud, precipitation, liquid water, ice, and ice sedimentation) for each set of runs for the CONSTRAIN case study.

Model Setup	Micro.	Rad.	Cloud	Precip.	Liq. Water	Ice	Ice Sed.
Full Physics	1M	Yes	Yes	Yes	Yes	Yes	Yes
No Prec.	1M	Yes	Yes	No	Yes	Yes	Yes
No Rad.	1M	No	Yes	Yes	Yes	Yes	Yes
No Rad./Prec.	1M	No	Yes	No	Yes	Yes	Yes
No Ice	1M	Yes	Yes	Yes	Yes	No	No
Ice Only	1M	Yes	Yes	Yes	No	Yes	Yes
Ice Only, No Sed.	1M	Yes	Yes	Yes	No	Yes	No
No Sed.	1M	Yes	Yes	Yes	Yes	Yes	No
Ice Only, No R/S/P	1M	No	Yes	No	No	Yes	No
No Cloud/R/P	1M	No	No	No	No	No	No
No Ice/R/P	1M	No	Yes	No	Yes	No	No
M2005	2M	Yes	Yes	Yes	Yes	Yes	Yes

Table 3.4. Model dimensions for the NOSHOC CONSTRAIN runs with grid spacing (dx, dz) and number of grid points (nx, nz) in the horizontal and vertical.

Physics	dx	nx	dz	nz
Full Physics	0.1 km	640	50 m	128
Full Physics	0.5 km	192	100 m	67
Full Physics	1 km	96	100 m	67
Full Physics	3 km	32	100 m	67
Full Physics	30 km	32	100 m	67
No Prec.	0.1 km	320	50 m	128
No Rad.	0.1 km	320	50 m	89
No Rad.	0.5 km	192	100 m	47
No Rad.	1 km	96	100 m	47
No Rad.	3 km	32	100 m	47
No Rad.	30 km	32	100 m	47
No Rad./Prec.	0.1 km	320	50 m	89
No Ice	0.1 km	640	50 m	128
No Ice	0.5 km	192	100 m	67
No Ice	1 km	96	100 m	67
No Ice	3 km	32	100 m	67
Ice Only	0.1 km	640	50 m	128
Ice Only, No Sed.	0.1 km	320	50 m	128
No Sed.	0.1 km	640	50 m	128
Ice Only, No R/S/P	0.1 km	640	50 m	128
No Cloud/R/P	0.05 km	640	50 m	128
Ice/R/P	0.1 km	640	50 m	128
M2005	0.1 km	960	25 m	212
M2005	3 km	96	100 m	67

Table 3.5. Model dimensions for the SHOC CONSTRAIN runs with grid spacing (dx, dz) and number of grid points (nx, nz) in the horizontal and vertical.

Physics	dx	nx	dz	nz
Full Physics	0.5 km	192	100 m	67
Full Physics	1 km	96	100 m	67
Full Physics	3 km	32	100 m	67
Full Physics	30 km	32	100 m	67
No Prec.	0.5 km	192	100 m	67
No Prec.	1 km	96	100 m	67
No Rad.	0.5 km	192	100 m	47
No Rad.	1 km	96	100 m	47
No Rad.	3 km	32	100 m	47
No Rad.	30 km	32	100 m	47
No Ice	0.5 km	192	100 m	67
No Ice	1 km	96	100 m	67
No Ice	3 km	32	100 m	67
No Ice	8 km	32	100 m	67
No Ice	30 km	32	100 m	67
Ice Only	0.5 km	192	100 m	67
Ice Only	1 km	96	100 m	67
Ice Only	3 km	32	100 m	67
Ice Only	30 km	32	100 m	67
No Sed.	0.5 km	192	100 m	67
No Sed.	1 km	96	100 m	67
No Sed.	3 km	32	100 m	67
Ice Only, No R/S/P	1 km	96	100 m	67
Ice Only, No R/S/P	4 km	32	100 m	67
Ice Only, No R/S/P	8 km	32	100 m	67
M2005	3 km	32	100 m	67

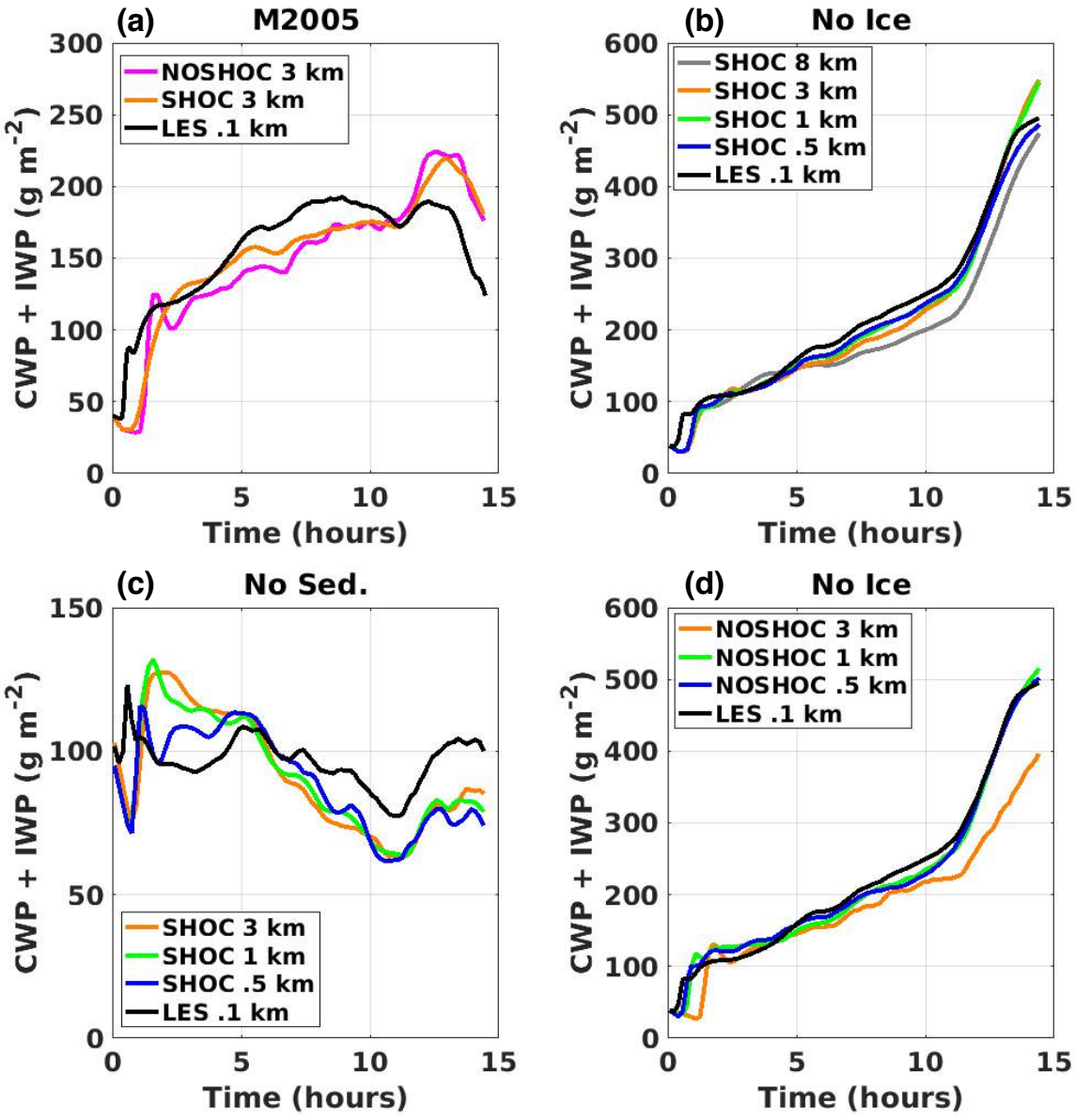

Figure 3.1. Cloud water path + ice water path time series for a) M2005 microphysics, b) no ice SHOC, c) no sedimentation, and d) no ice NOSHOC model runs.

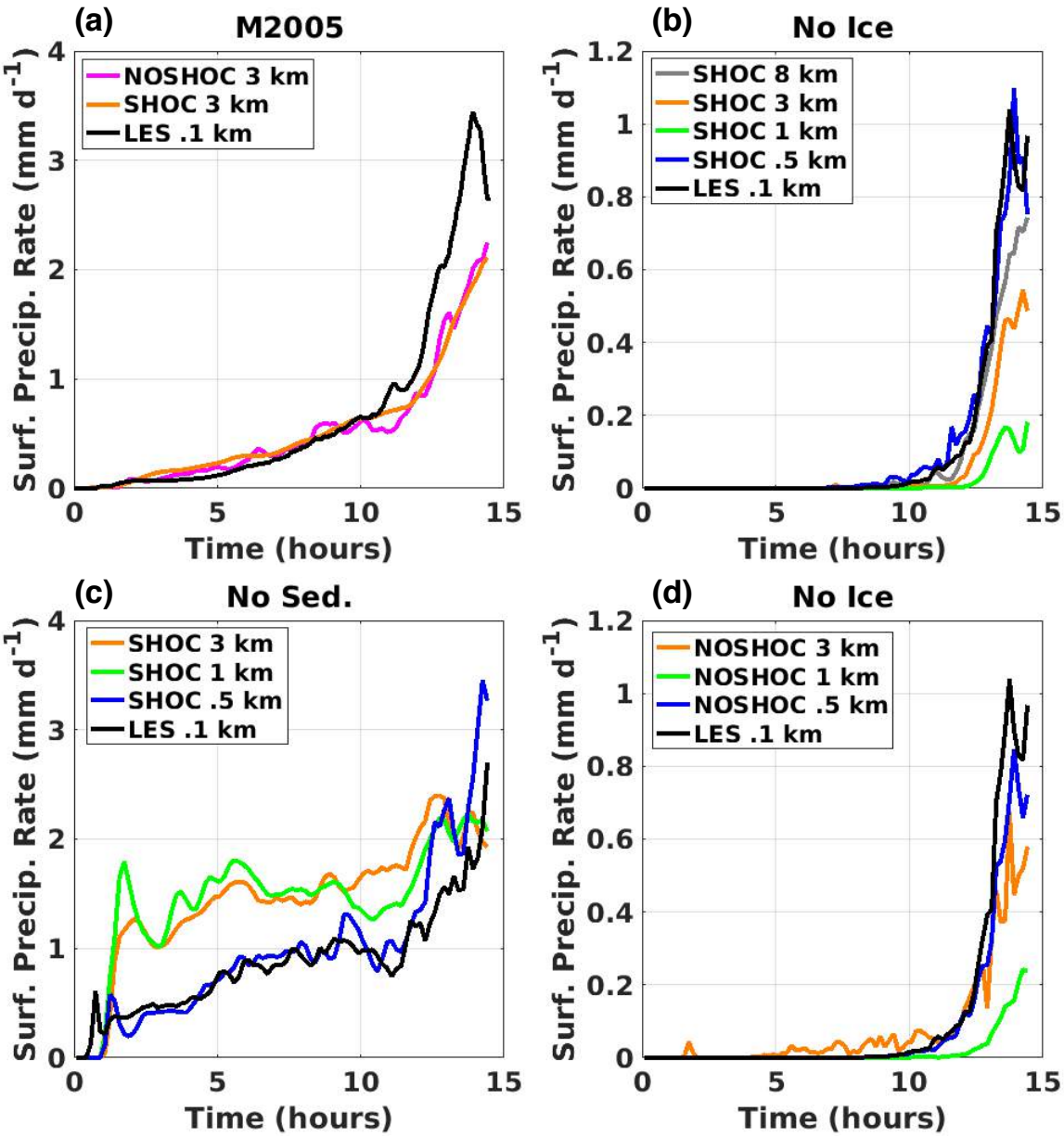

Figure 3.2. Surface precipitation rate time series for a) M2005 microphysics, b) no ice SHOC, c) no sedimentation, and d) no ice NOSHOC model runs.

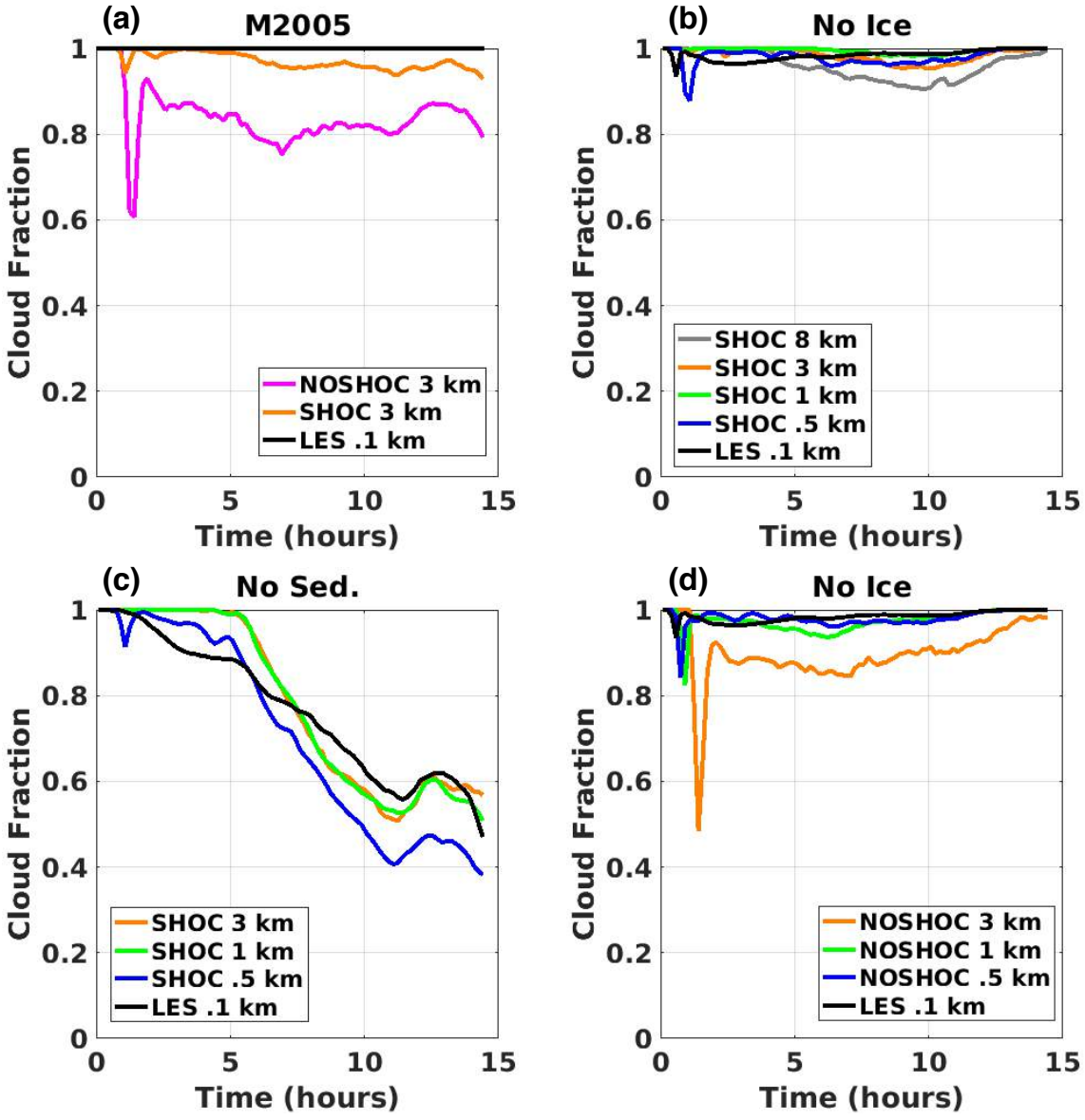

Figure 3.3. Cloud fraction time series for a) M2005 microphysics, b) no ice SHOC, c) no sedimentation, and d) no ice NOSHOC model runs.

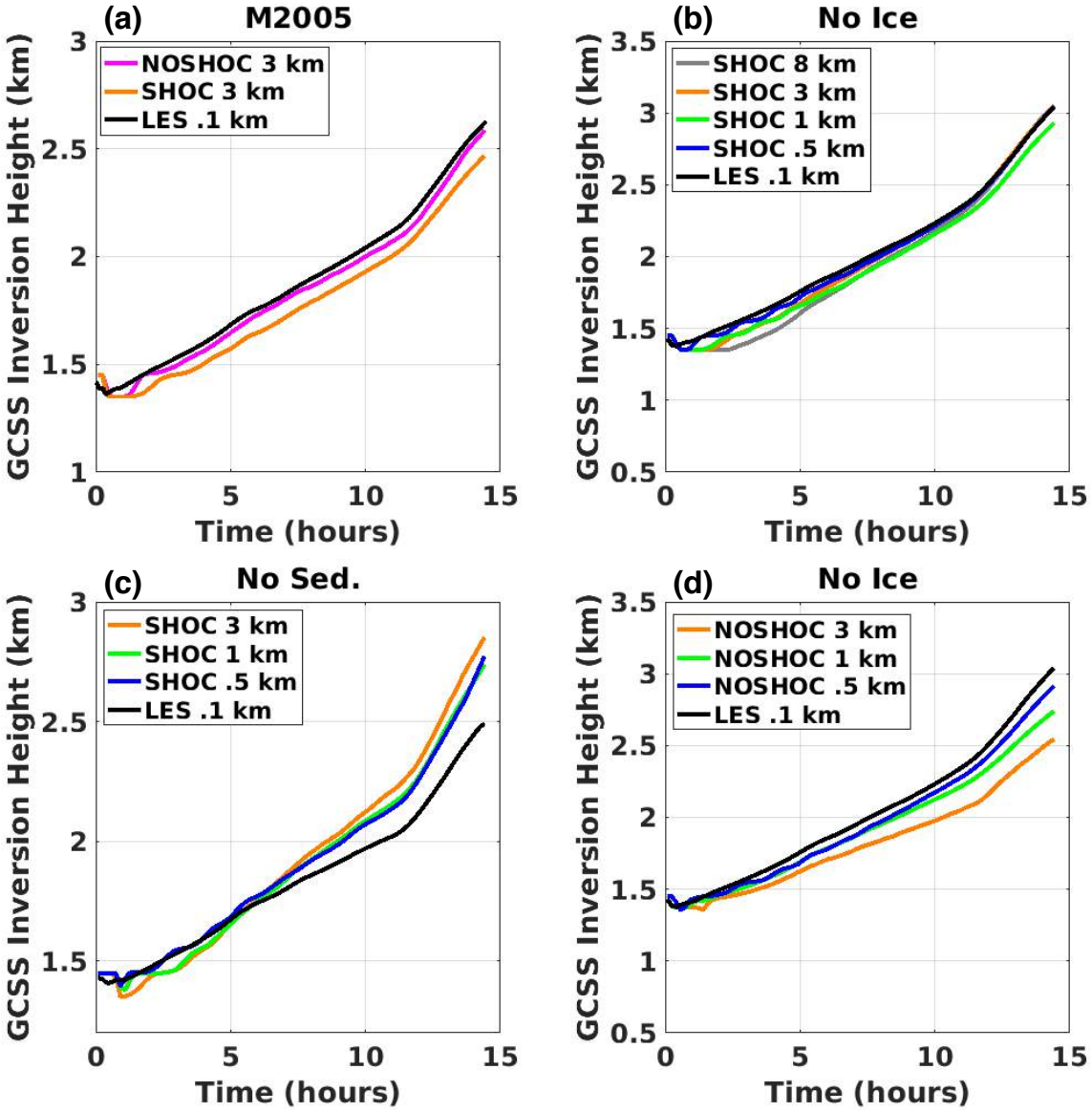

Figure 3.4. Inversion height time series for a) M2005 microphysics, b) no ice SHOC, c) no sedimentation, and d) no ice NOSHOC model runs.

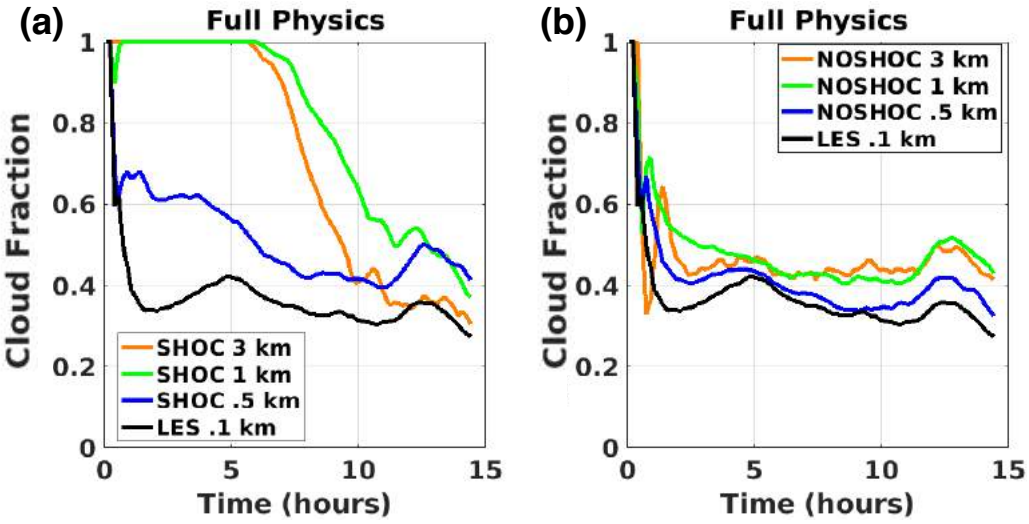

Figure 3.5. Cloud fraction time series for a) SHOC full physics and b) NOSHOC full physics model runs.

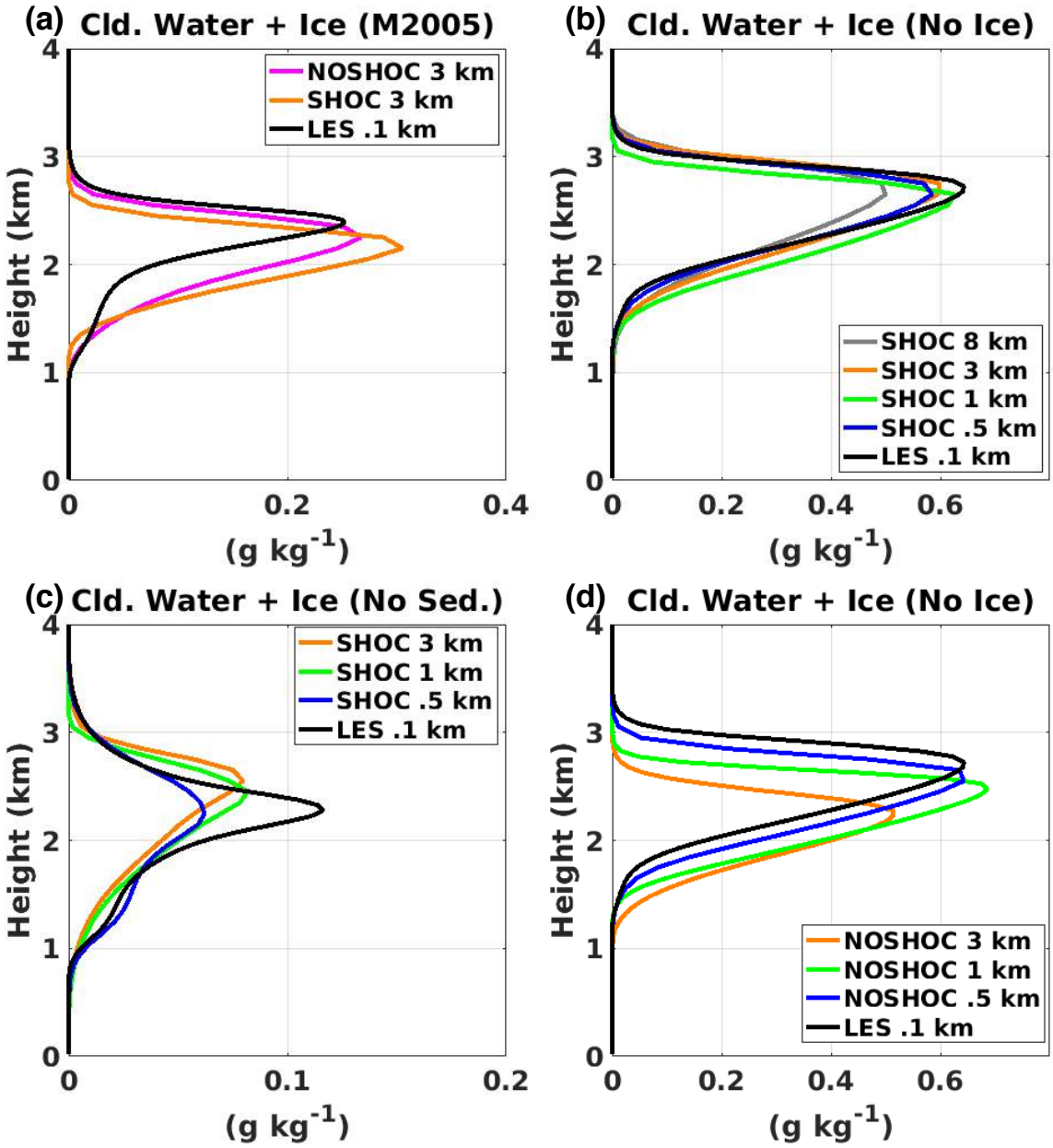

Figure 3.6. Cloud water + ice final hour mean profiles for a) M2005 microphysics, b) no ice SHOC, c) no sedimentation, and d) no ice NOSHOC model runs.

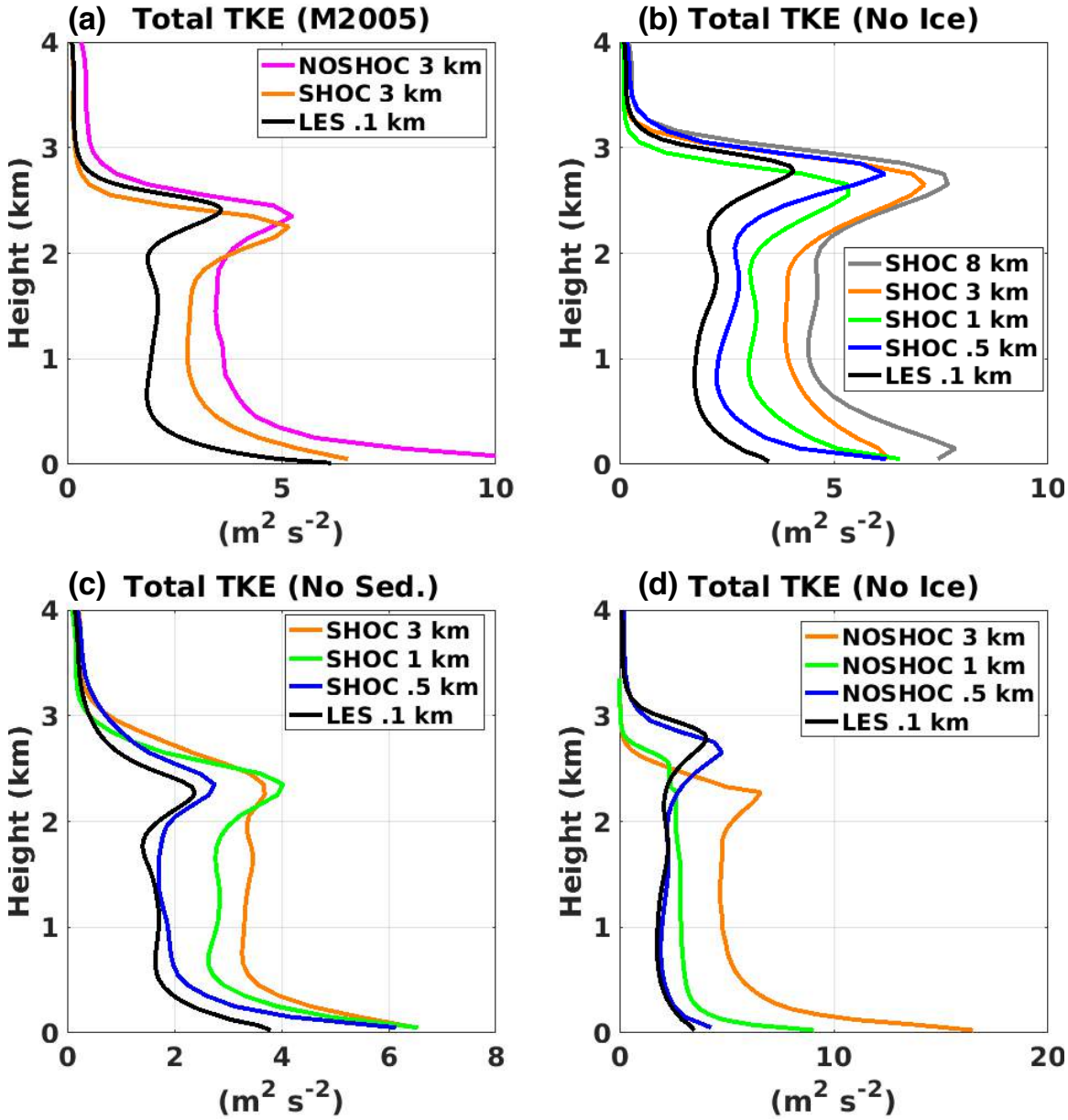

Figure 3.7. Total turbulent kinetic energy final hour mean profiles for a) M2005 microphysics, b) no ice SHOC, c) no sedimentation, and d) no ice NOSHOC model runs.

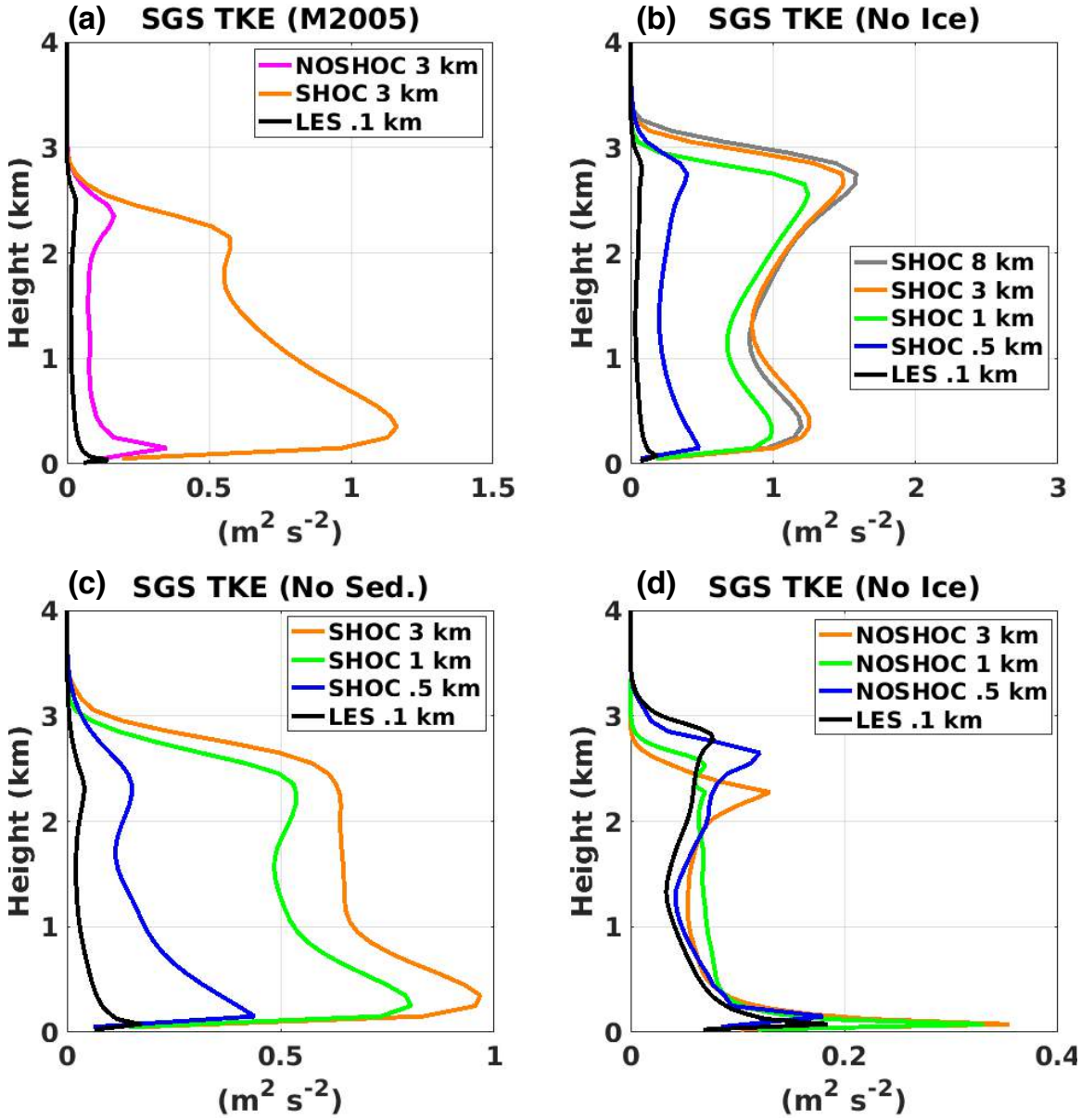

Figure 3.8. Subgrid scale turbulent kinetic energy final hour mean profiles for a) M2005 microphysics, b) no ice SHOC, c) no sedimentation, and d) no ice NOSHOC model runs.

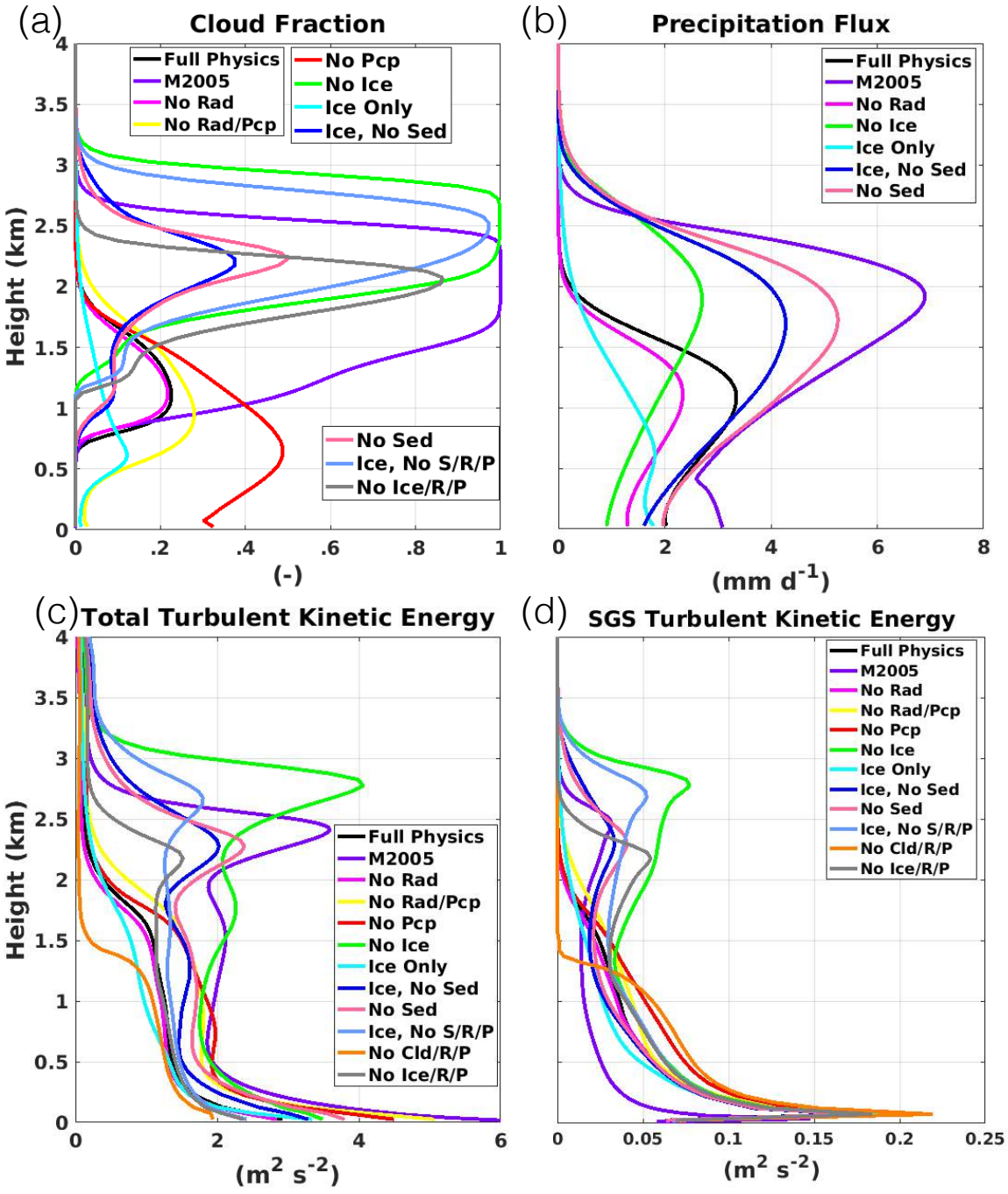

Figure 3.9. LES model run final hour mean profiles for a) cloud fraction, b) precipitation flux, c) total turbulent kinetic energy, and d) subgrid-scale turbulent kinetic energy.

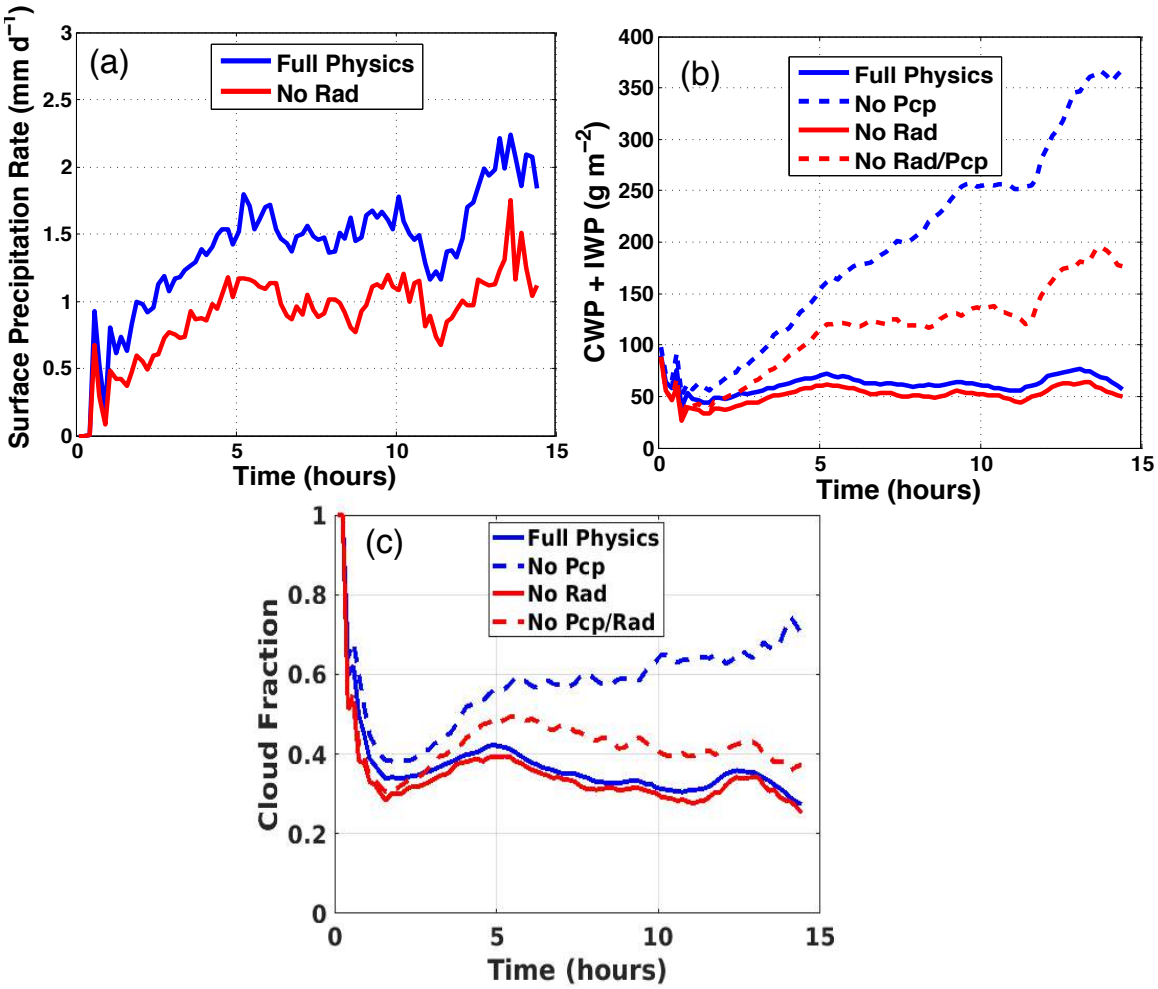

Figure 3.10. CONSTRAIN LES time series of full physics, no precipitation, no radiation, and no radiation or precipitation runs for a) surface precipitation rate, b) cloud water path + ice water path, and c) cloud fraction.

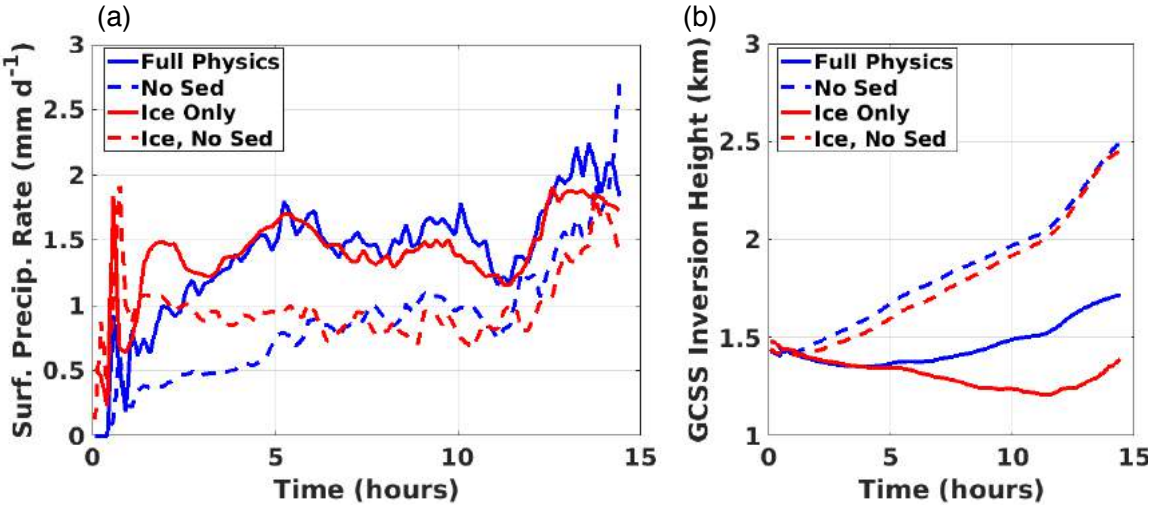

Figure 3.11. CONSTRAIN LES time series of a) surface precipitation rate and b) inversion height for full physics, no ice sedimentation, ice only, and ice only + no ice sedimentation runs.

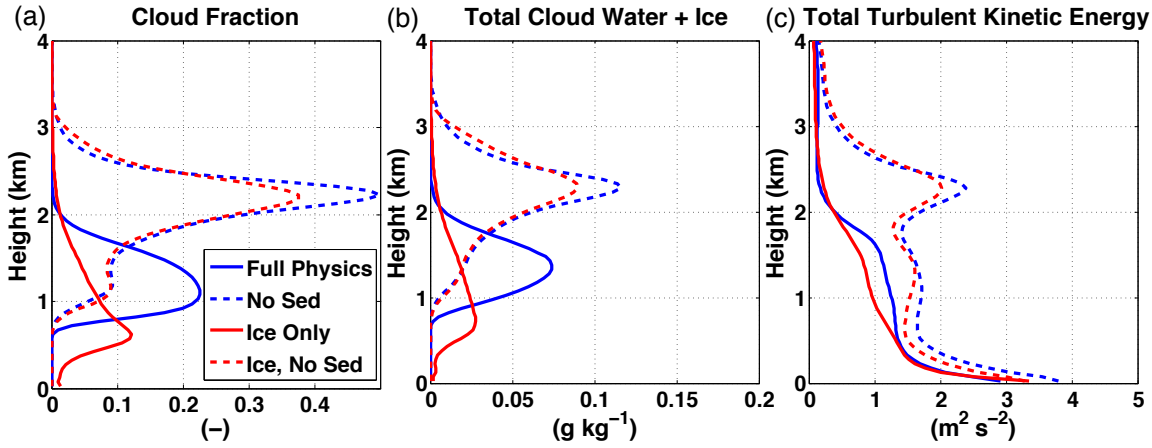

Figure 3.12. Final-hour averaged CONSTRAIN LES profiles of a) cloud fraction, b) total cloud water and ice, and c) total turbulent kinetic energy for full physics, no ice sedimentation, ice only, and ice only + no ice sedimentation runs.

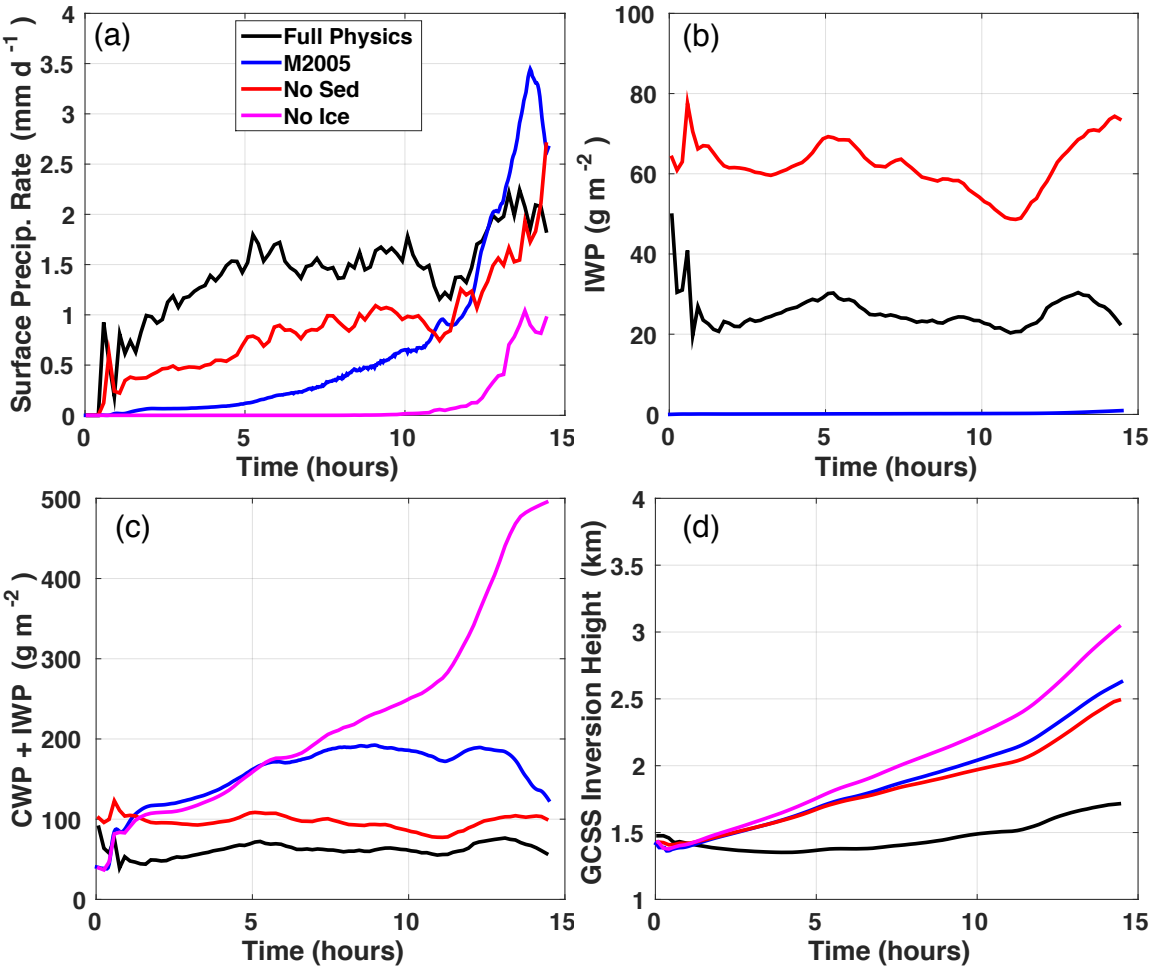

Figure 3.13. CONSTRAIN LES time series of full physics, Morrison (M2005) microphysics, no ice sedimentation, and no ice runs for a) surface precipitation rate, b) cloud water path + ice water path, c) ice water path, and d) inversion height.

CHAPTER 4

RADIATIVE CONVECTIVE EQUILIBRIUM

4.1 Background

Radiative convective equilibrium (RCE) modeling provides a simple proxy for Earth's climate. RCE is a statistical equilibrium between radiative cooling of the atmosphere and heating due to convection. In early runs looking at RCE a fixed lapse rate constraint was able to approximate convection on an equilibrium system (Manabe and Strickler, 1964; Manabe and Wetherald, 1967). Estimates of climate sensitivity could be made using RCE as a baseline state. Manabe and Wetherald estimated a doubling of CO_2 would increase temperature of an atmosphere with fixed relative humidity by roughly 2°C. They also noted that high cirrus clouds heat the surface while low clouds cool the surface.

RCE runs can be used to test prescribed changes in a model through a simpler equilibrium climate. Using an RCE simulation the Cloud-Resolving Convection Parameterization (CRCP) was able to represent large scale features reasonably well but was unable to handle organized convection (Grabowski, 2001). When the Community Atmosphere Model, version 5 (CAM5) was tested on RCE with a 100-km grid spacing and a high resolution 25-km grid spacing the latter produced smaller cloud systems that had stronger precipitation intensity (Reed et al., 2015).

The influence of clouds on the Earth's radiation budget remains a challenge as it relates to changes in cloud cover or cloud types in response to warming and cloud-aerosol interactions, the latter of which is one of the largest sources of uncertainty in the anthropogenic component of climate change (Myhre et al., 2013). There is a large amount of variation between models on magnitude, sign, and longwave and shortwave components of changes in net cloud feedbacks (Cess et al., 1996).

One way to look at top of atmosphere radiation budgets is to look at contributions from cloud type bins defined by optical thickness and cloud top pressure. Data from the

Earth Radiation Budget Experiment (ERBE) and the International Satellite Cloud Climatology Project (ISCCP) were used by Hartmann et al. (2001) to assess radiation budgets in convective tropical regions. They found that the positive and negative radiative forcings largely balance despite individual contributors potentially having large positive or negative values.

4.2 Methodology

To evaluate cloud and radiative property dependencies on a broad variety of cloud-resolving model (CRM) configurations, 42 model runs have been performed. Specifications in the model configurations include SST, horizontal grid size, microphysics scheme, and turbulence closure scheme. SSTs selected were 301 K and 305 K. Grid sizes used were 0.5, 1, 2, 4, 8, and 16 km.[1] Microphysics schemes used were SAM single-moment microphysics and the M2005 double-moment microphysics (Morrison et al., 2005), which are referred to in this chapter as 1M and 2M, respectively. Turbulence closure schemes used were standard SAM-TKE (referred to in this chapter as NOSHOC) or SHOC. Runs performed were 50 day simulations.

Runs were first performed on a 256x256 km domain with 84 vertical levels. However, many SHOC runs experienced self-aggregation. Self-aggregation has been shown to occur in RCE simulations when domain sizes are sufficiently large (Muller and Held, 2012; Jeevanjee and Romps, 2013). Muller and Held found that a system initialized with aggregated conditions will stay aggregated even at the finest resolution if the domain is large enough, over 200 km in their study. When RCE simulations are not self-aggregating they have been shown to be qualitatively similar across a large range of GCM domain sizes (Silvers et al., 2016). In SAM, cloud-radiative feedbacks and convective gustiness have been found to initiate self-aggregation (Bretherton et al., 2005). They found that reduced radiative cooling of anvil cirrus air columns along with increased surface latent and sensible heat in convectively active regions create the instability that results in self-aggregation.

Self-aggregation can be identified through finding extreme and persistent precipitable water regions in 2-D output. Examples of precipitable water fields are shown in Figure 4.1. The left column shows the NOSHOC 1M 305 K run on a 256 km domain. However,

[1] Runs with 0.5 km grid spacing were performed by Marat Khairoutdinov.

the same run, except performed with SHOC, shown in the middle column, developed a persistent and deepening negative precipitable water anomaly after day 10. Running the SHOC case that self-aggregated on a 128 km domain, the right column, with 4 copies of the domain to show scale, did not self-aggregate even after 50 days. SHOC runs frequently self-aggregated on the 256 km domain and smaller grid spacing SHOC runs run with 2M microphysics even aggregated on the 128 km domain. None of the NOSHOC runs showed self-aggregation. The table of non-aggregating model simulations performed is shown in (Table 4.1).

By having simulations at different SSTs the climate dependence of cloud and radiative properties can be determined. Additionally, climate feedbacks can be calculated using radiative kernels (Soden et al., 2008). Eight additional 1 km runs were performed for each combination of SST, microphysics scheme, and turbulence closure scheme on a 64 km domain with ISCCP simulated cloud fraction bins saved to which radiative kernels could be applied. The advantage to using the cloud radiative kernels is that the radiative feedbacks are solely due to cloud responses. Noncloud differences in the atmosphere such as temperature profiles of the runs varying in SST can impact radiative forcings making isolating the effects of clouds difficult. Two sets of kernels were considered with the Zhou et al. (2013) set using a similar methodology as Zelinka et al. (2012a,b) which derived the radiative kernels from the Fu-Liou radiative transfer model (Fu and Liou, 1992, 1993). The observation based radiative kernels generated from ERA Interim over 2000-2010 (Zhou et al., 2013) were initially selected over CFMIP1 climate model derived kernels (Zelinka et al., 2012a,b). This was done due to a closer match with SAM statistics file radiative forcings, which were subject to non-cloud influences, under the assumption that those were more representative of the case. However, with the recent release of version 3 of the observation kernels and recalculating for this study, the two sets of kernels became approximately the same, suggesting that the climate derived kernels would have been the correct choice from the start and that the differences between the two are minor in this situation.

4.3 Results

From the RCE simulations, dependencies on microphysics, turbulence parameterization scheme, grid spacing, and SST were evaluated. All results detailed in this section are

25-day averages of days 26-50 in model run simulations.

Precipitable water and surface precipation rate means and standard deviations are shown in Figure 4.2. The largest influence on both of these variables was SST with clear separation between the 305 K runs and the 301 K runs with precipitable water values approximately 20 mm higher and surface precipitation rates approximately .6 mm d^{-1} higher for all model configurations of microphysics, grid size, and turbulence parameterization scheme. SHOC 1M runs had slightly lower surface precipitation rates than their NOSHOC equivalents (Figure 4.2a,c). Smaller grid spacing runs had slightly higher precipitable water and slightly lower surface precipitation rates than larger grid spacing runs. The standard deviation for precipitable water is very low (Figure 4.2a,b) while the standard deviation for surface precipitation rate increases with larger grid size (Figure 4.2c,d).

Cloud water path (CWP) and ice water path (IWP) values are presented in Figure 4.3. Larger grid spacing 2M runs with SHOC have higher CWP than their 1M counterparts (Figure 4.3a,b). The 301 K SHOC runs had a much lower CWP than the 305 K SHOC runs and the NOSHOC runs at either SST. These 301 K SHOC runs have very little grid size dependence on CWP. SHOC runs with 1M microphysics have lower CWP and IWP than the NOSHOC equivalents (Figure 4.3a,c). Altering the grid spacing results in CWP increasing and IWP decreasing as grid spacing increases, with the increases in CWP much larger in magnitude than the decreases in IWP. There is a large difference in IWP depending on the microphysics scheme selected with much lower IWP in the 2M runs (Figure 4.3c,d). Standard deviations of ice water path are much larger, especially for 1M runs, than for cloud water path.

ISCCP simulated high and low cloud fractions are shown in Figure 4.4. Simulated high cloud fractions are higher for 2M runs than 1M runs (Figure 4.4a,b). Grid size and SST dependencies are similar for high cloud fraction compared to ice water path, and low cloud fraction compared to cloud water path. SHOC 1M runs show a larger high cloud fraction than the NOSHOC runs despite the ice water path being greater for NOSHOC runs. Standard deviations are larger for larger grid size runs except for 2M high cloud fraction.

Cloud radiative effects, which represent the change in the radiative fluxes due to clouds though is also dependent on atmospheric variables such as temperature, are shown in

Figure 4.5. Longwave (LW) cloud radiative effect is similar to high cloud fraction with the exception of a 2M SHOC vs NOSHOC gap in LW cloud radiative effect which does not show up in high cloud fraction (Figure 4.5b vs Figure 4.4b). The negative of shortwave (SW) cloud radiative effect is similar to low cloud fraction. The SW cloud radiative effect has a larger influence on the net cloud radiative effect than the LW. At large grid sizes all runs except 301 K SHOC runs have negative net cloud radiative effects. For 1M NOSHOC runs at the lowest grid sizes (0.5 km and 1 km) net cloud radiative effect is negative; however, for 1M SHOC runs and all 2M runs, the average net cloud radiative effect is positive for 1 km runs (Figure 4.5e,f).

Sensitivities for these variables can be determined using the 301 K and 305 K runs. Precipitable water and surface precipitation sensitivities are shown in Figure 4.6. NOSHOC runs with either microphysics scheme have similar precipitable water sensitivity (Figure 4.6a) to increasing temperature, approximately 4.5 mm K^{-1} except for a slightly lower sensitivity of approximately 4 mm K^{-1} for the 16 km run. SHOC runs have less of a clear pattern though the 1 km runs have the highest sensitivity. For surface precipitation (Figure 4.6b), NOSHOC runs are consistent with an increase in surface precipitation rate of approximately .15 mm d^{-1} K^{-1}. SHOC runs have an increasing surface precipitation rate sensitivity to temperature as grid size gets larger.

Figure 4.7 shows the sensitivity of CWP and IWP to warming. For CWP (Figure 4.7a) there is very little temperature influence on NOSHOC runs. However, for SHOC runs, there is a large positive increase in CWP with warming, especially for larger grid sizes and for 2M runs, primarily due to CWP being so low for the 301 K 2M SHOC runs with 8 and 16 km grid spacing. IWP (Figure 4.7b) has a near zero to slightly negative sensitivity for NOSHOC runs, but a near zero to slightly positive sensitivity for SHOC runs.

ISCCP cloud fraction sensitivities are shown in Figure 4.8. For high cloud fraction sensitivity (Figure 4.8a) the 1M NOSHOC runs have little grid size dependence and are slightly negative with warming. 2M NOSHOC runs and SHOC runs have less consistency with grid size but range from roughly -1% K^{-1} to +0.5% K^{-1} with the highest positive feedbacks being the 1 km SHOC runs. Low cloud fraction sensitivity (Figure 4.8b) is similar to that for cloud water path, with small increases in cloud fraction at large grid spacing for NOSHOC runs and much larger increases in cloud fraction for SHOC runs.

Cloud radiative effect sensitivities are shown in Figure 4.9. LW cloud radiative effect sensitivities (Figure 4.9a) are similar to those for ISCCP high cloud fraction (Figure 4.8a) and ice water path (Figure 4.7b) with negative sensitivities for NOSHOC runs but a range of negative to positive sensitivities for SHOC runs. SW cloud radiative effect sensitivities (Figure 4.9b) are similar to the negative of ISCCP low cloud fraction (Figure 4.8b) and cloud water path (Figure 4.7a) sensitivities. There is very little change for NOSHOC run SW sensitivity compared to the much larger negative SW radiative effect changes for SHOC runs. Net cloud radiative effect sensitivities (Figure 4.9c) are dominated by the SW sensitivities.

Mean cloud fraction profiles for the last 25 days of simulations are shown in 12 different comparisons in Figure 4.10. For the SHOC vs NOSHOC comparison (left column), SHOC runs have higher upper tropospheric cloud fraction than the NOSHOC equivalents. For comparisons between the 305 K and 301 K runs (middle column) the warmer SST results in a higher cloud elevation. There is a slightly higher cloud fraction in the upper troposphere for the 301 K runs than the 305 K runs. The 305 K runs have higher low-cloud fraction in the SHOC runs than in the 301 K SHOC runs. For comparisons between 1M and 2M microphysics (right column) the 2M runs have a much higher cloud fraction in the upper-troposphere. 1M runs have a small increase in cloud fraction around 15 km, or a slowing in the decrease in cloud fraction with altitude, which does not show up in 2M runs.

Mean 25-day profiles of total cloud water + ice (QN) are shown in Figure 4.11 as for cloud fraction before. For SHOC vs NOSHOC comparisons (left column) there is little difference in higher upper-troposphere QN. For the low levels QN is higher for NOSHOC for 1M 305 K and much higher for NOSHOC for 301 K of either microphysics scheme. For 2M 305 K runs the SHOC values are much higher than NOSHOC for runs which are the larger grid spacing runs. For 305 K vs 301 K comparisons (middle column) for all setups the warmer SST runs have slightly higher to much higher (for SHOC at low levels) QN values. The warmer SST runs also have higher upper-level elevations of maximum QN. For 2M vs 1M comparisons (right column) the 2M runs have higher QN at lower levels (except for 301 K SHOC which are similar), a lower magnitude high-level maximum in QN, and a higher elevation high-level maximum in QN.

Cloud fraction profiles as a function of temperature, in order to further evaluate the

middle column of Figure 4.10 with regard to cloud temperatures, are shown in Figure 4.12. In all cases, low-level cloud fraction decreased as horizontal grid spacing decreased. Upper-level cloud top temperature was similar for all runs regardless of SST (a, b, e, f vs c, d, g, h). This result matches up with findings in Hartmann and Larson (2002) which detailed a feature called the fixed anvil temperature hypothesis. Further research found less than a 0.5 K change in cloud top temperature for a 2 K change in SST (Kuang and Hartmann, 2007). For NOSHOC runs, larger grid spacing runs had cooler maximum cloud fraction level temperatures than the smaller grid spacing runs. Smaller grid spacing 1M runs for both SHOC and NOSHOC had a small increase in cloud fraction around 190 K.

ISCCP simulations allowed for cloud histograms separated into 7 cloud top pressure bins and 7 optical thickness bins. A set of these results was made for all 8 model setups (varying in SST, microphysics, and turbulence parameterization scheme) using 1 km grid spacing runs on a 64 km domain. The cloud fraction histograms are multiplied by the ERA interim LW and SW cloud radiative kernels from Zhou et al. (2013) to make histograms of LW, -SW, and net cloud forcing from which feedbacks could be calculated. These cloud feedbacks derived from the kernels have the benefit of attributing inter-run differences solely due to clouds rather than also being influenced by changes in other atmospheric variables such as temperature profiles. These results are based on the recently updated third version of the observational kernels.

Cloud fractions and feedbacks for each of the histogram bins are shown for NOSHOC (Figure 4.13) and SHOC (Figure 4.14) runs. For NOSHOC and SHOC runs the most frequent cloud type is upper-level cirrus clouds between 50 and 180 mb with optical thickness below 3.6. Cloud fractions are more concentrated in the lowest pressure level bins in the 2M runs. A logarithmic scale highlights small cloud fractions in some low-level cloud bins spread out along the range of optical thickness, moreso for NOSHOC than SHOC, and a very small fraction of more optically thick clouds in NOSHOC runs.

Cloud fraction feedbacks for 1M NOSHOC (Figure 4.13e) shows a shift from cloud fraction in the 180-310 mb range to the 50-180 mb range. For 2M NOSHOC runs (Figure 4.13f) there is a shift towards the highest elevation level but also towards the lowest optical depth bin. However, these cloud fraction feedbacks are very small, below 1% K^{-1} shifts for all except the increase in 2M NOSHOC. Bins in low to midlevels have changes of

approximately 0 though lean more towards very slight decreases than increases. For SHOC runs, the cloud fraction feedbacks are primarily positive in the highest elevation level for both 1M (Figure 4.14e) and 2M (Figure 4.14f) runs though there is a decrease in cloud fraction with increasing temperature in the smallest optical thickness bin for 1M SHOC. Bins in low to midlevels and higher optical thickness bins tilt towards having slightly positive cloud feedback for SHOC runs.

Kernel-derived LW cloud forcing and feedback values are shown for NOSHOC runs in Figure 4.15 and for SHOC runs in Figure 4.16. Despite the largest cloud fractions occurring in the lowest optical thickness uppermost level bin, it is the 0.3-1.3 and 1.3-3.6 optical thickness uppermost level bins with the largest LW cloud forcings for all model physics. This result was expected since the LW kernels used to map onto cloud fraction are larger for lower pressure and higher optical thickness bins, which can be seen in comparing the high-level high-optical thickness bins' LW cloud forcing to their cloud fraction values. LW cloud feedbacks for NOSHOC runs (Figure 4.15e-f) and SHOC (Figure 4.16e-f) runs are similar to their cloud fraction counterparts (Figure 4.13e-f and Figure 4.14 e-f) except with a shift towards higher optical thickness bins for the larger magnitude feedbacks.

Kernel-derived SW cloud forcing and feedback values are shown for NOSHOC runs in Figure 4.17 and for SHOC runs in Figure 4.18. The forcings are shown multiplied by -1 for easier comparison to LW cloud forcings. The largest magnitude SW cloud forcings are for the uppermost 1.3-3.6 optical thickness bins. SW kernels used to map onto cloud fraction are larger for higher optical thickness bins at all levels with a slight increase in forcing with elevation. As a result, for the low-mid troposphere the SW cloud forcing is more prominent than the LW cloud forcing. SW cloud feedbacks for NOSHOC runs (Figure 4.17e-f) and SHOC runs (Figure 4.18e-f) are also similar to the cloud fraction feedbacks except with a shift to higher magnitude feedbacks occurring with higher optical thickness.

Kernel-derived net cloud forcing and feedback values are shown for NOSHOC runs in Figure 4.19, and for SHOC runs in Figure 4.20. When combining the effects of the cloud radiative kernels for LW and SW effects for any given cloud fraction, there is a net positive forcing for upper-level cirrus and a net negative forcing for bins with higher optical thickness and/or lower elevation. For all cloud physics setups the largest positive net cloud forcing values are for the 0.3-1.3 and 1.3-3.6 optical thickness uppermost level

bins. The strongest negative forcings are in high optical thickness and/or low-level bins.

The net cloud feedback results for NOSHOC (Figure 4.19e-f) do not display a clear pattern. There are negative feedbacks in the upper level high optical thickness bins, and positive feedbacks in many of the low-mid level bins. The highest magnitude positive net feedbacks include the 3.6-9.4 optical thickness 50-180 mb bin for both the 1M and 2M. There's significant differences between the 1M and 2M upper-level cirrus net cloud feedbacks with smaller magnitude positive values for 1M across the board and very large positive and negative values for 2M. For net cloud feedback with SHOC (Figure 4.20e-f) there is a more prominent pattern. There are positive feedback values in most bins in the upper levels with optical thicknesses between 0 and 9.4. Negative net cloud feedbacks are prominent along the lowest optical thickness bin for low levels and the high optical thickness bins throughout the troposphere.

Total cloud feedbacks could be calculated from pairs of histograms differing in SST by summing up all 49 histogram bins (Table 4.2) and then finding the per K difference between the 301 K cloud forcings and the 305 K cloud forcings (Table 4.3). For all runs the LW cloud forcing was larger in magnitude than the SW cloud forcing resulting in a positive net cloud forcing. SHOC and 2M microphysics each contributed to a larger net cloud forcing. The magnitude of the LW and SW cloud feedbacks were much higher for SHOC runs than NOSHOC runs. For 1M NOSHOC runs LW and SW feedbacks were both positive resulting in a net cloud feedback of 0.52 W m^{-2} K^{-1}. 2M NOSHOC runs resulted in a negative LW cloud feedback and a near zero net cloud feedback. LW feedbacks were positive for SHOC runs while SW feedbacks were negative for SHOC runs with roughly a 30% higher magnitude in SW feedback yielding a net cloud feedback of -0.36 and -0.35 W m^{-2} K^{-1} for 1M and 2M SHOC respectively.

Vertical profiles of cloud fraction and cloud feedbacks are shown in Figure 4.21. For all microphysics and turbulence closure scheme configurations the layer cloud fraction (Figure 4.21a) increases with warmer SST at the highest layer and decreases at the second highest layer. The cloud fraction changes are quite small, on the order of 1%. In the lower to middle troposphere SHOC runs have a very slightly positive cloud fraction feedback while NOSHOC runs have a very slightly negative cloud fraction feedback.

Net cloud feedback (Figure 4.21b) is positive for NOSHOC runs except for the second

lowest layer and the highest layer (2M only). For SHOC runs net cloud feedback is negative in the lower to middle troposphere and positive in the highest layer. The low to mid levels are responsible for the overall negative net cloud feedback for SHOC. Net cloud feedback values are of lower magnitude at the highest levels than those of LW and SW cloud feedback, a result of the LW and SW feedbacks largely canceling out. LW feedbacks (Figure 4.21c) are more positive at the highest level than negative at the second highest level for all configurations except 2M NOSHOC. This is responsible for the 2M NOSHOC setup having a slightly negative LW cloud feedback while the other three have a positive LW cloud feedback. SW cloud feedbacks (Figure 4.21d) are similar in the uppermost layers to the LW cloud feedback in shape though differ in the lower to middle troposphere. There is a negative SW cloud feedback for the SHOC runs in the lower to middle troposphere (shown as a positive -1*SW) which contributes to the negative SW cloud feedback values for SHOC runs in Table 4.2. Since there is almost no LW cloud feedback in the lower to middle troposphere the SW cloud feedback dominates in that range for contribution to the net cloud feedback.

4.4 Summary and Discussion

In the RCE study dependencies of grid spacing, SST, microphysics scheme, and turbulence parameterization scheme were examined for a total of 42 model runs. None of the NOSHOC runs self-aggregated but most of the SHOC runs self-aggregated on a domain of 256 km and the SHOC runs with smaller grid spacings also self-aggregated on a domain of 128 km. This may increase the uncertainty of the SHOC runs as they have fewer grid points to work with than the 256 km NOSHOC runs and could potentially explain the somewhat larger standard deviations for 2M cloud fractions and radiative effects for SHOC runs relative to NOSHOC runs.

Surface precipitation rate primarily depended on SST while cloud and ice water paths were highly dependent on microphysics scheme with much higher CWP and lower IWP for 2M runs. CWP was also dependent on grid spacing. A similar pattern to CWP was also the case for low cloud fraction and SW radiative effect. Some of the large grid size dependencies may be a result of the lack of cloud parameterization in the coarser grid spacing runs since the model is being run as a cloud-resolving model.

Cloud fraction in the upper-troposphere was higher for SHOC and double-moment runs compared to their NOSHOC and single-moment counterparts. For NOSHOC the cloud fraction maximum was at cooler temperatures for runs with larger grid spacings. All runs had similar cloud top temperatures. Cloud fraction in the upper-troposphere was larger for smaller grid spacings for all single-moment runs. Low-cloud fraction decreased with decreasing grid spacing for all model configurations. Cloud water + ice was higher in the upper-troposphere for single-moment runs compared to double-moment runs. Low-level cloud water + ice was higher for NOSHOC 301 K runs than the SHOC 301 K equivalent and for the SHOC 305 K runs than the SHOC 301 K equivalents.

SHOC runs had greater changes in sensitivity to precipitation and clouds with changes in grid spacing than the NOSHOC runs. This was largely due to the 301 K SHOC runs having little dependence on grid spacing while the 305 K SHOC runs and NOSHOC runs had a much larger, and consistent in the case of NOSHOC, dependence on grid spacing.

Cloud radiative kernels were used to evaluate cloud forcings solely from the clouds in the system in order to determine the radiative feedbacks from clouds for a warming climate. Domains of 64 km were selected for the kernel runs to keep all the models on the same size domain. A 1 km grid spacing was selected for the kernel runs since 1 km results were most similar to the highest resolution 0.5 km runs and allowed for a sufficient number of grid points on 64 km domains. The kernel results would likely be much different if a larger grid spacing were selected due to the large changes in cloud fraction with grid size.

The most common cloud type in these runs was high-level cirrus. Cloud fraction feedbacks showed these clouds continued to rise with increasing SST. Cloud forcings were larger in the LW than the SW for all model configurations. These differences were largest for SHOC and double-moment microphysics. Compared to the magnitude of net cloud forcing the change in net cloud forcing with an increase in temperature was small. The LW and SW feedbacks were larger in magnitude for SHOC than NOSHOC runs. For single-moment NOSHOC the LW and SW feedbacks were both positive leading to a 0.36 W m^{-2} K^{-1} net cloud feedback. Double-moment NOSHOC had LW and SW feedbacks that were approximately equal leaving a near 0 net cloud feedback. SHOC runs of either microphysics had similar negative cloud feedbacks (-0.35 and -0.36 W m^{-2} K^{-1}) due to a negative SW cloud feedback through the lower and middle troposphere, a result that is

the opposite sign of the more common results in cloud feedback studies. These results could be significantly different for other grid spacings, leaving a higher uncertainty in the robustness of these results.

Radiative kernels have been used in other studies to estimate radiative feedbacks in a warming climate. Zelinka et al. (2012a) showed a model global mean net radiative feedback of 0.57 W m^{-2} K^{-1} globally for a doubling of CO_2. The models used included 11 Cloud Feedback Model Intercomparison Project (CFMIP) GCMs which ranged from 0.16 to 0.94 W m^{-2} K^{-1} global mean net cloud feedback. Zhou et al. (2015) showed a 0.20 ± 0.21 W m^{-2} K^{-1} interannual net radiative feedback for cirrus clouds globally. The feedback was largely from contributions in the tropical tropopause and subtropical upper troposphere.

Cirrus clouds are considered to be the bins with cloud top pressure of 440 mb or less and optical thickness of 3.6 or less. Zhou et al. (2015) had used a tropical tropopause layer of 70-150 mb for which the uppermost layer in this study can be compared. Net cloud feedbacks for these cirrus bins were: 0.09 W $m^{-2}K^{-1}$ for 1M NOSHOC, -0.20 W m^{-2} K^{-1} for 2M NOSHOC, 0.23 W m^{-2} K^{-1} for 1M SHOC, and 0.16 W m^{-2} K^{-1} for 2M SHOC. For NOSHOC, tropical tropopause layer cirrus provided half the overall positive net cloud feedback (for 1M) and twice as negative as the overall negative (for 2M) net cloud feedback. Despite SHOC simulations being the runs with the negative net cloud feedback overall the tropical tropopause layer cirrus produced a positive net cloud feedback, more in line with Zhou et al. (2015).

Table 4.1. Model simulations performed for the RCE case.

RCE Run Setup			Grid Spacing (km)					
SST	Microphys.	Turb.	16	8	4	2	1	0.5
301 K	1M	NOSHOC	256	256	256	256	256	256
		SHOC	128	128	128	128	128	N/A
	2M	NOSHOC	256	256	256	256	256	N/A
		SHOC	128	128	64	64	64	N/A
305 K	1M	NOSHOC	256	256	256	256	256	256
		SHOC	128	128	128	256	256	N/A
	2M	NOSHOC	256	256	256	256	256	N/A
		SHOC	128	128	64	64	64	N/A
			Domain Size (km)					

Table 4.2. Mean latter 25-day averaged radiative kernel-derived cloud forcing values for each run 1 km RCE simulations.

Cloud Forcing	NOSHOC 1M		NOSHOC 2M		SHOC 1M		SHOC 2M	
SST	301	305	301	305	301	305	301	305
LW (W m^{-2})	51.0	51.7	56.8	55.9	54.4	60.2	54.3	58.9
SW (W m^{-2})	-47.3	-45.9	-38.9	-38.2	-38.6	-45.9	-30.1	-36.1
Net (W m^{-2})	3.7	5.8	17.9	17.7	15.8	14.3	24.2	22.8

Table 4.3. Mean latter 25-day averaged radiative kernel-derived cloud feedback values for 1 km RCE simulations.

Cloud Feedback	1M NOSHOC	2M NOSHOC	1M SHOC	2M SHOC
LW (W m^{-2} K^{-1})	0.16	-0.23	1.46	1.16
SW (W m^{-2} K^{-1})	0.36	0.17	-1.82	-1.51
Net (W m^{-2} K^{-1})	0.52	-0.06	-0.36	-0.35

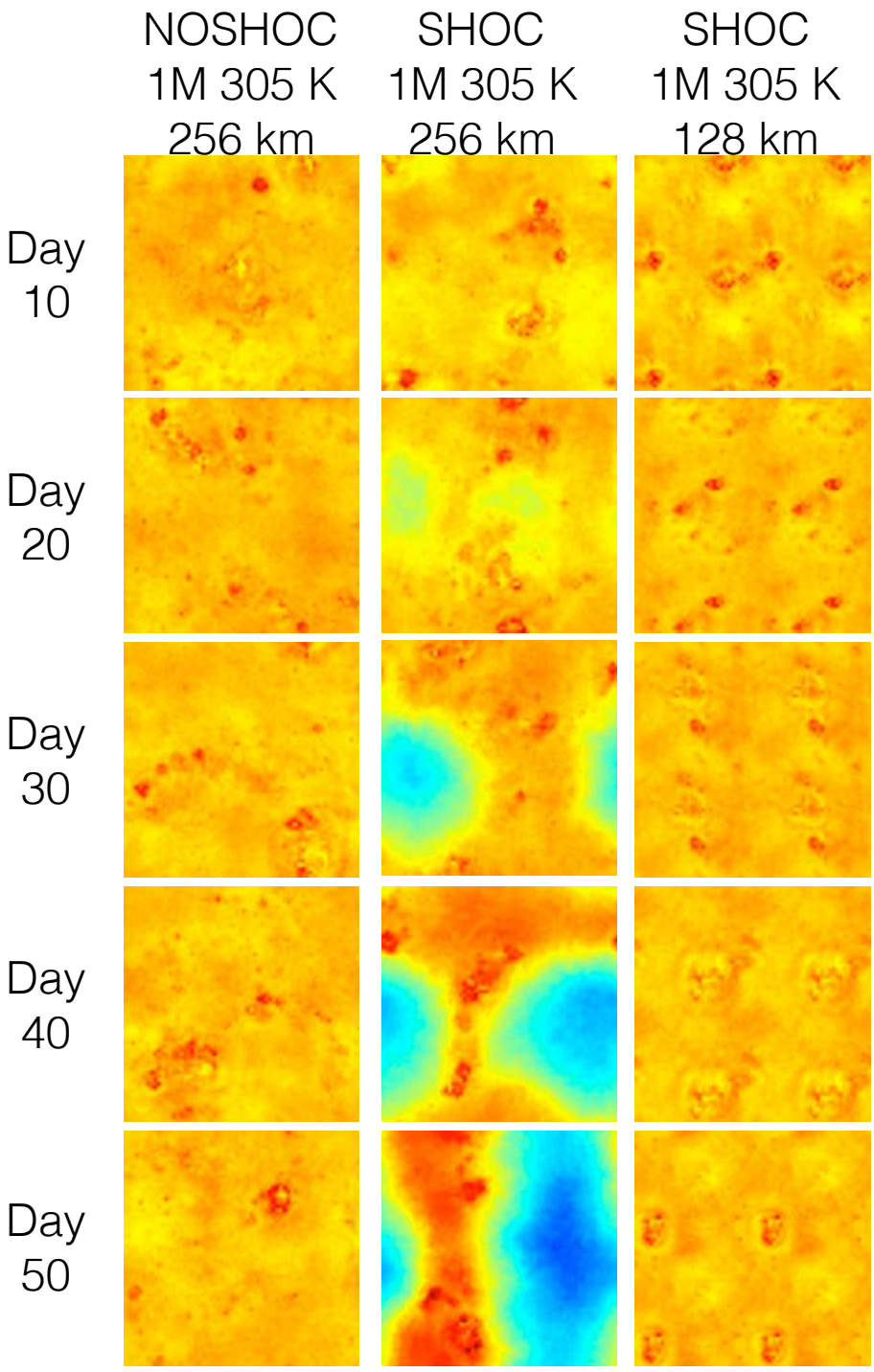

Figure 4.1. Precipitable water domains for days 10, 20, 30, 40, and 50 in 1M 305 K model runs of: column 1) NOSHOC on a 256x256 km domain, 2) SHOC on a 256x256 km domain, and 3) SHOC on a 128x128 km domain. The 128x128 km domain is presented as 4 of the same image to compare visually to the 256x256 km domain.

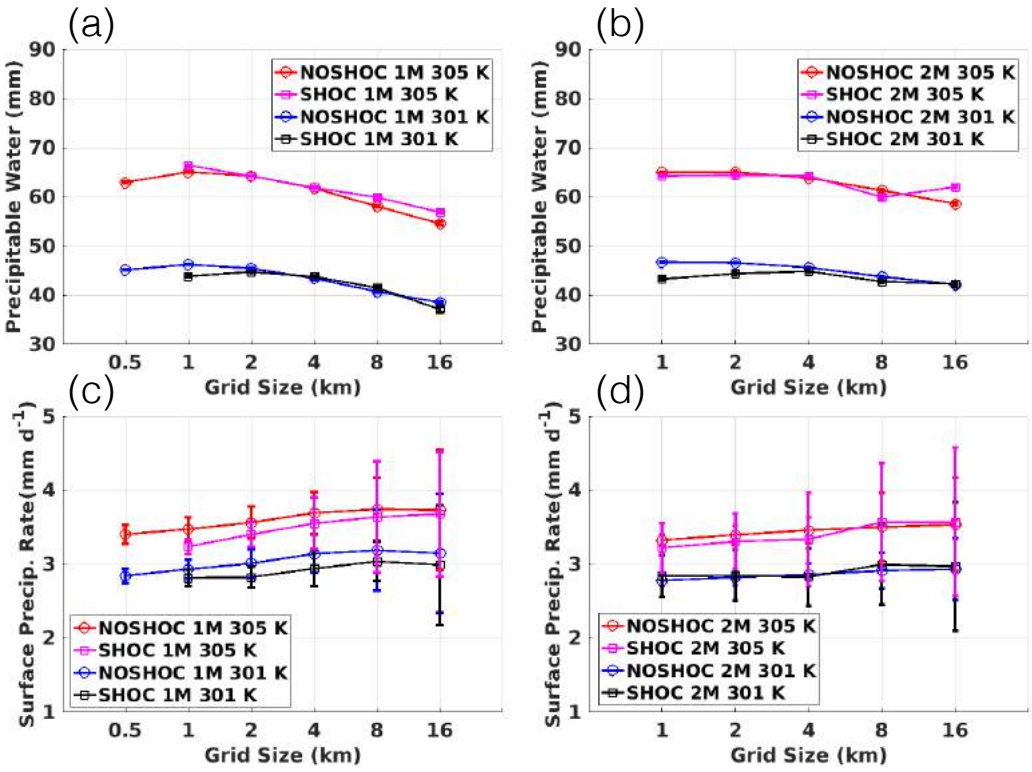

Figure 4.2. RCE simulation 25-day averaged values of: a) precipitable water for 1M microphysics runs, b) precipitable water for 2M microphysics runs, c) surface precipitation rate for 1M microphysics runs, and d) surface precipitation rate for 2M microphysics runs. Each panel shows runs varying in grid size, SST, and turbulence parameterization scheme.

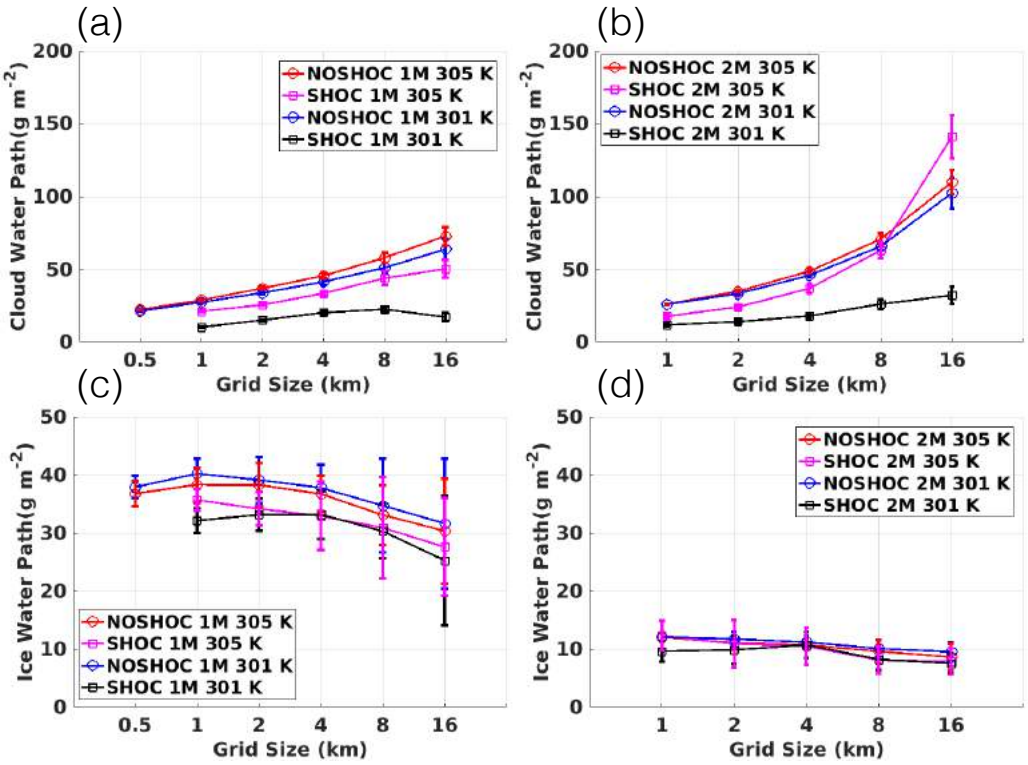

Figure 4.3. RCE simulation 25-day averaged values of: a) cloud water path for 1M microphysics runs, b) cloud water path for 2M microphysics runs, c) ice water path for 1M microphysics runs, and d) ice water path for 2M microphysics runs. Each panel shows runs varying in grid size, SST, and turbulence parameterization scheme.

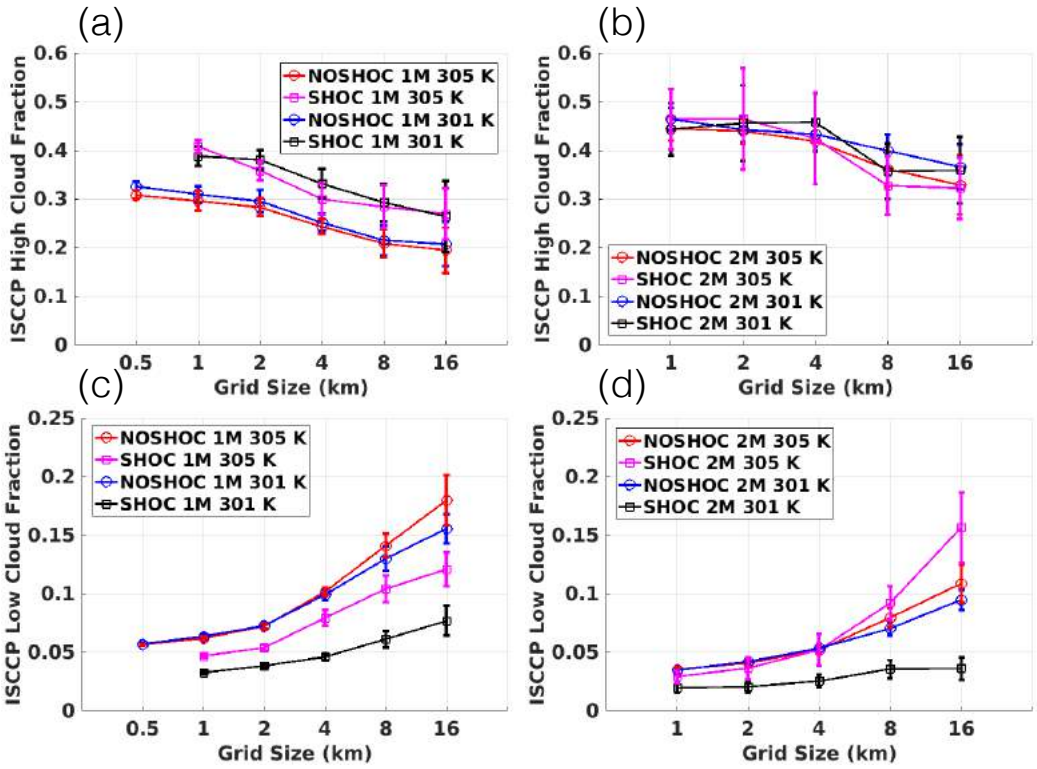

Figure 4.4. RCE simulation 25-day averaged values of: a) ISCCP simulated high cloud fraction for 1M microphysics runs, b) ISCCP simulated high cloud fraction for 2M microphysics runs, c) ISCCP simulated low cloud fraction for 1M microphysics runs, and d) ISCCP simulated low cloud fraction for 2M microphysics runs. Each panel shows runs varying in grid size, SST, and turbulence parameterization scheme.

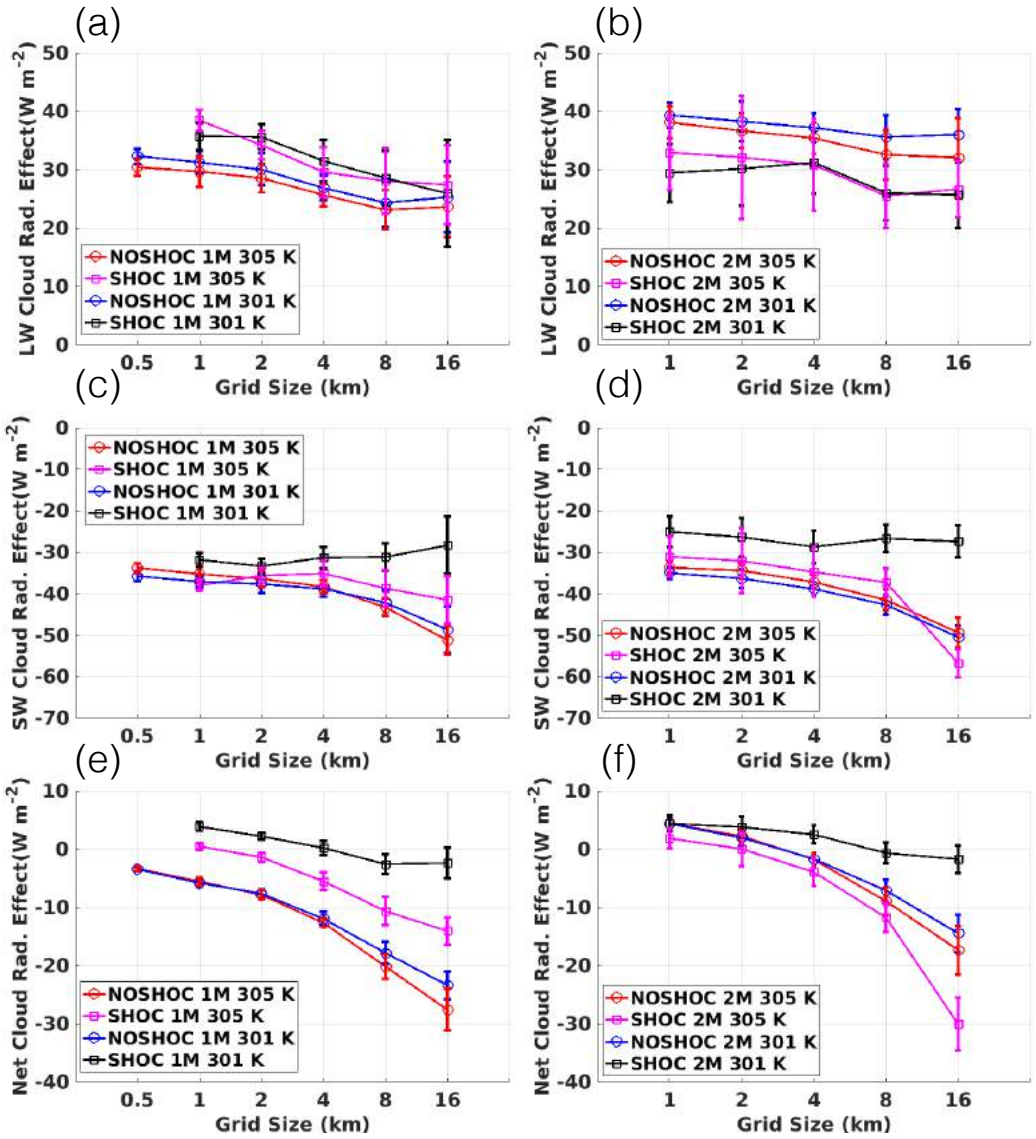

Figure 4.5. RCE simulation 25-day averaged values of: a) LW cloud radiative effect for 1M microphysics runs, b) LW cloud radiative effect for 2M microphysics runs, c) SW cloud radiative effect for 1M microphysics runs, d) SW cloud radiative effect for 2M microphysics runs, e) net cloud radiative effect for 1M microphysics runs, and f) net cloud radiative effect for 2M microphysics runs. Each panel shows runs varying in grid size, SST, and turbulence parameterization scheme.

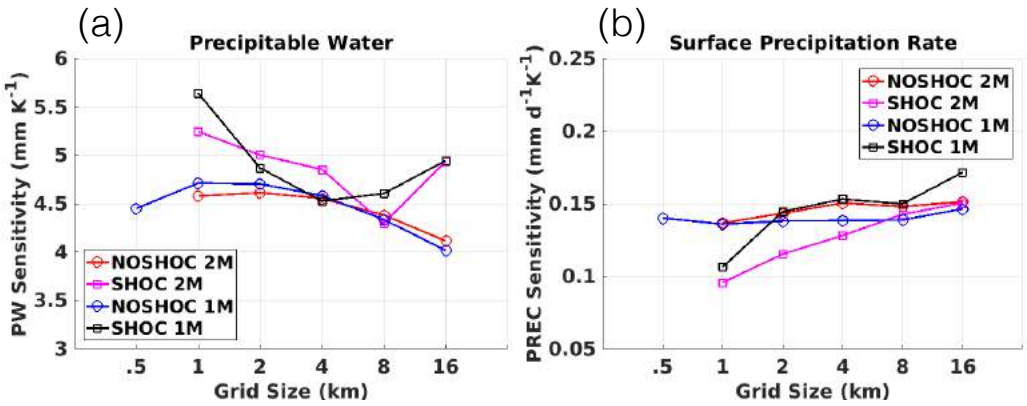

Figure 4.6. RCE last-25-day averaged sensitivity of a) precipitable water and b) surface precipitation rate to warming. Each panel shows runs varying in grid size, SST, and turbulence parameterization scheme.

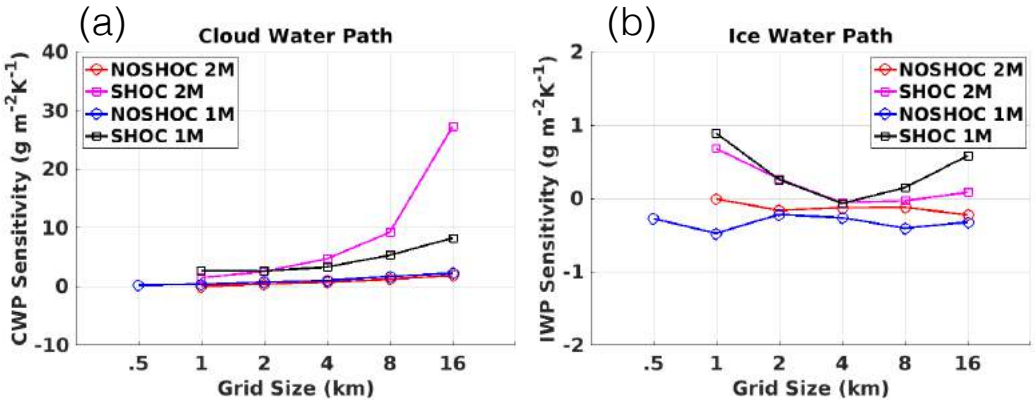

Figure 4.7. RCE last-25-day averaged sensitivity of a) cloud water path and b) ice water path to warming. Each panel shows runs varying in grid size, SST, and turbulence parameterization scheme.

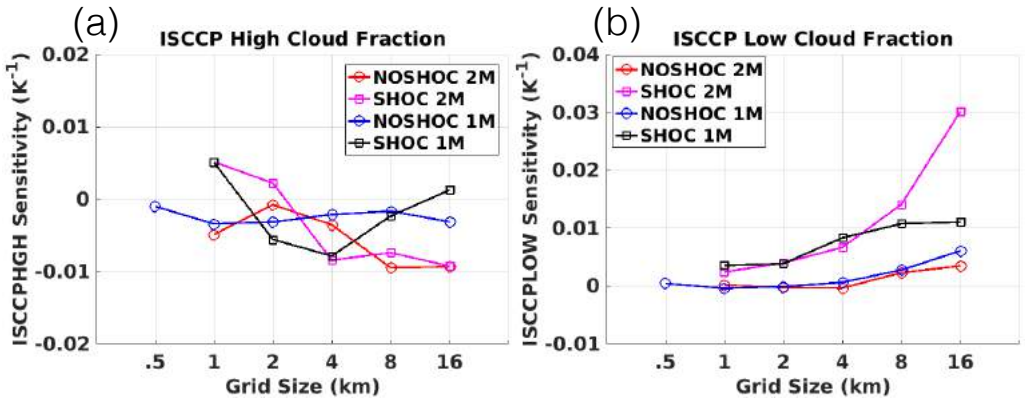

Figure 4.8. RCE last-25-day averaged sensitivity of a) ISCCP high cloud fraction and b) ISCCP low cloud fraction to warming. Each panel shows runs varying in grid size, SST, and turbulence parameterization scheme.

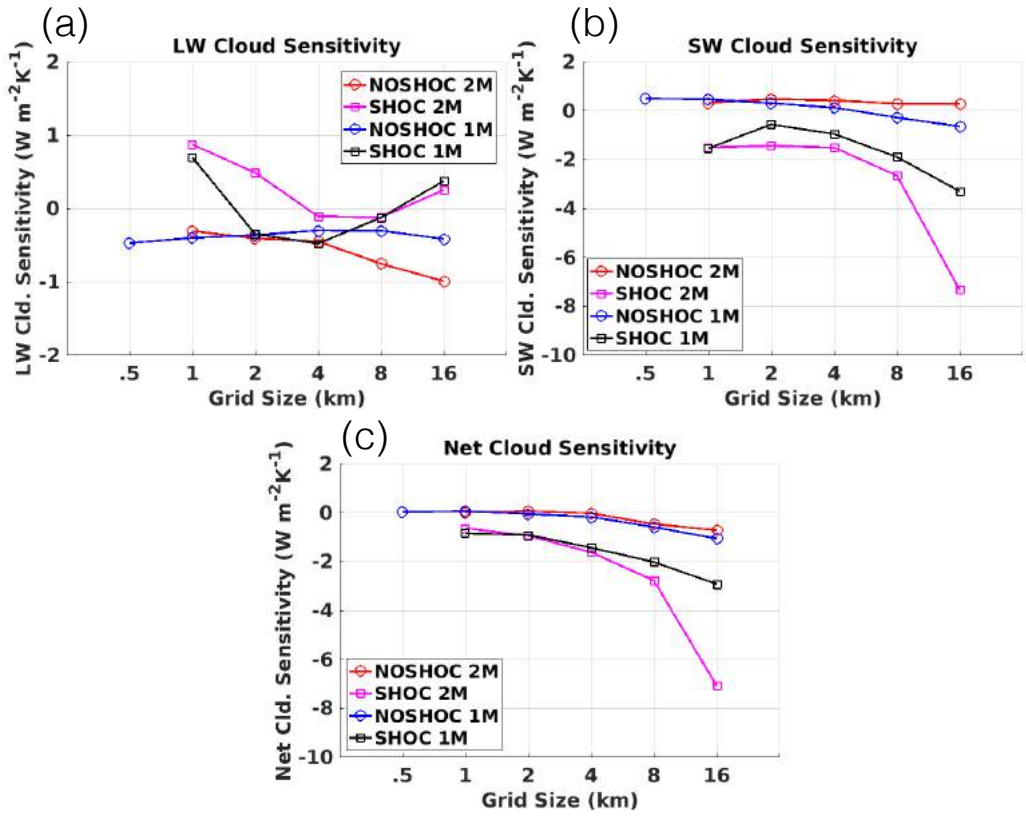

Figure 4.9. RCE last-25-day averaged sensitivity of a) LW cloud radiative effect, b) SW cloud radiative effect, and c) net cloud radiative effect to warming. Each panel shows runs varying in grid size, SST, and turbulence parameterization.

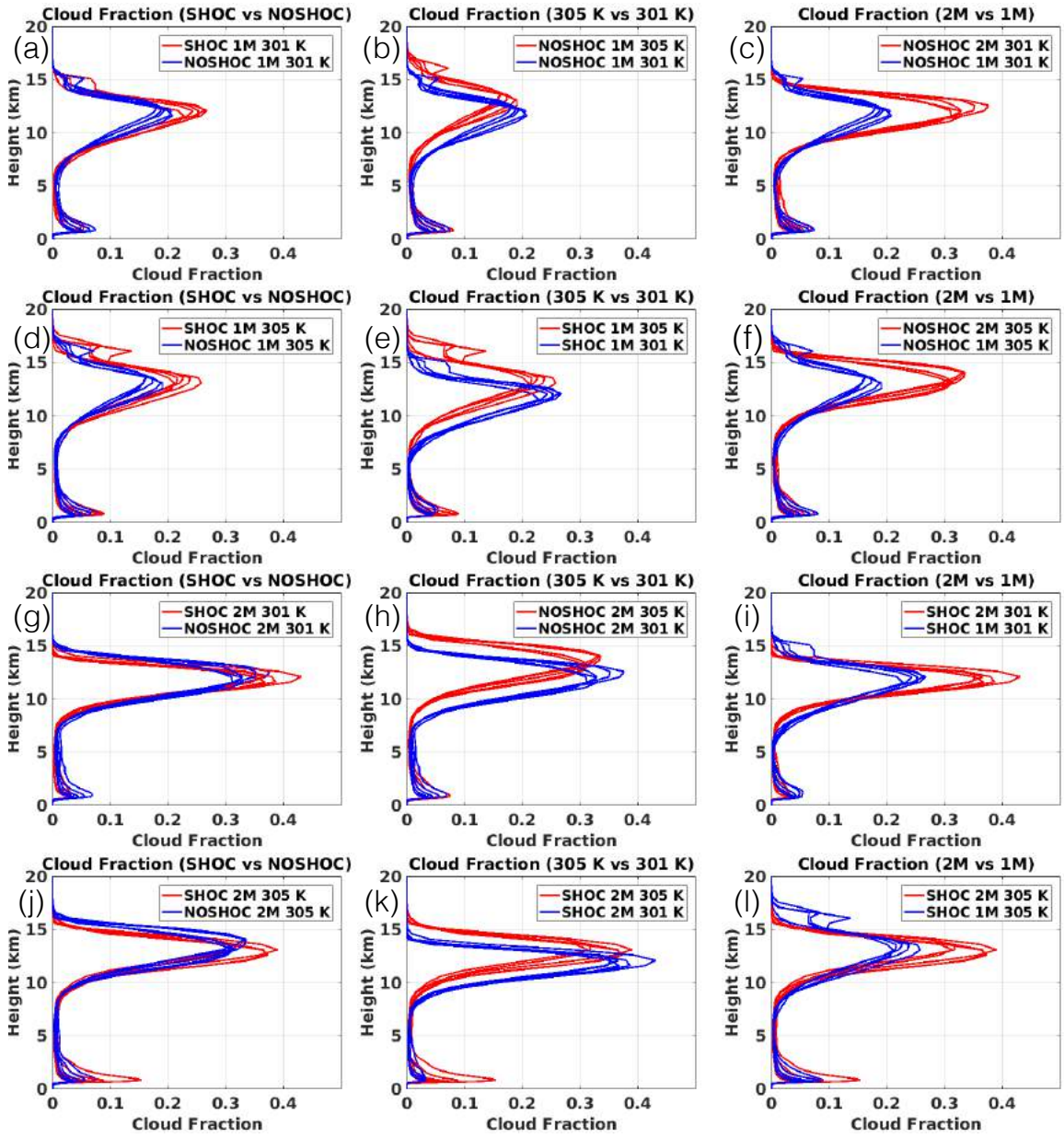

Figure 4.10. Mean cloud fraction profiles over the last 25 days of model simulations. The left column (a, d, g, j) are SHOC vs NOSHOC comparisons, the middle column (b, e, h, k) are 305 K vs 301 K comparisons, and the right column (c, f, i, l) are 1M vs 2M microphysics comparisons.

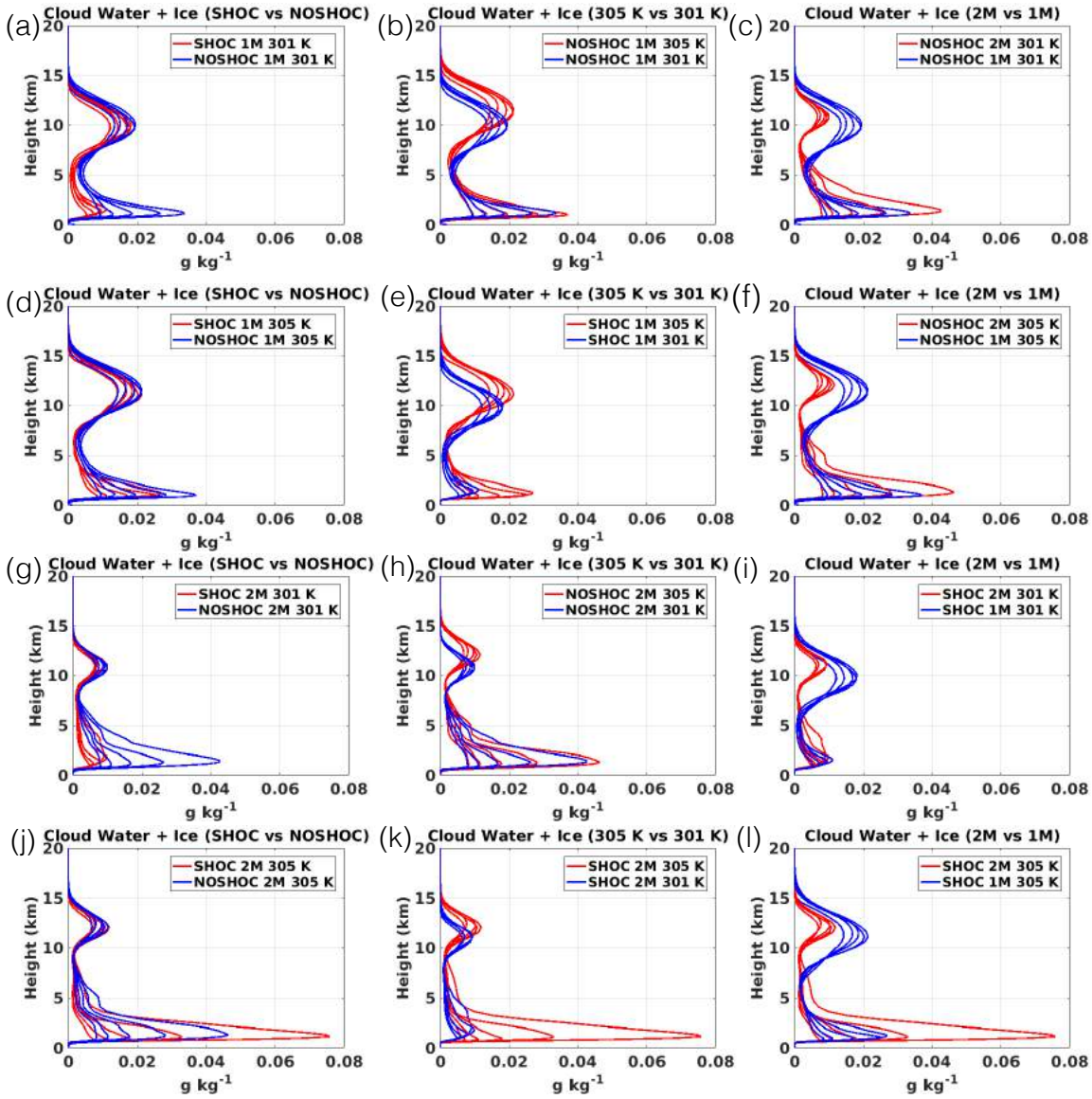

Figure 4.11. Mean total cloud water + ice profiles over the last 25 days of model simulations. The left column (a, d, g, j) are SHOC vs NOSHOC comparisons, the middle column (b, e, h, k) are 305 K vs 301 K comparisons, and the right column (c, f, i, l) are 1M vs 2M microphysics comparisons.

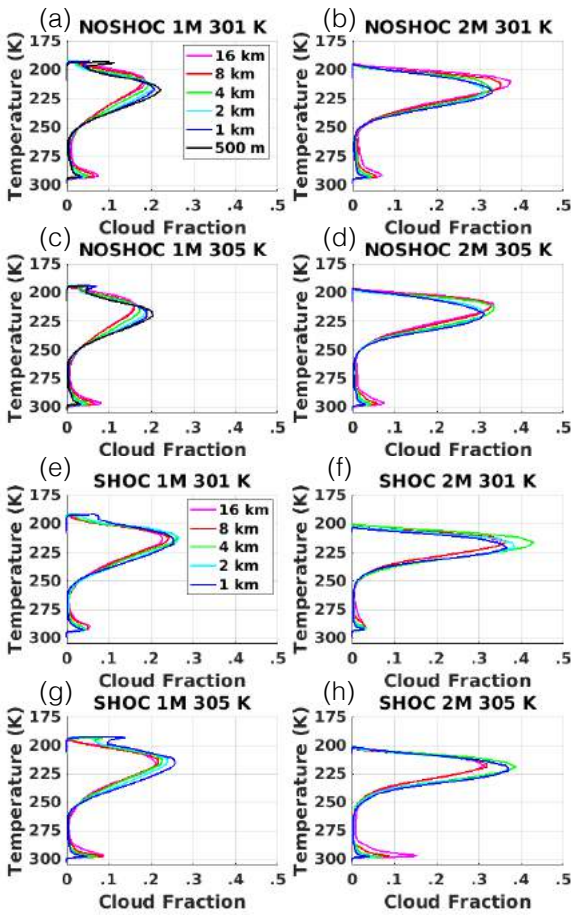

Figure 4.12. RCE simulation 25-day averaged values of cloud fraction as a function of temperature. Panels separate runs based on NOSHOC (a, b, c, d) vs SHOC (e, f, g, h), 301 K SST (a, b, e, f) vs 305 K SST (c, d, g, h), and 1M (a, c, e, g) vs 2M (b, d, f, h) microphysics.

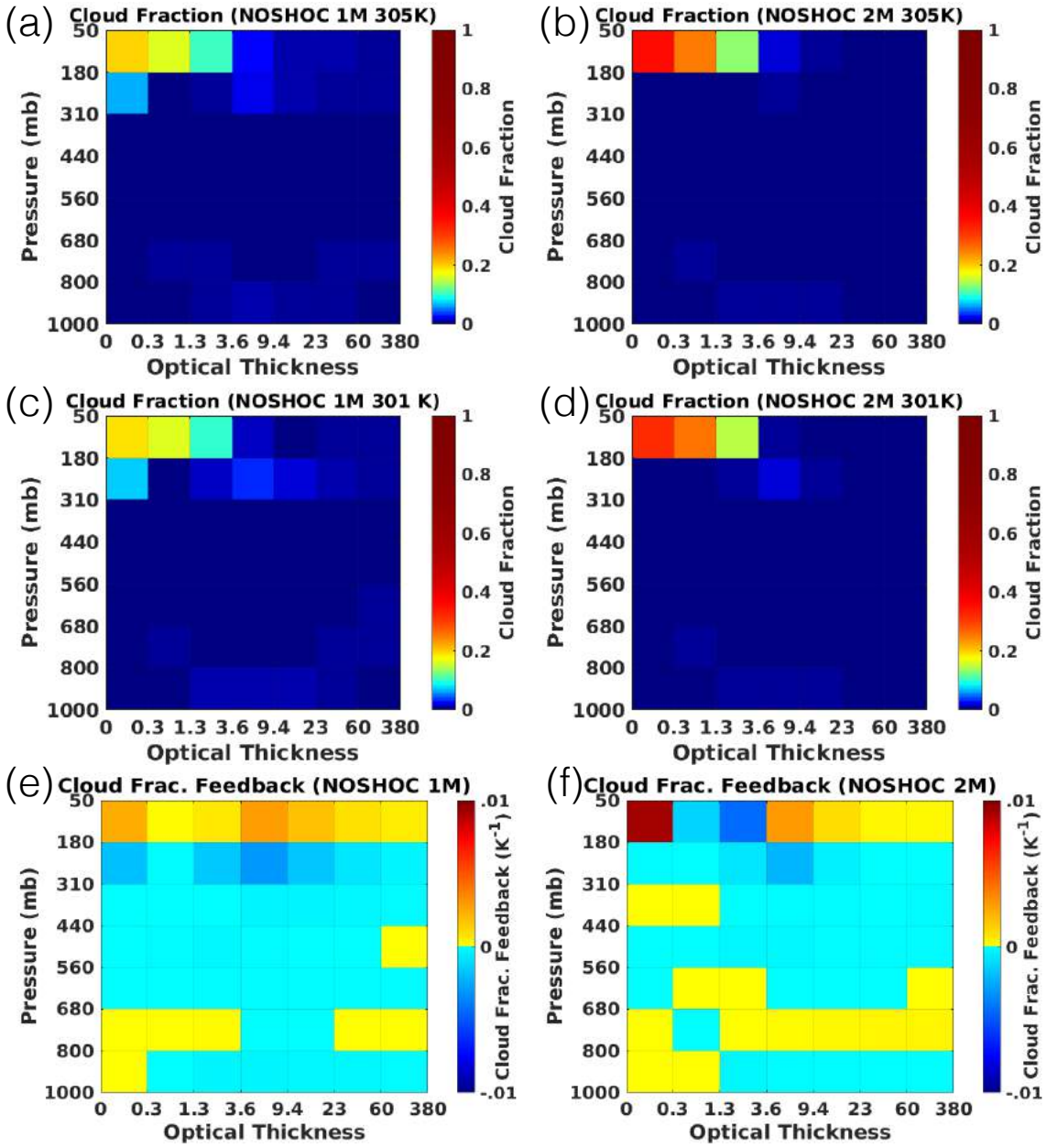

Figure 4.13. RCE 25-day averaged cloud radiative kernel derived cloud fraction for a) NOSHOC 1M 305 K, b) NOSHOC 2M 305 K, c) NOSHOC 1M 301 K, and NOSHOC 2M 301 K. Cloud fraction feedbacks are shown for e) NOSHOC 1M and f) NOSHOC 2M. Colorbars for a-d are logarithmic.

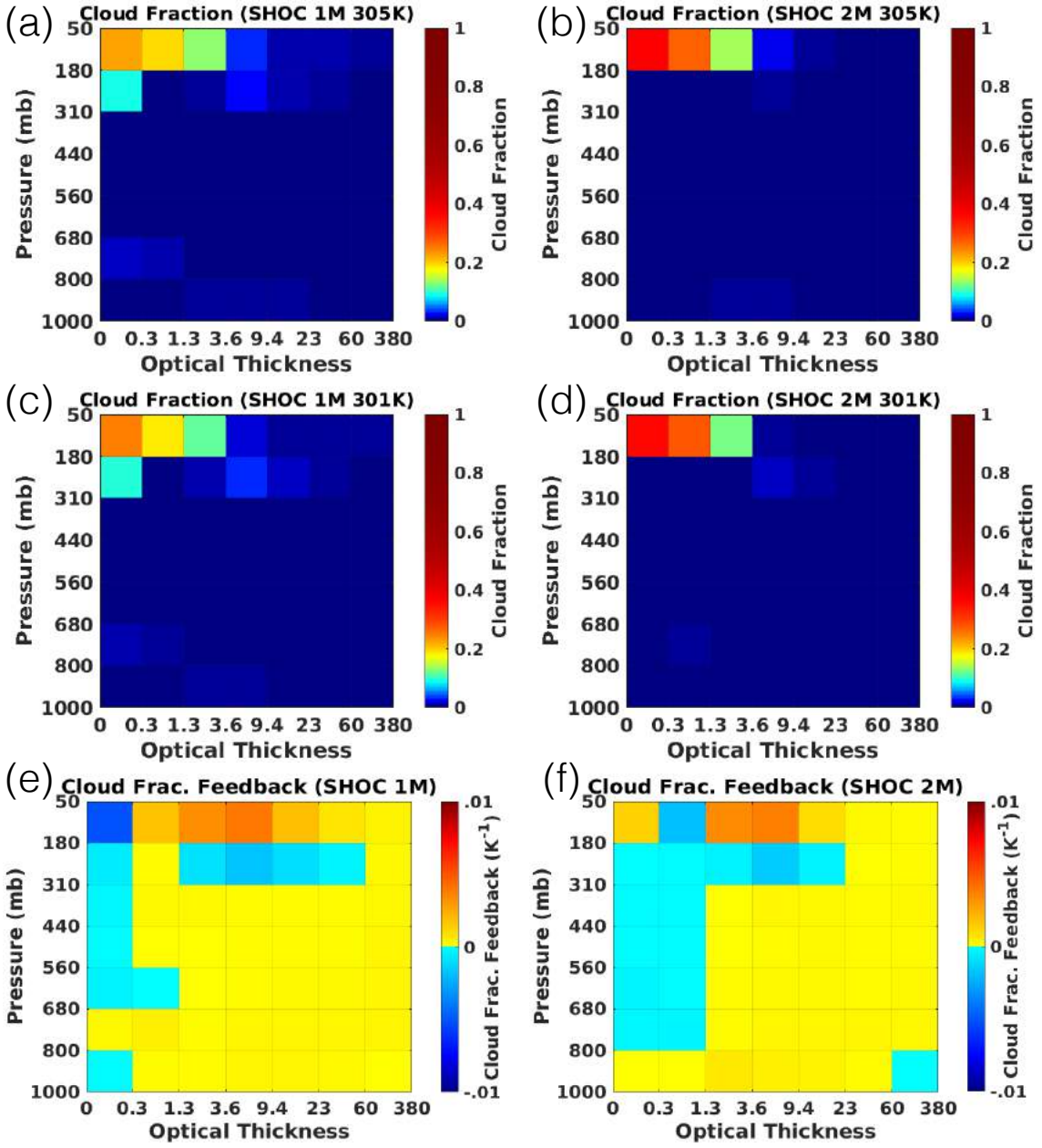

Figure 4.14. RCE 25-day averaged cloud radiative kernel derived cloud fraction for a) SHOC 1M 305 K, b) SHOC 2M 305 K, c) SHOC 1M 301 K, and SHOC 2M 301 K. Cloud fraction feedbacks are shown for e) SHOC 1M and f) SHOC 2M. Colorbars for a-d are logarithmic.

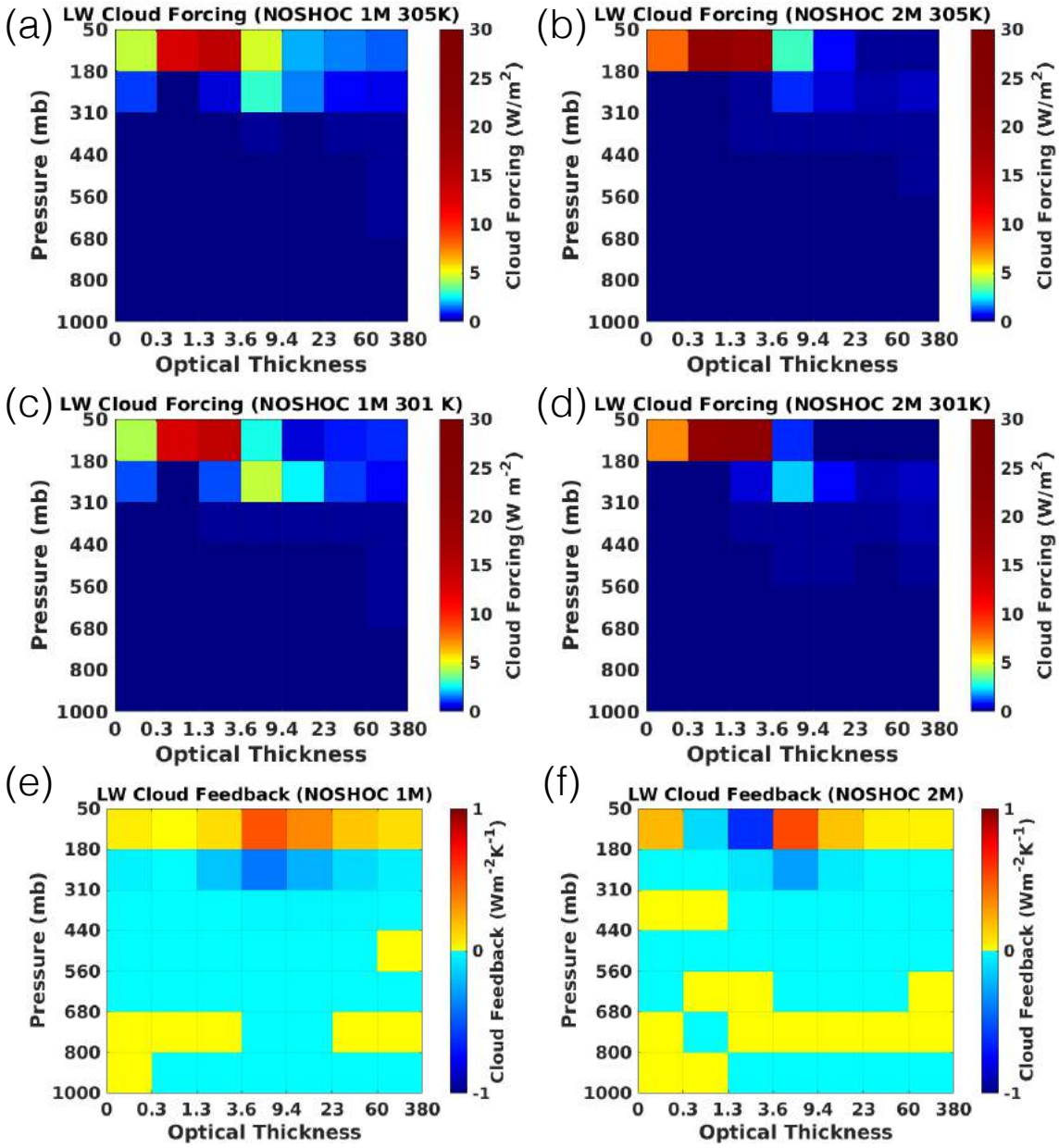

Figure 4.15. RCE 25-day averaged cloud radiative kernel derived LW cloud forcing for a) NOSHOC 1M 305 K, b) NOSHOC 2M 305 K, c) NOSHOC 1M 301 K, and NOSHOC 2M 301 K. LW cloud feedbacks are shown for e) NOSHOC 1M and f) NOSHOC 2M. Colorbars for a-d are logarithmic.

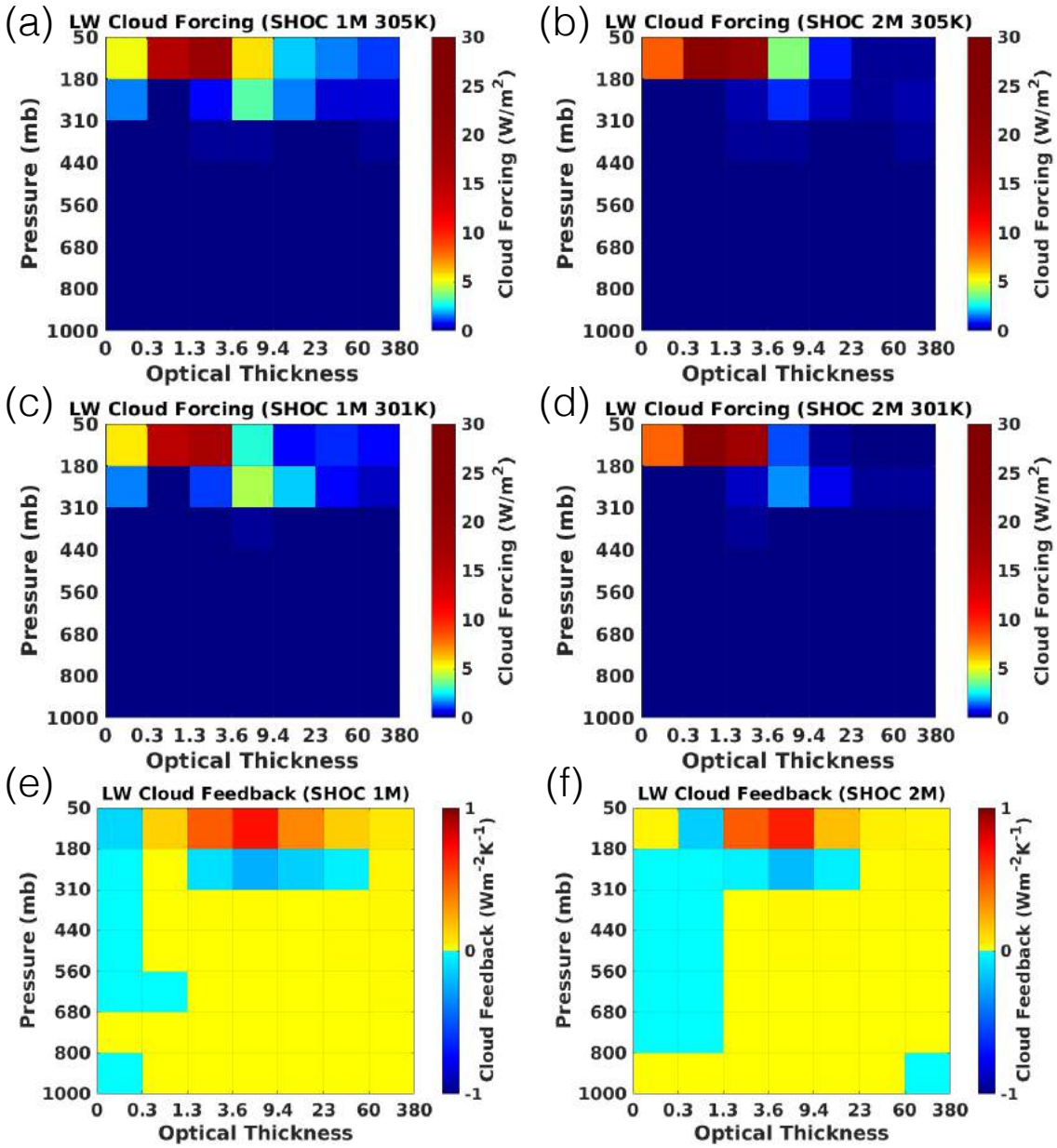

Figure 4.16. RCE 25-day averaged cloud radiative kernel derived LW cloud forcing for a) SHOC 1M 305 K, b) SHOC 2M 305 K, c) SHOC 1M 301 K, and SHOC 2M 301 K. LW cloud feedbacks are shown for e) SHOC 1M and f) SHOC 2M. Colorbars for a-d are logarithmic.

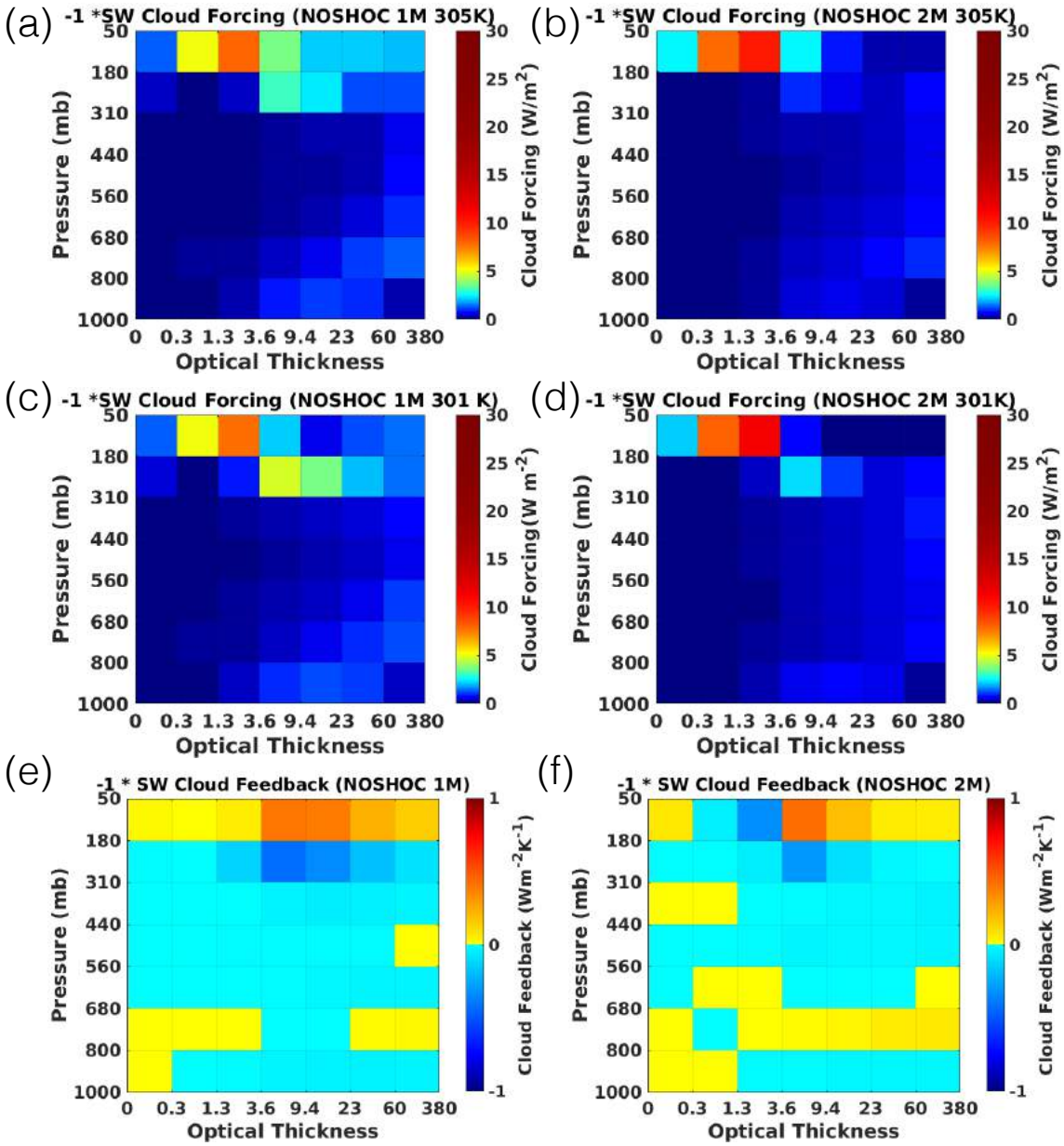

Figure 4.17. RCE 25-day averaged cloud radiative kernel derived SW cloud forcing for a) NOSHOC 1M 305 K, b) NOSHOC 2M 305 K, c) NOSHOC 1M 301 K, and NOSHOC 2M 301 K. SW cloud feedbacks are shown for e) NOSHOC 1M and f) NOSHOC 2M. Values are multiplied by -1 to compare to LW cloud forcings/feedbacks. Colorbars for a-d are logarithmic.

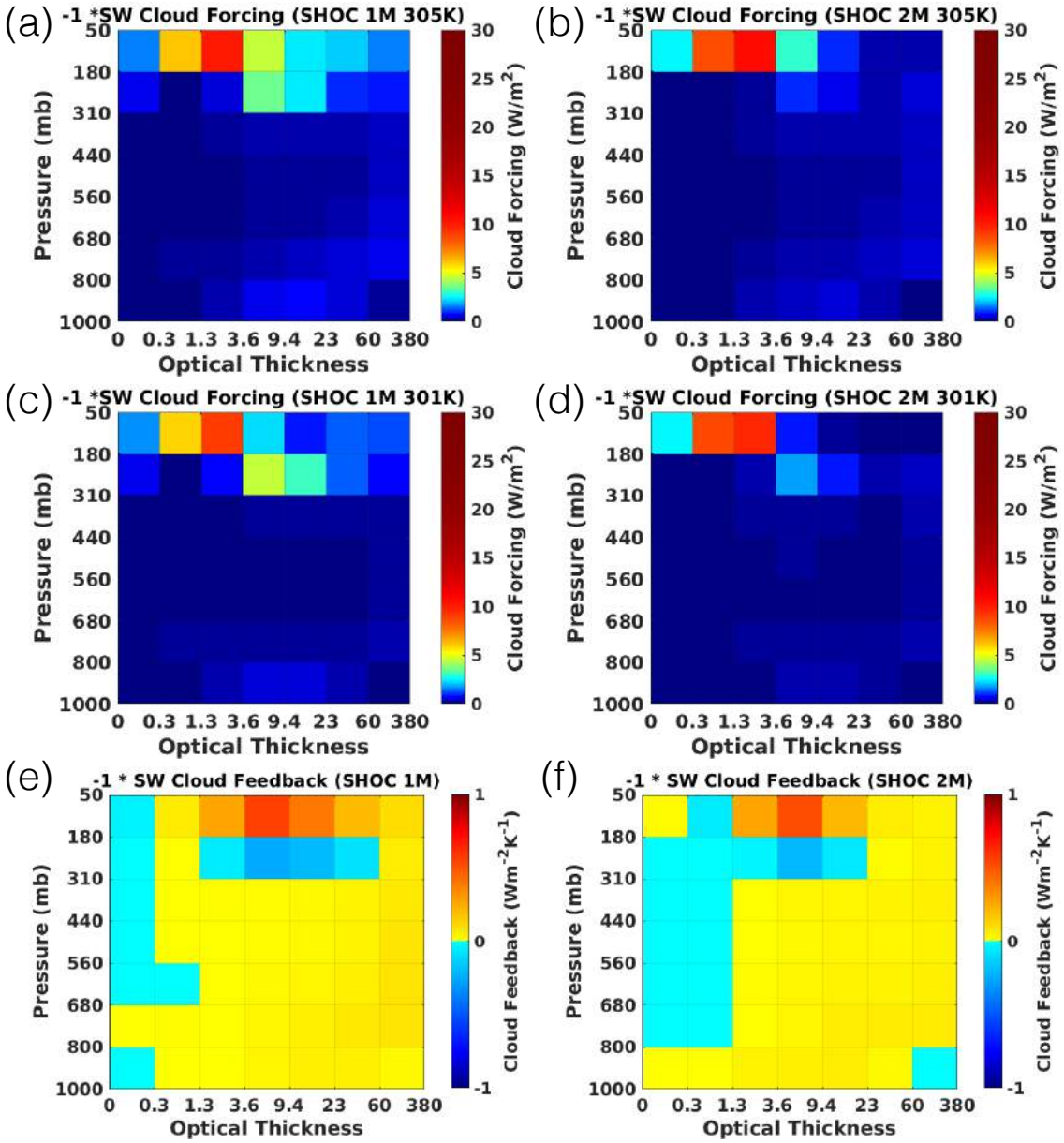

Figure 4.18. RCE 25-day averaged cloud radiative kernel derived SW cloud forcing for a) SHOC 1M 305 K, b) SHOC 2M 305 K, c) SHOC 1M 301 K, and SHOC 2M 301 K. SW cloud feedbacks are shown for e) SHOC 1M and f) SHOC 2M. Values are multiplied by -1 to compare to LW cloud forcings/feedbacks. Colorbars for a-d are logarithmic.

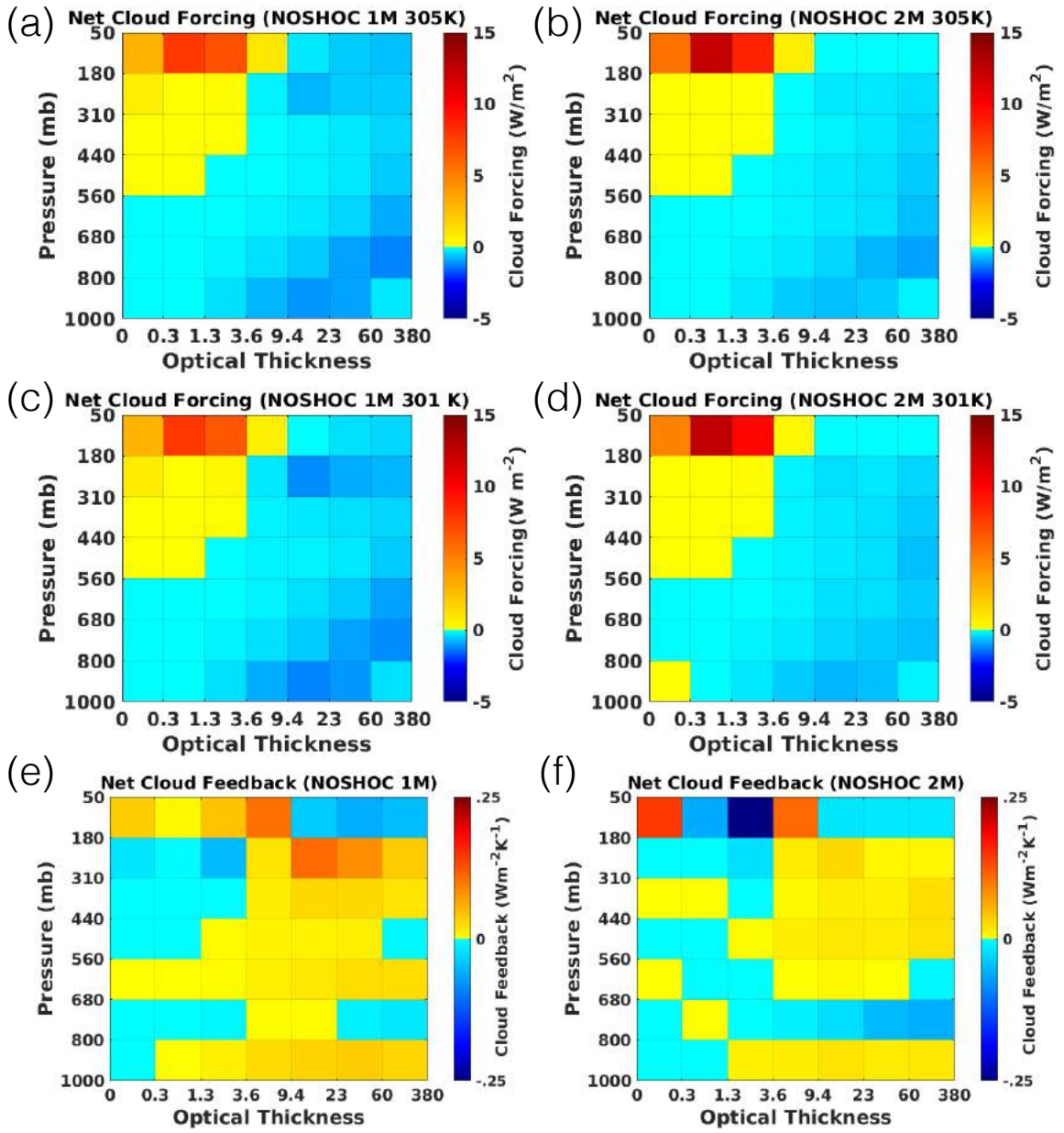

Figure 4.19. RCE 25-day averaged cloud radiative kernel derived net cloud forcing for a) NOSHOC 1M 305 K, b) NOSHOC 2M 305 K, c) NOSHOC 1M 301 K, and NOSHOC 2M 301 K. Net cloud feedbacks are shown for e) NOSHOC 1M and f) NOSHOC 2M.

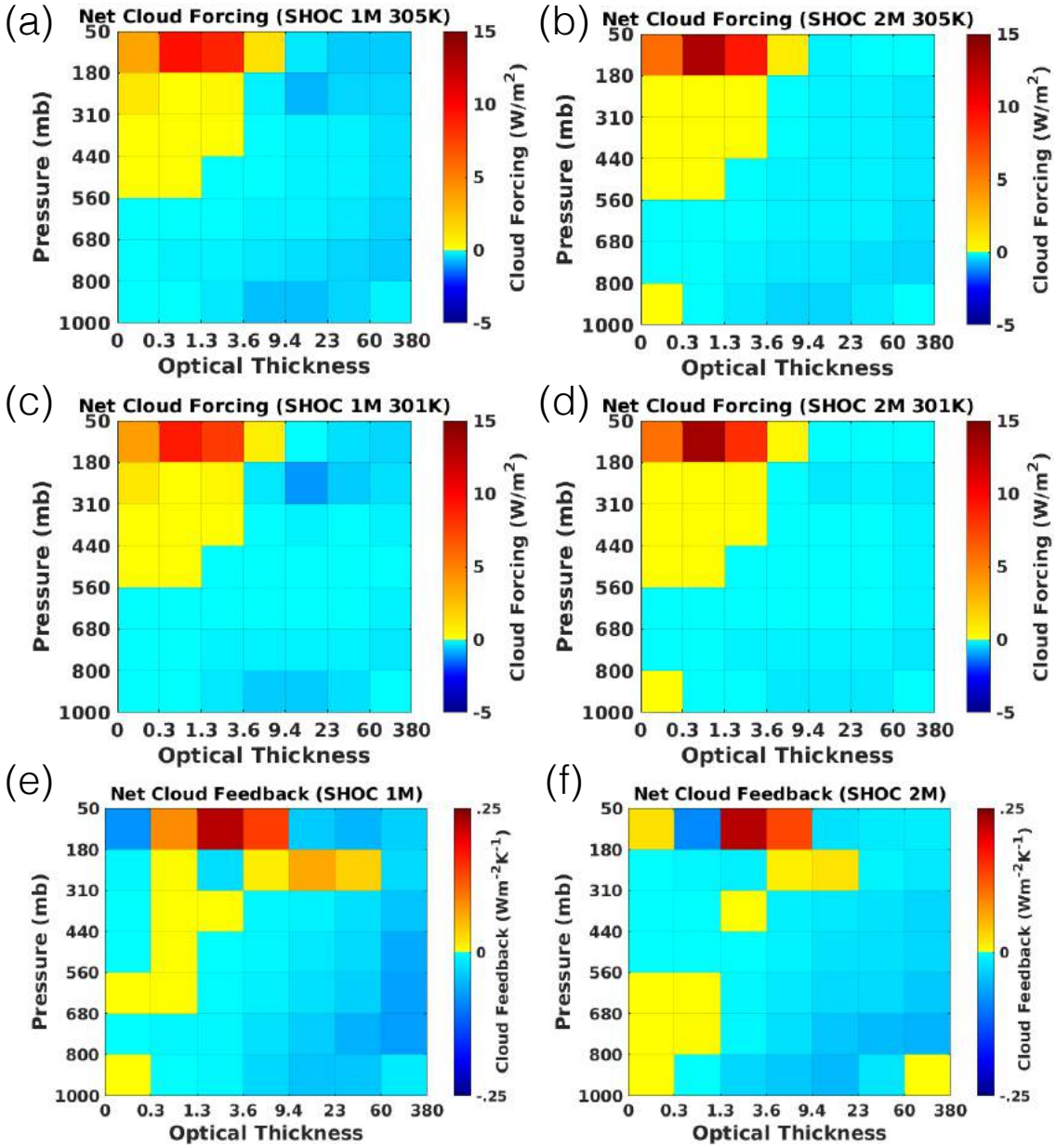

Figure 4.20. RCE 25-day averaged cloud radiative kernel derived net cloud forcing for a) SHOC 1M 305 K, b) SHOC 2M 305 K, c) SHOC 1M 301 K, and SHOC 2M 301 K. Net cloud feedbacks are shown for e) SHOC 1M and f) SHOC 2M.

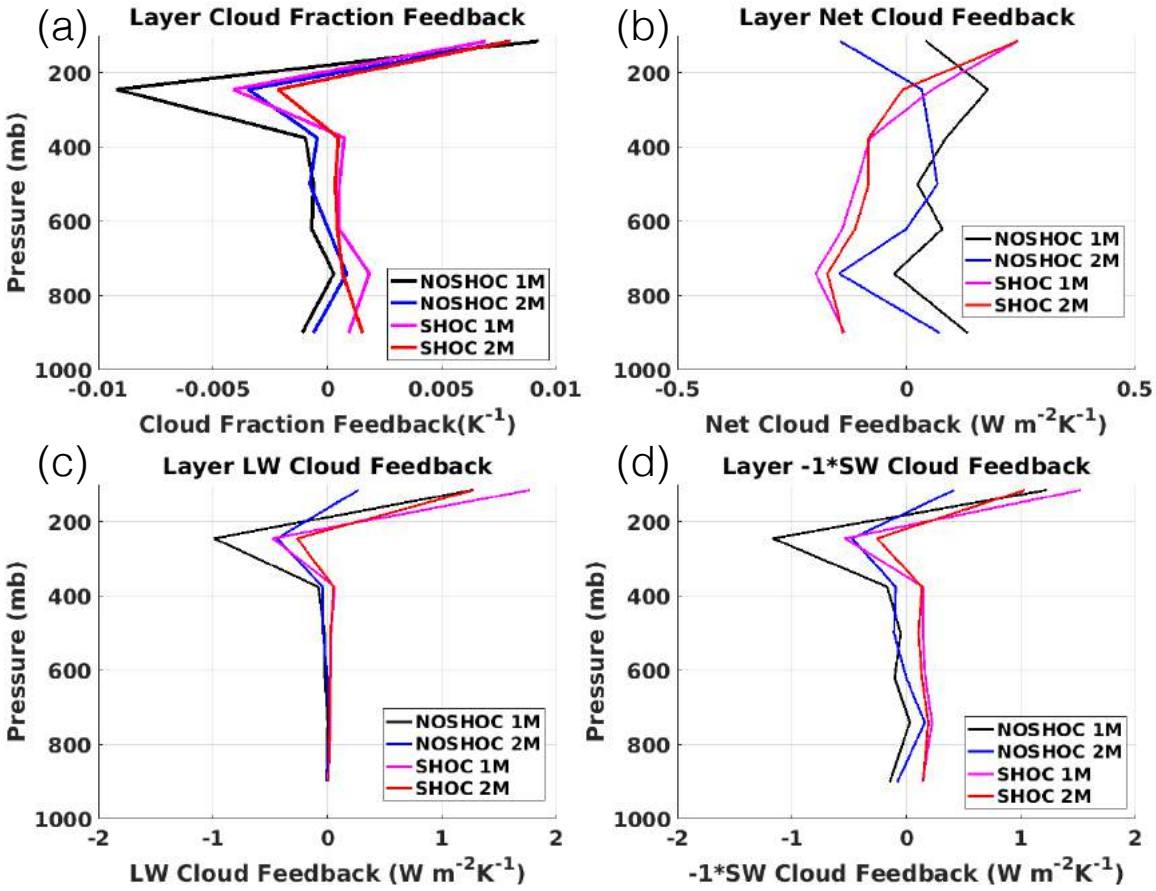

Figure 4.21. Vertical profiles of 25-day averaged cloud radiative kernel derived: a) cloud fraction feedback, b) net cloud radiative feedback, c) LW cloud radiative feedback, and d) -1 * SW cloud radiative feedback.

CHAPTER 5

DYNAMO

5.1 Background

The Madden-Julian oscillation (MJO) is the primary mode of intraseasonal variability in the Indian Ocean atmosphere (Madden and Julian, 1972). A trio of field campaigns were performed over the Indian Ocean and Western Pacific in late 2011-early 2012, the Dynamics of the MJO (DYNAMO), the Cooperative Indian Ocean Experiment on Intraseasonal Variability in Year 2011 (CINDY), and the Atmospheric Radiation Measurement (ARM) Program MJO Investigation Experiment (AMIE). A map of the sounding network used for DYNAMO/CINDY/AMIE is shown in Figure 1 in Johnson and Ciesielski (2013).

The MJO cycle features shallow nonprecipitating cumulus clouds in the suppressed phase, followed by cumulus congestus, then deep convection in the active phase, followed by stratiform precipitation (Bladé and Hartmann, 1993; Benedict and Randall, 2007). This cycle is considered a "discharge-recharge" pattern. The transition period from nonprecipitating cumulus clouds to cumulus congestus is one in which general circulation models have struggled due to a lack of moistening the troposphere by the shallow convection (Del Genio et al., 2012). In the observations, the Aqua Advanced Microwave Scanning Radiometer for Earth Observing System (EOS) (AMSR-E) found a moistening of 5 mm of precipitable water during the transition from shallow cumulus to deep convection.

5.2 Methodology

In this study, SAM with SHOC is tested to see if it adequately represents shallow cumulus during DYNAMO. During the DYNAMO field campaign, there are suppressed periods of convection in early October and in early to mid November (Johnson et al., 2015). Observations set up on Addu Atoll will be used as the target for the model; however, the observations from vertically profiling radars are only one location while a model covers a larger area with many points from which profiles can be taken so the uncertainty in the

model over the domain will be used to see if the model significantly deviates from the observations.

The cloud resolving model forcings that will be used in this study were based on the AMIE-Gan ECMWF analysis[1] and TRMM precipitation radar estimates using a constrained variational analysis (Zhang and Lin, 1997; Zhang et al., 2001). Fluxes and moisture tendencies including the ECMWF forcings have been evaluated in DYNAMO analysis (de Szoeke et al., 2015; Hannah et al., 2016). Sea-surface temperatures are based on the NOAA 1/4° daily Optimum Interpolation Sea Surface Temperature (OISST) satellite product (Reynolds et al., 2007; Reynolds, 2009).

Case studies were selected by analyzing many different satellite and ground-based observational imagery and measurements on Addu Atoll including Gan Island, which is the southernmost island in the Maldives. The Gan Island ARM mobile facility was located at 0° 41′ S, 73° 9′ E. The ARM Mobile Facility (AMF) KAZR radar and S-Pol radars are approximately 9 km apart and mapped as shown in Figure 1 of Feng et al. (2014). The 9 October 2011 to 30 November 2011 range was considered in search of periods with shallow cumulus with preferences for less upper-level cloud and less extensive precipitation. In the end, periods from 00z 13 October 2011 to 12z 14 October 2011 and 00z 4 November 2011 to 00z 7 November 2011 were selected to be the two cases. Based on the Johnson et al. (2015) analysis, the first case is slightly after the transition from a suppressed MJO to a more active convective period. The second case is in the suppressed MJO period in early November. The imagery and data used to come to these choices are covered below from larger scales down to smaller scales.

One satellite-based option for viewing the region is Meteosat, a geostationary satellite providing visible imagery which is shown for Cases 1 and 2 in Figure 5.1 and Figure 5.2, respectively (UCAR/NCAR - Earth Observing Laboratory, 2012). The resolution is quite low, though the main thing is to avoid periods dominated by either broad precipitation coverage or deep convection which is frequent in the Maldives. For Case 1 the main areas of precipitation stay north and south during daylight hours except for the increase in precipitation towards the 8-12z range on the 14th. For Case 2 daytime cloud coverage is

[1] https://www.arm.gov/news/data/post/21983

very light throughout the three days with a slight uptick on the 6th.

Another source of satellite information used to help identify potential case studies was from the Moderate Resolution Imaging Spectroradiometer (MODIS) (Barnes et al., 1998) on the Terra and Aqua satellites. The Terra satellite scans from north to south during the morning hours and the Aqua satellite scans from south to north during the afternoon hours covering roughly the same areas at roughly the same times each day. Imagery was obtained from the Land, Atmosphere Near real-time Capability for the Earth Observing System (LANCE) NASA Rapid Response System (Sohlberg et al., 2001). An example of each at 2 km resolution is shown in Figure 5.3 for the first case, October 13th and 14th. The boxed area, which includes Addu Atoll, has scattered cumulus on the morning image from the 13th, while the afternoon image on the 14th has broader cloud coverage near the onset of precipitation at Gan.

MODIS imagery for the second case, on November 5th and 6th, is shown in Figure 5.4. On the 5th, there is very little cloud coverage over the area with isolated cumulus. On the 6th, cloud cover is more significant in area and depth including congestus clouds.

These MODIS images can be viewed with resolution as high as 250 m. However, along the sides of the 2 km images the picture quality degrades as one moves to higher resolution. For each of these cases, one image has been selected to zoom in to 250 m resolution and those are shown in Figure 5.5 for a) 0845z 14 October 2011 and b) 0850z 6 November 2011. The domains shown in these images are approximately the area from the red boxes in the previous figures. The blue boxes highlight Addu Atoll, with Gan Island as the southernmost island that makes up Addu Atoll. In Case 1 this is late in the 36 hr period when deeper convection is moving into the area. In Case 2, the MODIS image is from the third day with shallow cumulus clouds near Addu Atoll and in the surrounding region.

Total Sky Imager data were used to get a ground-based visual on the cloud cover during the case periods (Morris, 2005; ARM Climate Research Facility, 2011b). Gan Island Total Sky Imager observations are shown for the two cases in Figure 5.6 and Figure 5.7. For Case 1, the morning of 13 October had a layer of altostratus early on (not shown) which moved out of the area. By 0430z (Figure 5.6a) cloud coverage had decreased significantly with just occasional cirrus. By midday (Figure 5.6b), patchy cirrocumulus clouds passed

over the station. Afternoon convection in the form of lower level cumulus occurred later in the day (Figure 5.6c). Early in the morning of the 14 October, a brief shower passed over Gan Island, after which low-level stratus passed through until mid morning (not shown). Through the late morning into the afternoon, cumulus clouds could be seen developing in the view of the sky imager at more distant regions (right sides of Figure 5.6d-e). Cumulus developed further during the afternoon resulting in broader coverage (Figure 5.6f), deeper convection, and rainfall towards the end of the daytime hours.

For the first day of Case 2, 4 November, the morning began with clear skies. Throughout the day cumulus clouds would form while increasing in coverage to partly cloudy conditions (Figure 5.7a-b). Later in the afternoon cirrus clouds moved through the Addu Atoll area. Similar conditions continued for the following two days except for a temporary decline in cloudiness midday on the 5th (Figure 5.7c-d).

Combined Remote Sensing Retrieval (CombRet) data were used for radar reflectivity observations, downloaded from ARM (ARM Climate Research Facility, 2011a). This choice was made due to the Mie scattering that occurs in Ka-band radar data when precipitation sized particles are present. CombRet retrievals are based on combinations of KAZR and S-Pol radars. The S-band radar data helps mitigate the Mie scattering effects on the radar reflectivity of Ka-band radars. Accounting for this is trivial for comparing shallow cumulus clouds but does influence precipitation comparisons between observations and the model. KAZR data have been used to improve understanding of stratiform and convective processes in DYNAMO/AMIE through high temporal resolution measurements (Deng et al., 2014). KAZR Active Remote Sensing of Clouds (ARSCL) data were used in the generation of CombRet retrievals.

ARSCL value added products have been used to provide high-resolution in vertical and time measurements of cloud properties (Clothiaux et al., 2000; Clothiaux et al., 2001). Issues with the ARSCL products have been identified over time, though many of these issues are addressed in the development of more recent KAZR-ARSCL data which is replacing the millimeter cloud radar (MMCR) versions (Kollias et al., 2005, 2016).

The S-Pol is a National Center for Atmospheric Research (NCAR) dual-polarimeteric, dual-frequency (S and Ka band) radar (Keeler et al., 2000) though only the S band is used for CombRet. It is capable of providing highly detailed cloud and precipitation

measurements. Quality control of the S-Pol includes removing ground clutter (Hubbert et al., 2009a,b).

Taking these two together the KAZR-ARSCL is primarily contributing to the periods without moderate precipitation in CombRet while the S-Pol is responsible for the heavier precipitating periods. In Feng et al. (2014) methods from PNNL COMBRET (Zhao et al., 2012; Comstock et al., 2013) were combined with a merging method based on WSR-88D and ARM Southern Great Plains (SGP) millimeter cloud radar data (Feng et al., 2009) to produce the final product.

CombRet data for Case 1 are shown in Figure 5.8. Reflectivity values for this set of plots are limited to values above -40 dBZ to reduce possible issues with radar sensitivity. Shallow cumulus develops through the daytime hours of 13 October (day 286.0-286.5). The period of shallow convection is focused on in Figure 5.8b. During the night a few periods of deeper clouds and rain showers occur at Gan Island. On the 14th the morning has cumulus present at just over 2 km, however towards the end of the day deeper convection develops and another period of rain showers occur.

The Case 2 period is a much simpler case for shallow cumulus conditions as shown in the CombRet data of Figure 5.9. There is little precipitation during the three day period and minimal high clouds (not shown). However, the first day, 4 November, includes almost no shallow cloud cover detected by the CombRet. From 12z 5 November to 00z 7 November shallow cumulus is more frequent at Gan. Periods from day 309.5-310.0 and 310.2-310.6 are highlighted in Figure 5.9b and Figure 5.9c.

CombRet data are generated by combining KAZR and S-Pol reflectivity data. To see the merging of the two sources, the three are shown together for Case 1 in Figure 5.10. The CombRet reflectivity looks much closer to the KAZR reflectivity than the S-Pol reflectivity, primarily because the S-Pol reflectivity takes measurements at a much lower frequency than the KAZR. The primary difference between CombRet and KAZR is the reflectivity in precipitating periods which is higher in the CombRet, derived largely from what the S-Pol is observing, particularly in the lowest 2 km around day 286.75.

For Case 2, the differences between the CombRet and the KAZR radar data are extremely minor (Figure 5.11). Without the precipitation in Case 1, the primary influence of the S-Pol reflectivity on CombRet does not appear. The S-Pol data does show clouds at the

same times as the KAZR but also frequent low level reflectivity returns at around half a km in addition to returns around 2.5 km which the KAZR does not show.

SAM model runs were used to investigate this pair of cases which span from day 286-287.5 (00z 13 October - 12z 14 October) and day 308-311 (00z 4 November - 00z 7 November). The SAM model capability of handling shallow cumulus for varying grid spacing with SHOC is investigated. These model runs are described in Table 5.1. The domain was made larger in the 2 km runs so that the grid would still have 32 grid points in the horizontal. The 0.5 km and high resolution 0.1 km horizontal grid spacing runs also had a decreased grid spacing in the vertical. The model runs were performed using the SHOC turbulence parameterization scheme and the double-moment Morrison et al. (2005) microphysics.

5.3 Results

Cloud water path for the 0.5 km model runs of the respective cases are shown in Figure 5.12 and Figure 5.13. The plots show time at evenly spaced intervals (5 hrs for Case 1, 10 hrs for Case 2) throughout the 36 hr and 72 hr runs. Case 1 took approximately 6 hrs to generate cloud while Case 2 took approximately 12 hrs. From those points onward clouds existed in the model domain for most timesteps although both briefly drop to virtually no cloud water path. Cloud cover was generally higher in Case 1 albeit at low fractions in both. Both cases had isolated cumulus; the largest clouds in either Case had horizontal extents of a few km.

Comparing model output to the CombRet reflectivities first requires converting model output to reflectivity values. This is done by evaluating the gamma functions of the particle size distributions for cloud and precipitation particles as is done in the Morrison scheme (Morrison et al., 2009). The Morrison gamma function for cloud and precipitation particle size distribution, N(D), is

$$N(D) = N_0 D^{\mu} e^{-\lambda D} \tag{5.1}$$

where D is the particle diameter. λ and N_0, the slope and intercept parameters, are given by the following in the Morrison method.

$$\lambda = \left[\frac{cN\Gamma(\mu+d+1)}{(q\Gamma(\mu+1))}\right]^{\frac{1}{d}} \tag{5.2}$$

$$N_0 = \frac{N\lambda^{\mu+1}}{\Gamma(\mu+1)} \tag{5.3}$$

Morrison identfies c and d as parameters from the power-law mass-diameter relationship m=cD^d. c = $\pi\rho_j/6$ for the jth species and d = 3 for all species. For all species except cloud water, μ is 0. For cloud water μ is calculated as a function of N_c concentration and air density (Martin et al., 1994). Γ is the Euler gamma function.

To get the equivalent Rayleigh reflectivity size distribution, the 6th power of the melted equivalent diameter is multiplied by the particle size distribution (Stanford, 2016). The melted equivalent diameter is described in Stanford (2016) as:

$$D_{eq} = \left[\frac{6c}{\pi\rho_w}\right]^{\frac{1}{3}} D^{\frac{d}{3}} \tag{5.4}$$

which for liquid water leads to D_{eq} = D while for ice particles D_{eq} = [ρ_j / ρ_w]$^{1/3}$D. This results in Rayleigh reflectivity size distributions of

$$Z_e(D) = 0.224x10^{18}[\frac{6c}{\pi\rho_w}]^2 D^{2d} N(D) \tag{5.5}$$

for ice species and

$$Z_e(D) = 1x10^{18} D^6 N(D) \tag{5.6}$$

for liquid species (Stanford, 2016). The extra 0.224 factor in the ice species is taking into account the dielectric factor, as shown in Smith (1984).

Integrating these obtains the following equations for the reflectivity of ice species

$$Z_e = 0.224x10^{18} N\lambda^{1+\mu}\lambda^{-1-\mu-2d}[\frac{6c}{\pi\rho_w}]^2 * \frac{\Gamma(2d+\mu+1)}{\Gamma(\mu+1)} \tag{5.7}$$

and for liquid species

$$Z_e = 1x10^{18} N\lambda^{1+\mu}\lambda^{-1-\mu-2d}\frac{\Gamma(2d+\mu+1)}{\Gamma(\mu+1)} \tag{5.8}$$

as described in Varble (2013).

Determining whether the model runs are capable of representing the observations when the observations are from one point requires determining the range of what the model is seeing over the domain throughout the period and evaluating whether it is comparable

to the observations. A simple way to do this is to look at time-height cross-sections for a variety of points in the model domain. This is shown at 16 evenly spaced points for Case 1 at each grid size. Reflectivities are shown, as for the CombRet data above, for values greater than -40 dBZ to maintain the same range and colorbar.

For the 2 km grid spacing Case 1 run, the time-height cross-sections are shown in Figure 5.14. There is a wide range of results with some locations having multiple instances of precipitating convection while other locations have no instances of precipitation reaching the ground. The main precipitation periods are around day 286.5, around day 287, and just before the end of the run. This matches up somewhat closely to the CombRet reflectivity which shows precipitation primarily around days 286.75, just before 287, and just before the end of the Case period. Shallow cumulus occurs at all 16 locations throughout most of the period. Cloud cover is non-existent in the first few hours of the simulation.

The 1 km grid spacing Case 1 run time-height cross-sections are shown in Figure 5.15. All 16 points in this run had precipitation reaching the ground at some point in the 36 hr period. The precipitation periods in the 1 km run seem on average to be somewhat less frequent but of a longer duration comparing this 16 point sample to the one from the 2 km grid run. The timing of precipitation, on the other hand, is pretty close to having the same periods as the CombRet. Shallow cumulus presence and initial cloud time is also similar to the 2 km run.

The 0.5 km grid spacing Case 1 run time-height cross-sections are shown in Figure 5.16. Most of the 16 points had precipitation reaching the ground at some point in the 36 hr period ranging from 0 to 6 instances of precipitation. Shallow cumulus again shows up in all of the points and like the others it takes several hours for the model to generate cloud.

The same set of plots were made for the three Case 2 runs with model output for three runs of Case 2 are shown in Figure 5.17 for 2 km, Figure 5.18, for 1 km, and Figure 5.19 for 0.5 km. Precipitation is much less frequent for Case 2. In the 2 km run only approximately half of the 16 points show precipitation reaching the surface during the three day period. Shallow cumulus occurs over the three day period at a less frequent rate than in Case 1. The model also takes longer to generate any cloud presence, almost half a day. The 1 km and 0.5 km runs tell similar stories for precipitation, shallow cumulus, and initial cloud

time.

For each of the runs, profiles have been made of the percentage of time the reflectivity exceeds threshold values. For the Case 1 2 km run, profiles of the reflectivity exceedence percentage (hereafter referred to as REP) are shown in Figure 5.20. These profiles are for the latter 30 hrs of the 36 hr run due to removing the initial model period before any clouds are generated. Reflectivity thresholds of -40, -30, and -20 dBZ are used to deal with any potential issues with CombRet sensitivity at the lowest reflectivities. Means, mean +- 1 and 2 standard deviations, and maximum and minimum values are plotted for the simulation using the entirety of the model domain. As a result there is a wide range of individual point profiles going into the 32 x 32 grid point averages.

The altitude with the highest mean REP values is around 700 m, exceeding the -40 dBZ threshold roughly 17% of the time. This is the region where shallow cumulus clouds developed at all points in the 16-panel figures for all of the Case 1 model runs. Mean REP values drop off to around 10% by 1.5 km. Increasing the reflectivity threshold decreases the magnitude of this drop off from 700 m to higher altitudes. The CombRet data does not have a similar maximum REP around 700 m, but ranges from 15-20% (for the -40 dBZ threshold) from 1 km up through 4 km. Through the lowest km, the CombRet is close to the model average for all three thresholds. From 1-2 km for the -40 dBZ threshold, and 1-4 km for the higher thresholds, the observations are close to the +1 standard deviation profile, eventually exceeding it. At higher elevations there may be more influence from advection into the region, particularly in this case where midlevel clouds occurred. While there are the differences noted, the 2 km grid spacing run appears reasonable compared to the observations.

The 1 km run of Case 1 has REP profiles shown in Figure 5.21.The 1 km profiles have a similar shape to those for the 2 km model run and a similar maximum mean REP altitude. However, the 1 km model profiles have slightly higher percentages across the 0-4 km range than the 2 km model run. As a result, the model average is higher than the observations for the lowest 800 m for the -40 dBZ threshold run. Above that the CombRet stays within the +1 standard deviation range, aside from the brief deviation at roughly 2300 m for the -40 dBZ threshold, for higher altitudes than the 2 km run. The 1 km grid spacing run also seems fairly representative of the observations.

The 0.5 km run of Case 1 has REP profiles shown in Figure 5.22. The lowest 800 m model profiles are similar in shape to the 1 km run. Despite having twice as many grid points (64x64 instead of 32x32) the maximum REP value (red dots) was lower than in the 2 km or 1 km runs. The altitude of the maximum model mean REP values drops in the 0.5 km grid spacing run to a height of around 500 m for the -20 dBZ threshold. From an altitude of 1 km and higher REP values drop off much faster in the 0.5 km grid, particularly for the -40 dBZ threshold. The observational CombRet REP profile is roughly the same as the maximum REP in the entire model domain from 2.5 km to 4 km. The higher reflectivity thresholds delay the crossing of the observations with the model maximum until around 4 km. Of the three runs, the 0.5 km model run is by far the least likely to be representing the observed values reasonably above 2 km though it was reasonable in the lowest altitudes where shallow cumulus would be present.

A set of model REP profiles were made for Case 2 and are shown in Figure 5.23 for 2 km, Figure 5.24 for 1 km, and Figure 5.25 for 0.5 km. The first 12 hours were left off of these comparisons to account for the time it took the model to create the first clouds which took almost twice as long to develop cumulus as did Case 1.

For the 2 km run for Case 2 (Figure 5.23), the maximum mean REP altitude is at approximately 750 m for the -40 dBZ threshold. The magnitude of this low-level peak relative to surrounding elevations decreases as the threshold is shifted higher. For the -20 dBZ threshold the mean only reaches a maximum of around 2.5% at an altitude of almost 1 km. Similar to Case 1 the percentage decreases with altitude. In the observations CombRet does not show any notable reflectivity returns above 3 to 4 km altitude during this period while the model develops cumulus that reaches as high as 6 km which was the case for the other grid spacings as well. However, the observation dropoff to 0 is roughly in line with the -1 standard deviation line so this departure from the model mean REP profile is not inherently unreasonable. In the lower levels (< 2 km) the model does a reasonable job at representing the observations, staying primarily within 1 standard deviation. Unlike Case 1, in Case 2 the model mean tends to overestimate the cloudiness relative to the observations. CombRet with a -40 dBZ threshold does have a similar 750 m peak in occurrence, though CombRet is lower in magnitude than the model, briefly falling in the -1 to -2 standard deviation range. At higher dBZ thresholds CombRet's altitude of the

highest REP value rises to around 1.75 km for the -20 dBZ threshold.

For the 1 km run for Case 2 (Figure 5.24) the mean REP profiles are similar to the 2 km run with their primary difference being a lower magnitude peak. This trend continues for the profiles for the 0.5 km run (Figure 5.25). The 0.5 km run has a slightly higher mean REP value from an altitude of 1 to 2 km. A shorter dropoff from 750 m to 1.5 km represents a lower frequency of shallow cumulus in the lower grid spacing run which matches up closer to the observation profile. In the 1 km and 0.5 km runs the -1 standard deviation line does not drop to 0 as quickly as it does for the 2 km run.

For Case 2 the 0.5 km run performs the best for the -20 dBZ reflectivity threshold with a closer match to the observations on the altitude of maximum mean REP. All three did similarly well for the -40 dBZ reflectivity threshold.

The high-resolution 100 m runs for each case are shown in Figure 5.26. For both cases the model dramatically overestimates shallow cumulus. Every model grid point had cloud cover rates above the observations around 600 m. REP values were much higher throughout the lowest 2 km than the larger grid spacing runs but end up close to the other runs by 4 km. A 100 m run was then performed with SHOC with comparable results suggesting turbulence parameterization scheme is not a factor in this overestimate. Since both cases yielded the same result with 100 m grid runs, the overestimation of shallow cloud is unlikely to be a coincidence.

5.4 Summary and Discussion

For the DYNAMO study, cases where shallow cumulus were present in the observations were selected in order to test the models' capacity to reasonably represent shallow cumulus. Satellite imagery, sky imagery from Gan Island, and combined radar retrievals (CombRet) merging KAZR and S-Pol data were used to identify such periods. The periods selected were 00z 13 October 2011 - 12z 14 October 2011 for Case 1 and 00z 4 November 2011 - 00z 7 November 2011 for Case 2. Case 1 is during the transition from the suppressed period towards the cumulus congestus period of the MJO a few days after the CombRet retrieval data started for this field program. Case 2 is during the suppressed period in the MJO.

During the 10 October 2011 to 30 November 2011 period of DYNAMO there were

few instances where Gan Island displayed shallow cumulus in the CombRet data for an extended period without interference from other cloud types. Deep convective periods of the MJO ruled out large portions of the period and even in suppressed periods mid or upper level clouds advecting into the region, which could influence the results, were not uncommon, even during calmer periods of the MJO. CombRet data suggests shallow cumulus coverage in this period does not result in high percentages of the region covered with that cloud type. Coverage is spotty enough at times that some periods may be suitable with shallow cumulus in the region that is just not detected by ComRet when Gan is on the low end of the range of cloud cover the region sees.

Model runs were performed at 2, 1, 0.5, and 0.1 km grid spacing using double-moment microphysics and the SHOC turbulence parameterization scheme. Maps of cloud water path show isolated convection throughout both cases with a slightly higher coverage in Case 1. Time-height cross-sections of evenly spaced grid points indicated a wide range in model outcomes in precipitation and convection; however, all grid points highlighted for all model runs of both cases had shallow cumulus at some point during the model run period.

In Case 1 shallow cumulus was well represented in the simulations compared to the observations for grid sizes from 0.5 km to 2 km; however, the simulations suggest a faster dropoff in cloud fraction than the observations in the 2-4 km altitude range. The 0.5 km grid size run underestimated cloud fraction the most relative to the observations in the midlevels. A reflectivity threshold of -20 dBZ was the closest match between the simulations and observations with a smaller dropoff in cloud cover at low and midlevel simulation values which kept the observations within a standard deviation for a higher altitude than the smaller reflectivity thresholds.

In Case 2 shallow cumulus cloud fraction was overestimated in the simulations relative to the observations for grid sizes from 0.5 km to 2 km. Despite the REP falling to 0 around 3 km, a lower altitude than the simulation mean, this result is not unreasonable since it is roughly the -1 standard deviation. The 0.5 km grid size run was a closer match in this case, with a smaller peak in shallow cumulus and a closer match with the observations on the height of the cloud cover maximum for the -20 dBZ threshold.

For both cases, the LES scale 100 m resolution runs significantly overestimated shallow

convection. There are a variety of possibilities that could lead to this result. One possibility involves how radar observations show a significant frequency of low elevation returns in the S-band radar for Case 2 which are not in the KAZR and not part of the combined CombRet data. If these values were considered, that would bring the observed low-level REP values in Case 2 to over 20% which is on the high side of the simulation. However, the S-band radar also shows more reflectivity returns just below 3 km which would create a bump in the observation REP profile significantly higher than the simulated result.

There may be some uncertainties with the advective forcing. Since precipitation is used as a constraint to force the model and these cases are selected with low precipitation in mind, it is possible that the model may have some difficulty generating the correct cloud structures in the absence of precipitation.

Another possibility involves how SHOC handles cloud fraction. Since SHOC does not use an all-or-nothing scheme for cloud fraction, SHOC can identify grid boxes with fractional cloud coverage. How SHOC divides up liquid water in those grid boxes may affect what particle sizes SHOC is expecting inside the cloud.

Table 5.1. Model simulations performed for DYNAMO cases.

Case	Days	H. Spacing	Domain	# V. Levels	Lowest V. Level	V. Spacing
1	286-287.5	2 km	64 km	67	50 m	100 m
1	286-287.5	1 km	32 km	67	50 m	100 m
1	286-287.5	0.5 km	32 km	109	25 m	50 m
1	286-287.5	0.1 km	32 km	109	25 m	50 m
2	304-307	2 km	64 km	67	50 m	100 m
2	304-307	1 km	32 km	67	50 m	100m
2	304-307	0.5 km	32 km	109	25 m	50 m
2	304-307	0.1 km	32 km	109	25 m	50 m

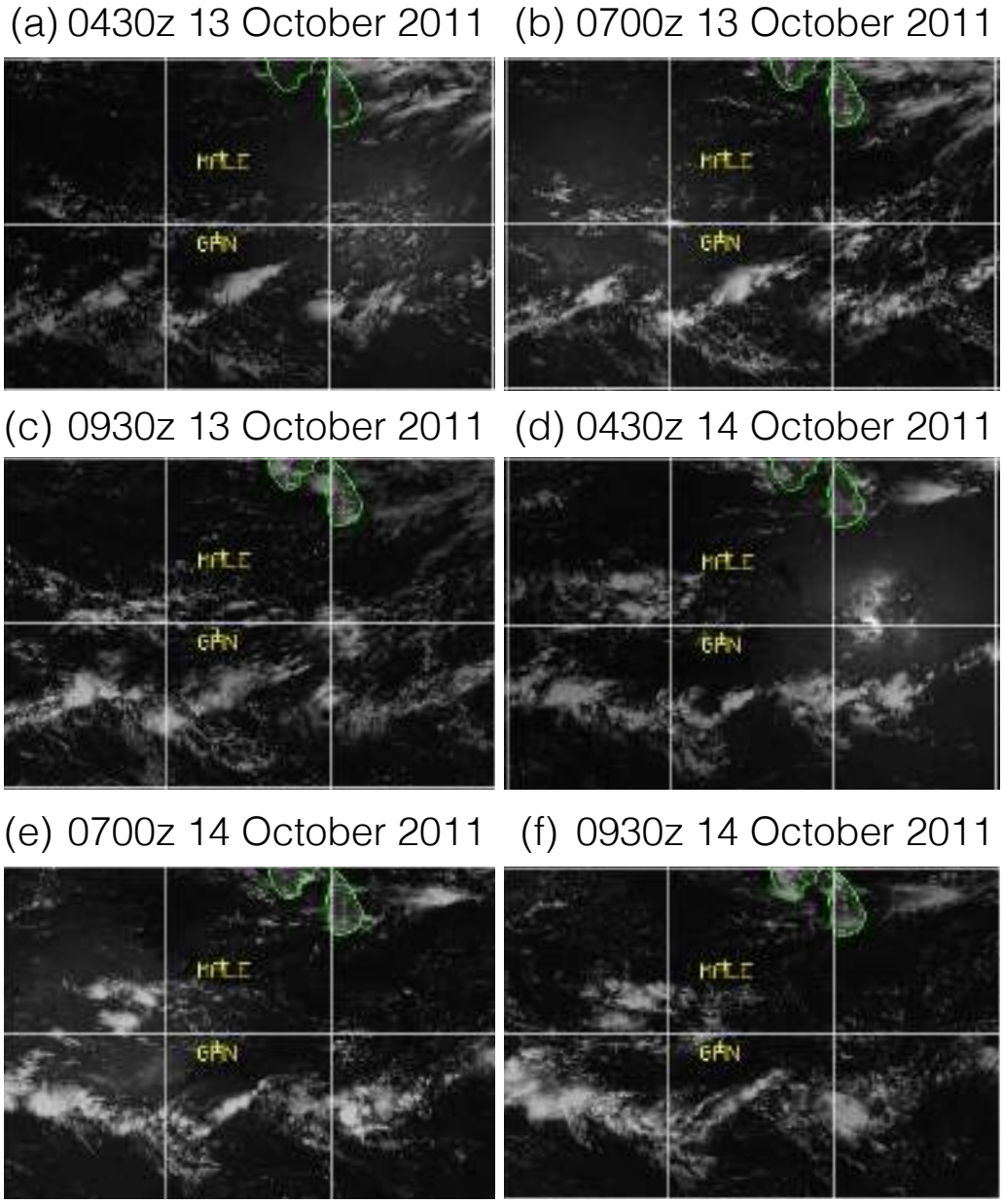

Figure 5.1. Meteosat-7 visible (channel 1) imagery for Case 1. Times selected are a) 0430z 13 October 2011, b) 0700z 13 October 2011, c) 0930z 13 October 2011, d) 0430z 14 October 2011, e) 0700z 14 October 2011, and f) 0930z 14 October 2011.

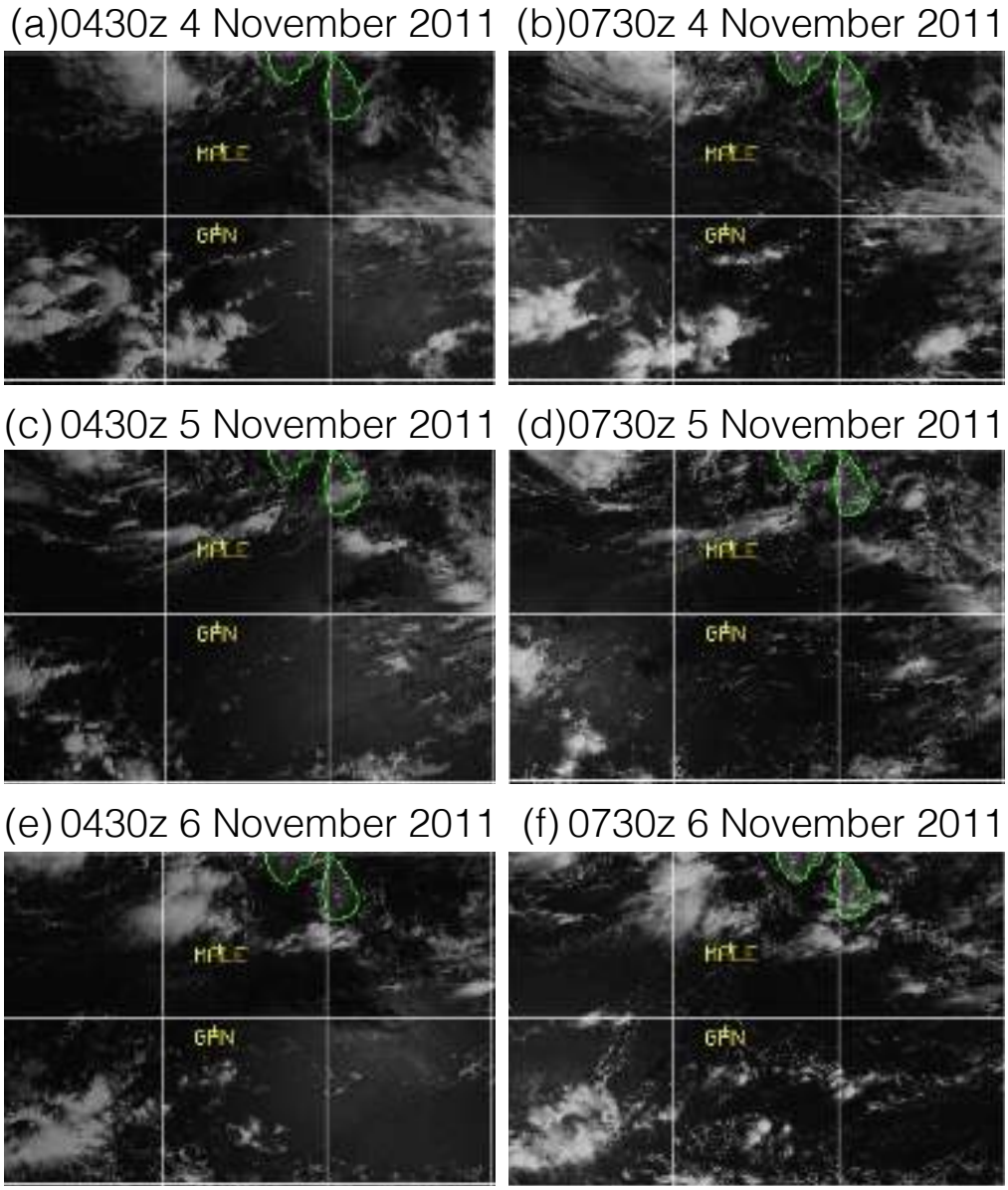

Figure 5.2. Meteosat-7 visible (channel 1) imagery for Case 1. Times selected are a) 0430z 4 November 2011, b) 0730z 4 November 2011, c) 0430z 5 November 2011, d) 0730z 5 November 2011, e) 0430z 6 November 2011, and f) 0730z 6 November 2011.

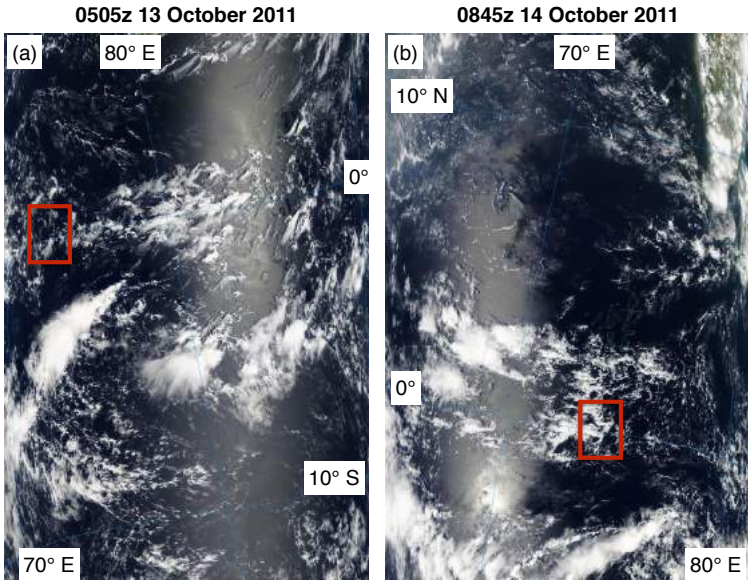

Figure 5.3. MODIS satellite imagery for DYNAMO Case 1 at 2 km resolution from NASA Rapid Refresh. Times selected are a) 0505z 13 October 2011 and b) 0845z 14 October 2011. Red boxes show the geographic area around Addu Atoll.

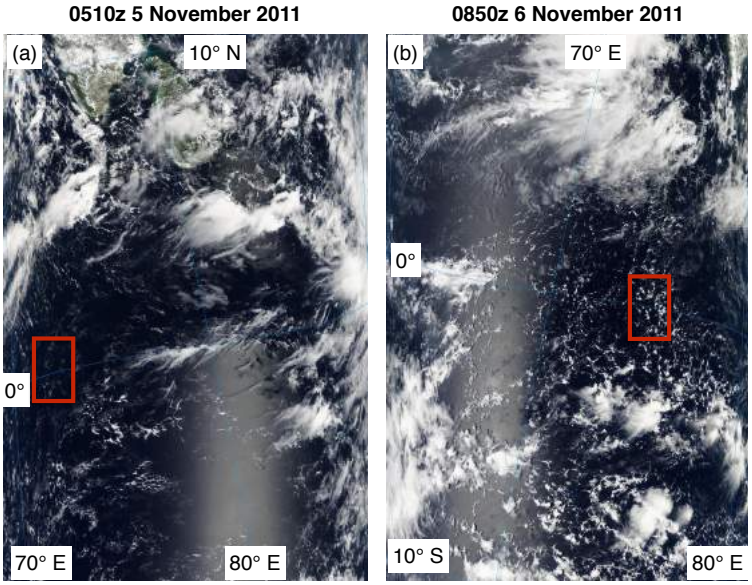

Figure 5.4. MODIS satellite imagery for DYNAMO Case 2 at 2 km resolution from NASA Rapid Refresh. Times selected are a) 0510z 5 November 2011 and b) 0850z 6 November 2011. Red boxes show the geographic area around Addu Atoll.

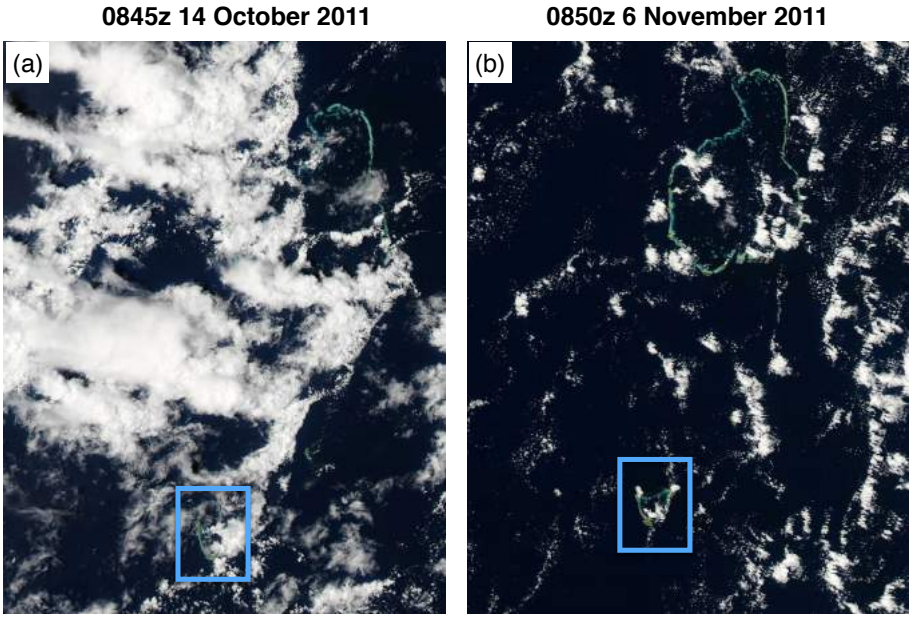

Figure 5.5. MODIS satellite imagery from NASA Rapid Refresh for a) DYNAMO Case 1 at 0.25 km resolution for 0845z 14 October 2011 and b) DYNAMO Case 2 at 0.25 km resolution for 0850z 6 November 2011. The blue box indicates the area encompassing Gan Island and Addu Atoll.

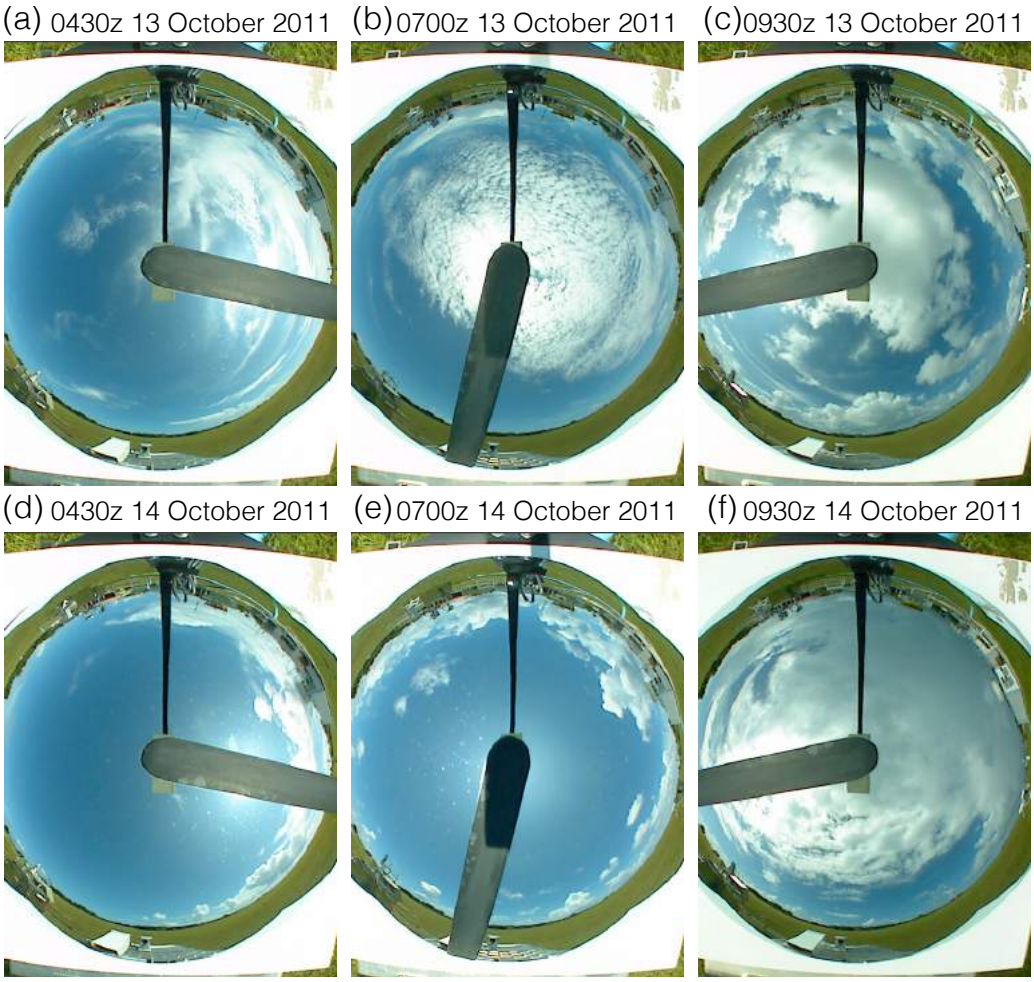

Figure 5.6. Gan Total Sky Imager observations for Case 1. Times selected are a) 0430z 13 October 2011, b) 0700z 13 October 2011, c) 0930z 13 October 2011, d) 0430z 14 October 2011, e) 0700z 14 October 2011, and f) 0930z 14 October 2011.

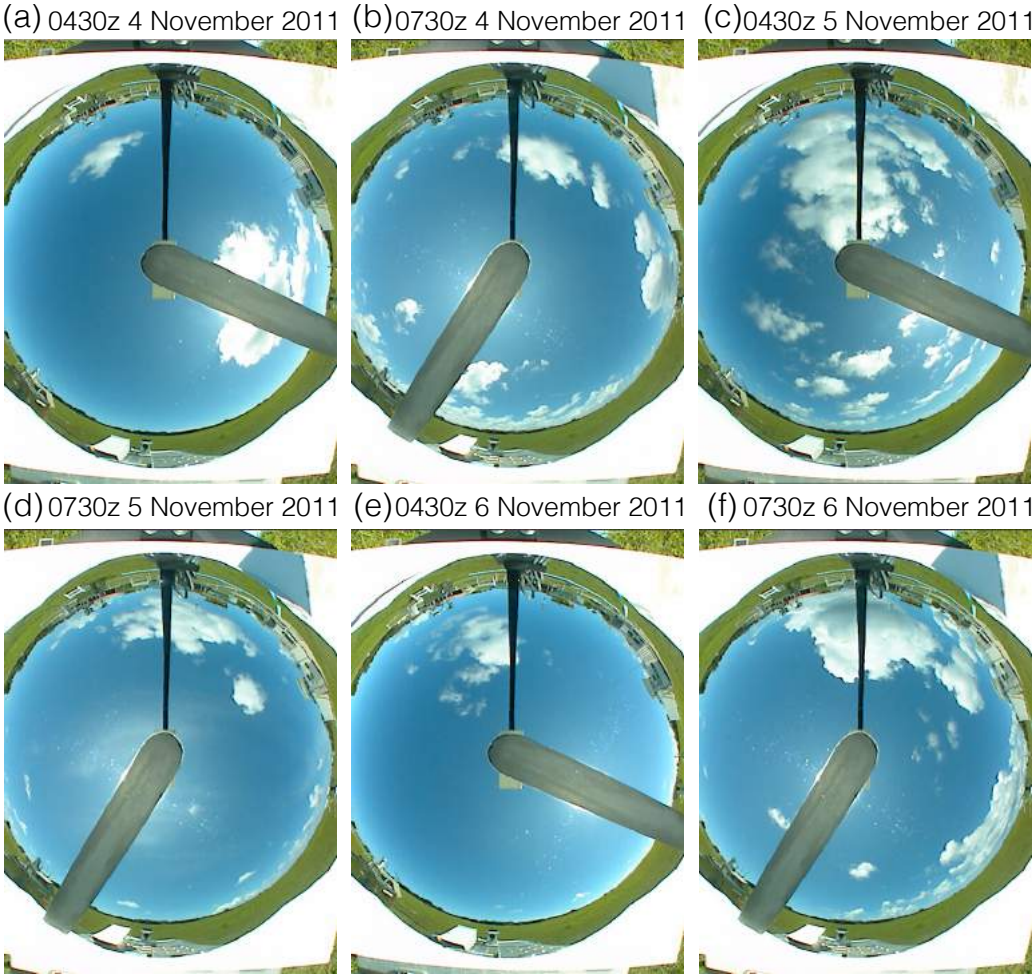

Figure 5.7. Gan Total Sky Imager observations for Case 1. Times selected are a) 0430z 4 November 2011, b) 0730z 4 November 2011, c) 0430z 5 November 2011, d) 0730z 5 November 2011, e) 0430z 6 November 2011, and f) 0730z 6 November 2011.

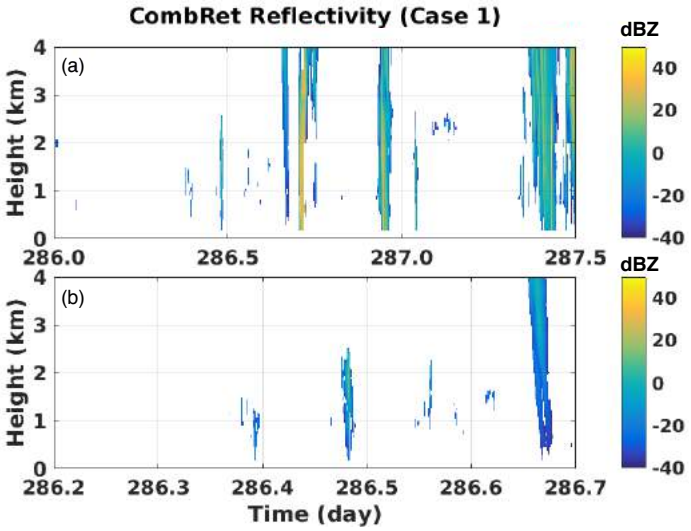

Figure 5.8. CombRet reflectivity observations at Gan Island for Case 1, from a) day 286-287.5 (00z 13 October 2011 to 12z 14 October 2011) and b) day 286.2-286.7.

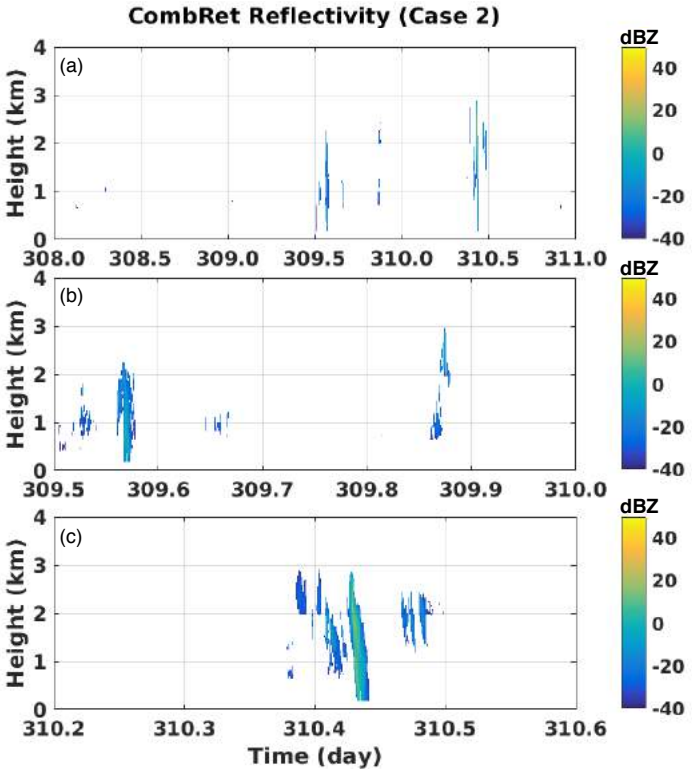

Figure 5.9. CombRet reflectivity observations at Gan Island for Case 2, from a) day 308-311 (00z 4 November 2011 to 00z 7 November 2011), b) day 309.5-310, and c) day 310.2-310.6.

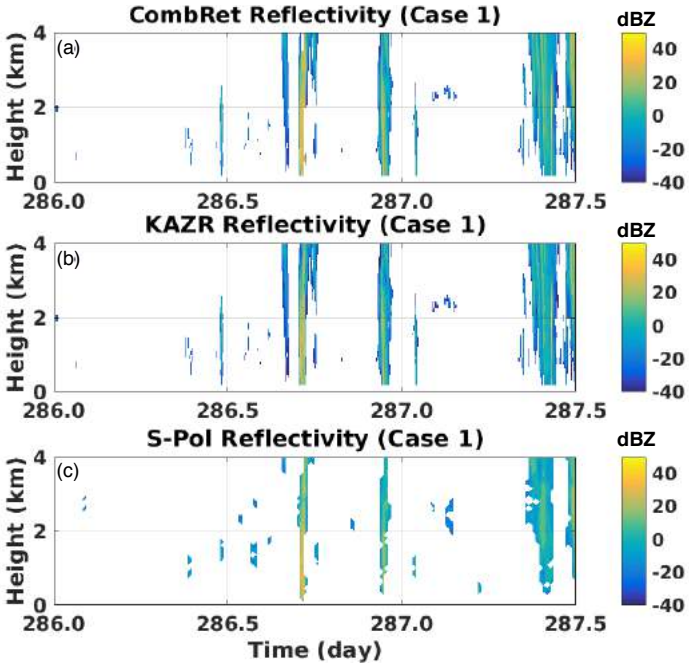

Figure 5.10. Reflectivity observations at Gan Island for Case 1, day 286-287.5 (00z 13 October 2011 to 12z 14 October 2011) from a) CombRet, b) KAZR, and c) S-Pol.

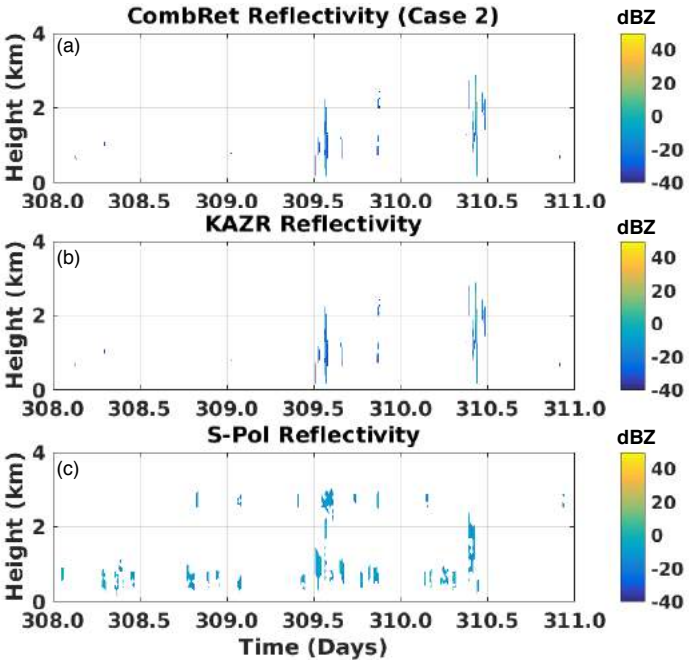

Figure 5.11. Reflectivity observations at Gan Island for Case 2, day 308-311 (00z 4 November 2011 to 00z 7 November 2011) from a) CombRet, b) KAZR, and c) S-Pol.

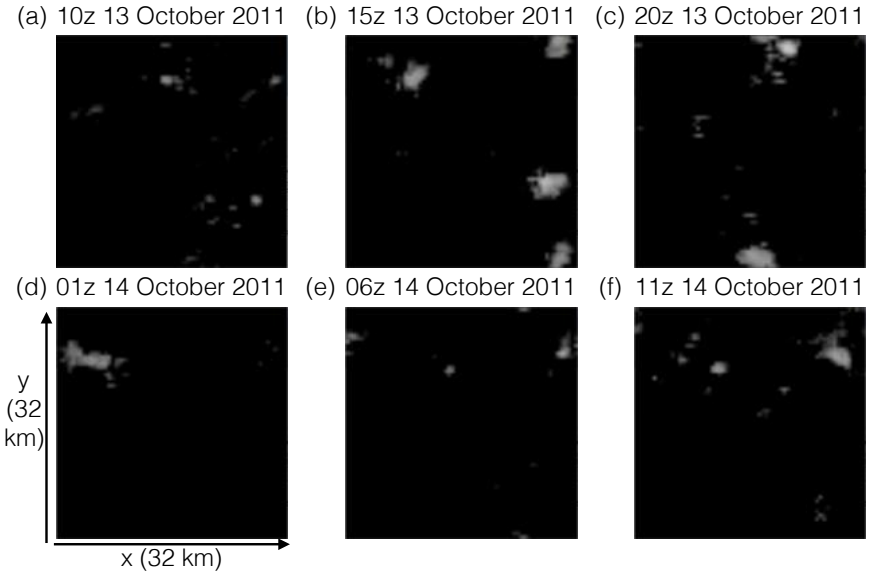

Figure 5.12. CWP domains for the 0.5 km grid size Case 1 run. Times selected are a) 1000z 13 October 2011, b) 1500z 13 October 2011, c) 2000z 13 October 2011, d) 0100z 14 October 2011, e) 0600z 14 October 2011, and f) 1100z 14 October 2011.

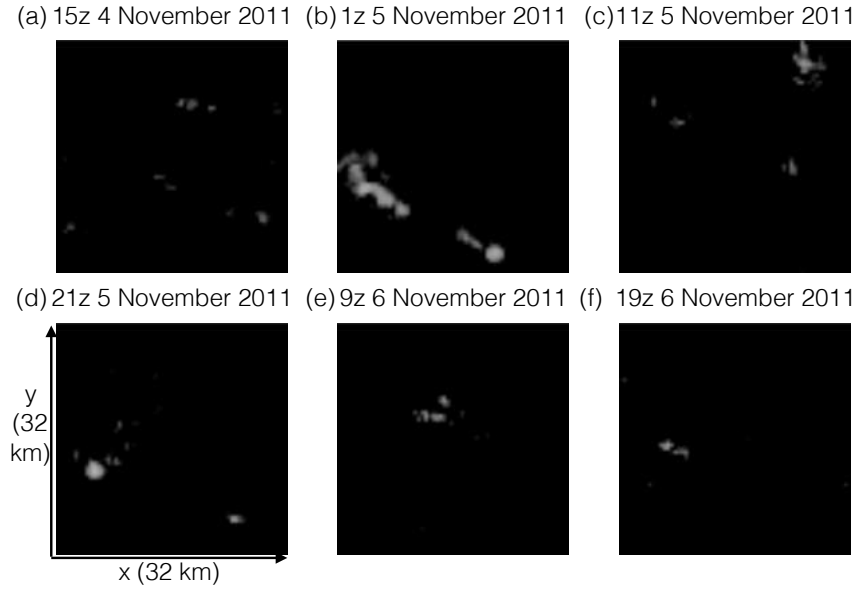

Figure 5.13. CWP domains for the 0.5 km grid size Case 2 run. Times selected are a) 1500z 4 November 2011, b) 0100z 5 November 2011, c) 1100z 5 November 2011, d) 2100z 5 November 2011, e) 0900z 6 November 2011, and f) 1900z 6 November 2011.

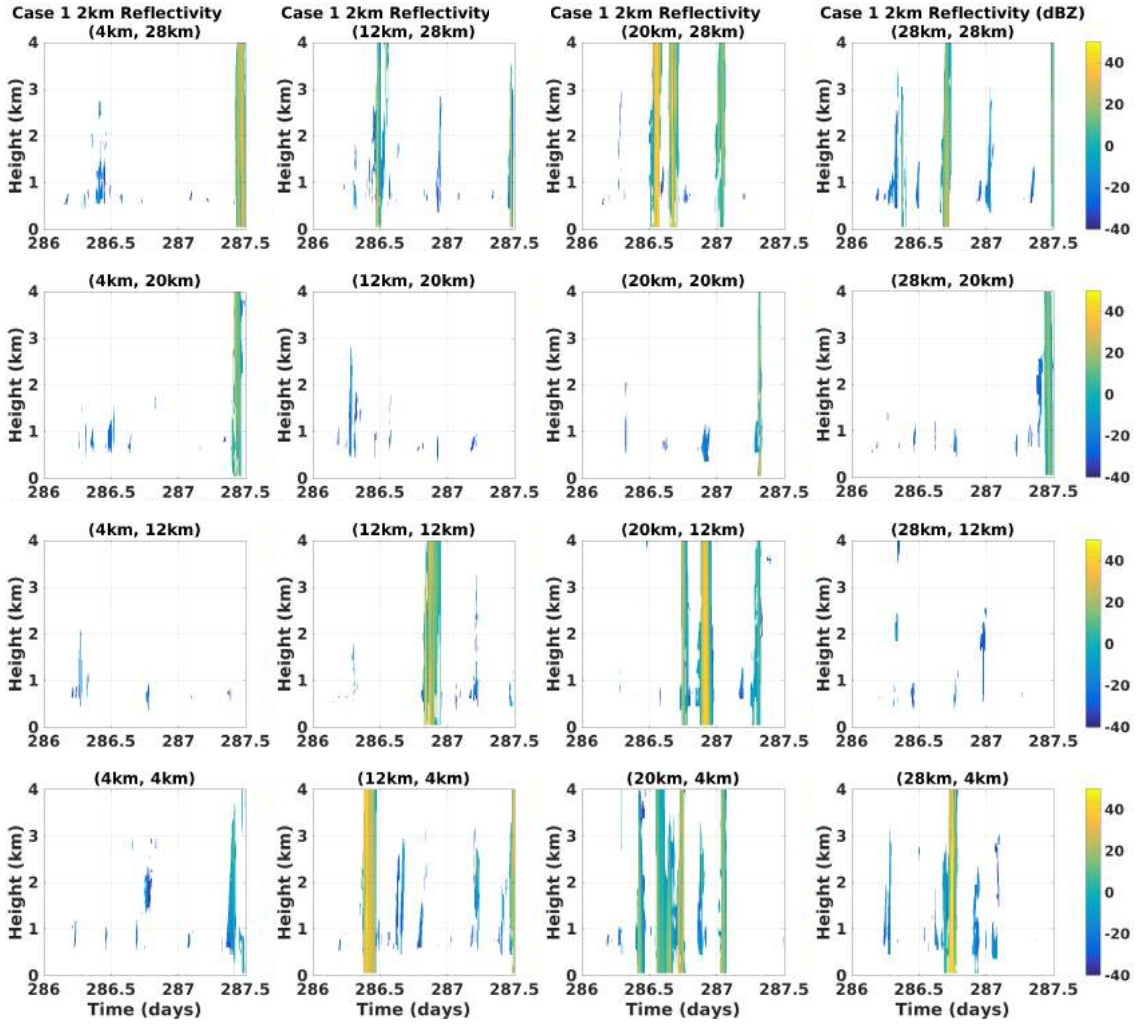

Figure 5.14. Time-height reflectivity from 16 evenly spaced points for the 2 km grid Case 1 model run.

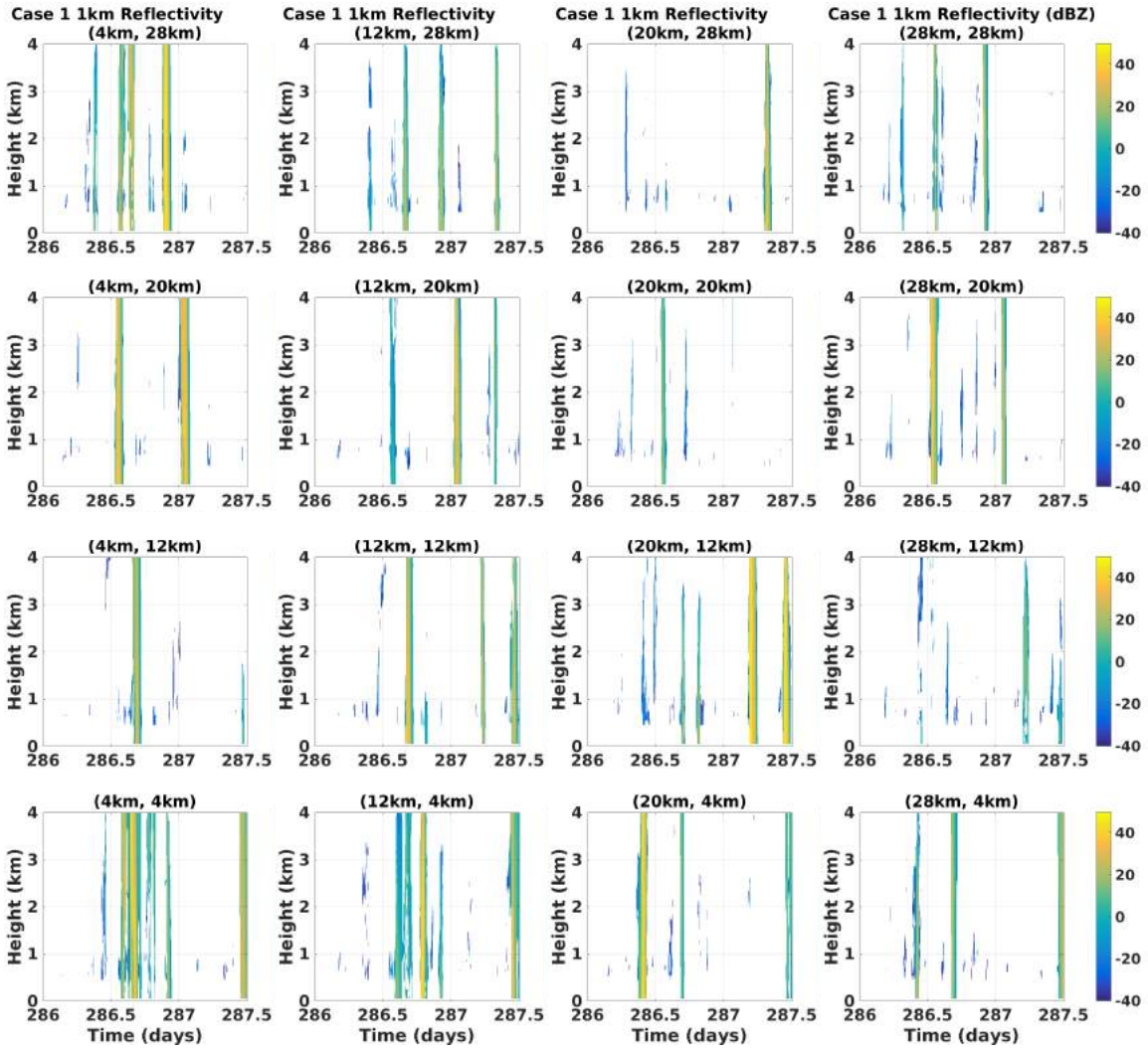

Figure 5.15. Time-height reflectivity from 16 evenly spaced points for the 1 km grid Case 1 model run.

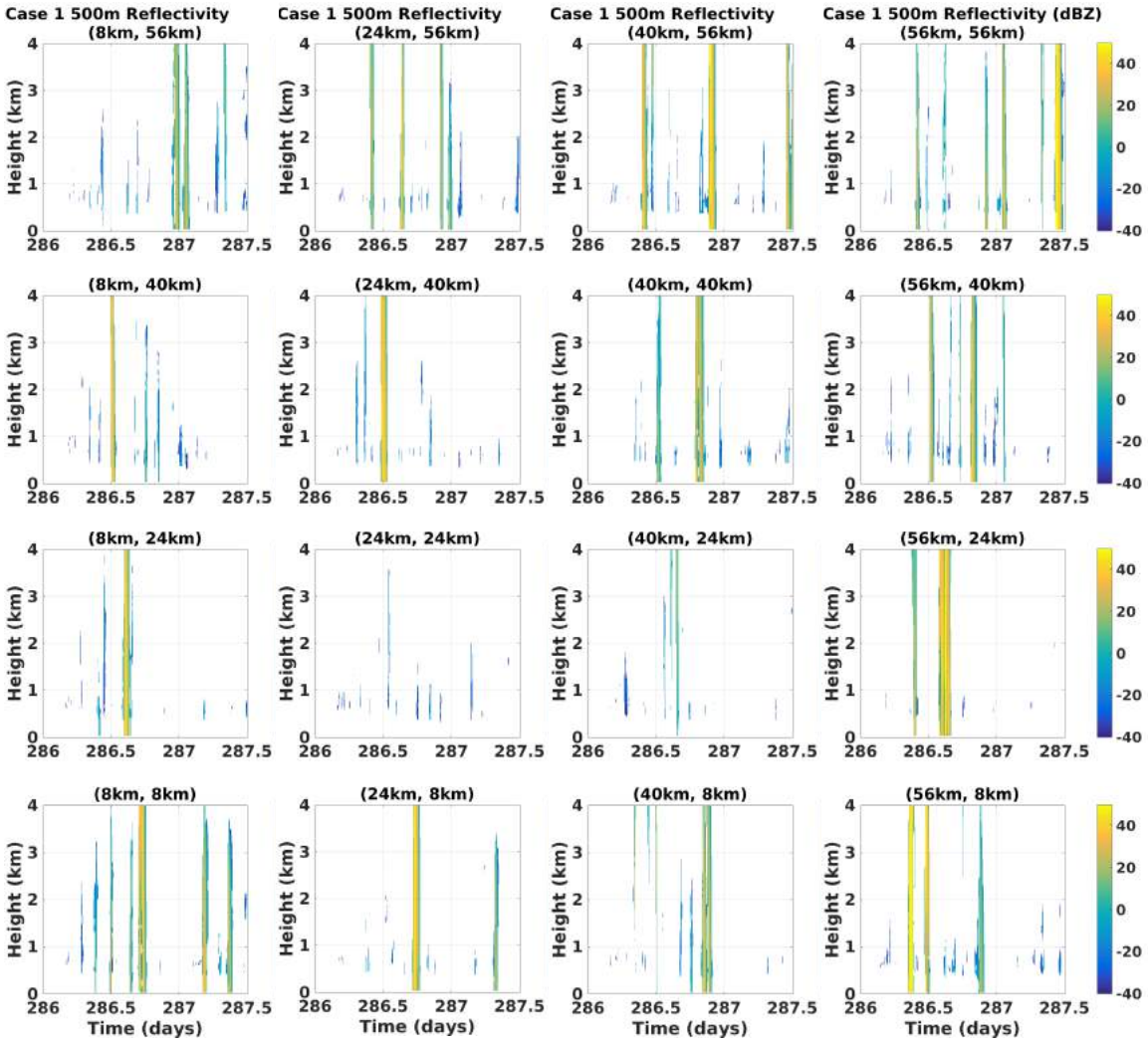

Figure 5.16. Time-height reflectivity from 16 evenly spaced points for the 0.5 km grid Case 1 model run.

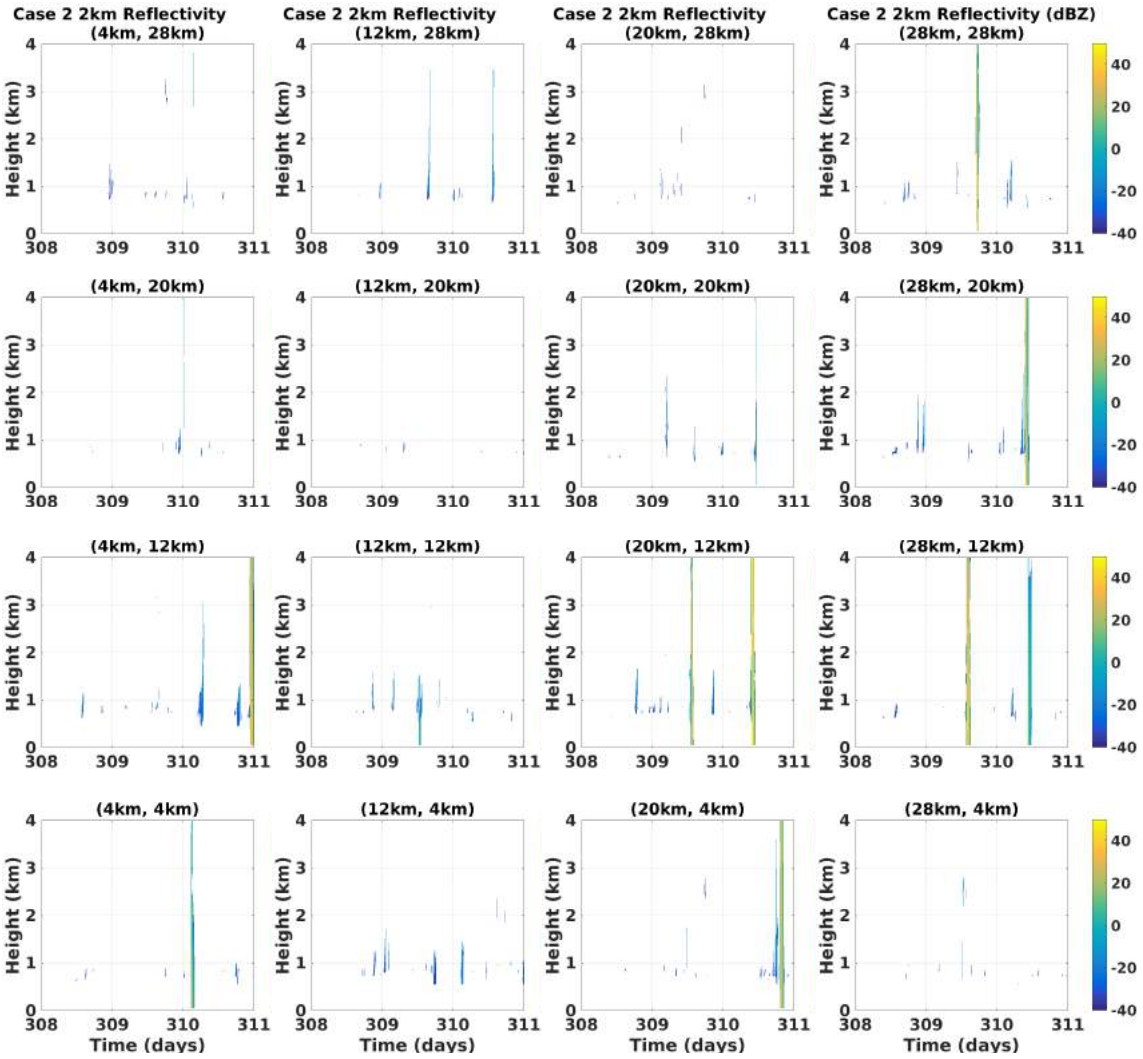

Figure 5.17. Time-height reflectivity from 16 evenly spaced points for the 2 km grid Case 2 model run.

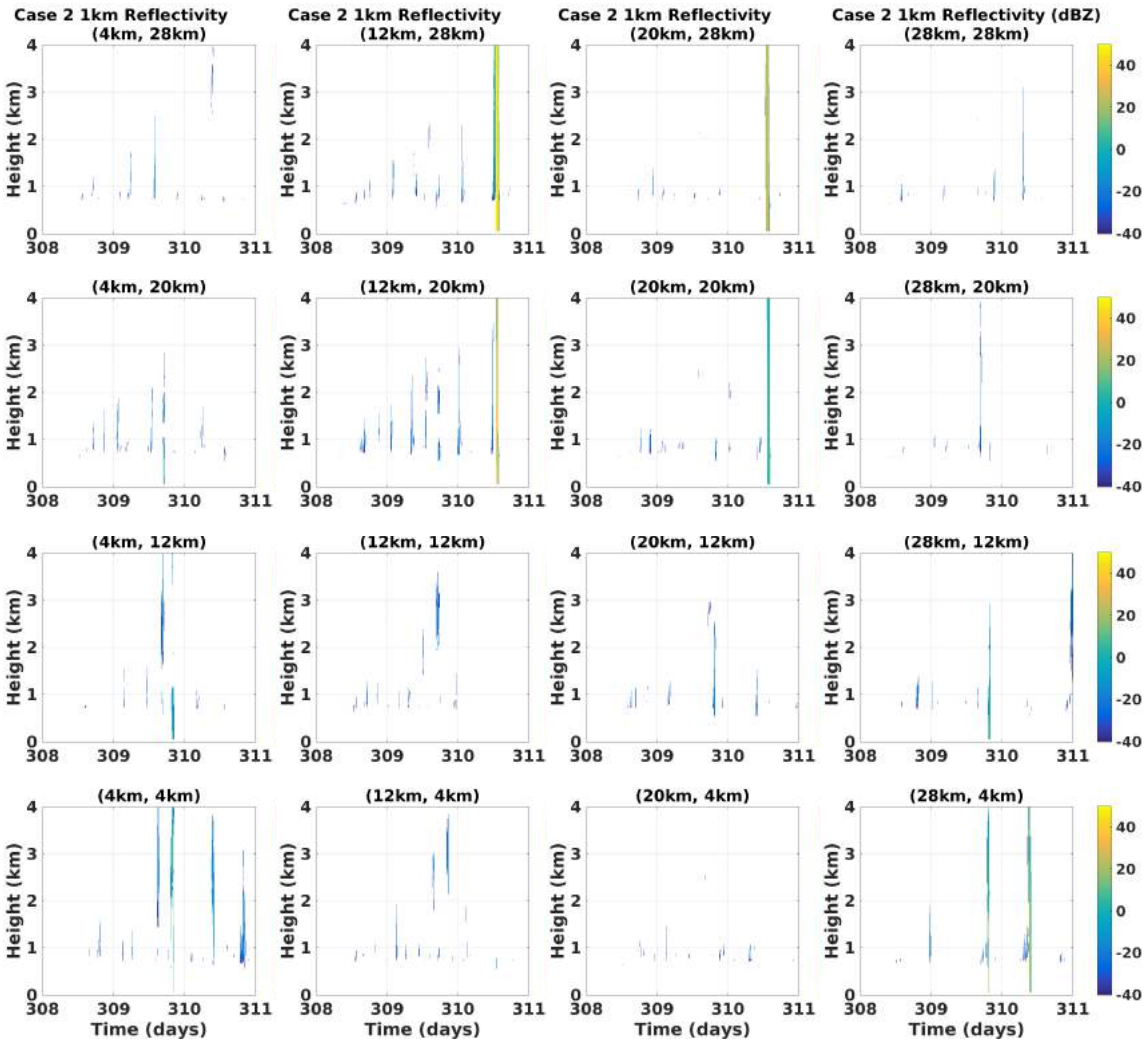

Figure 5.18. Time-height reflectivity from 16 evenly spaced points for the 1 km grid Case 2 model run.

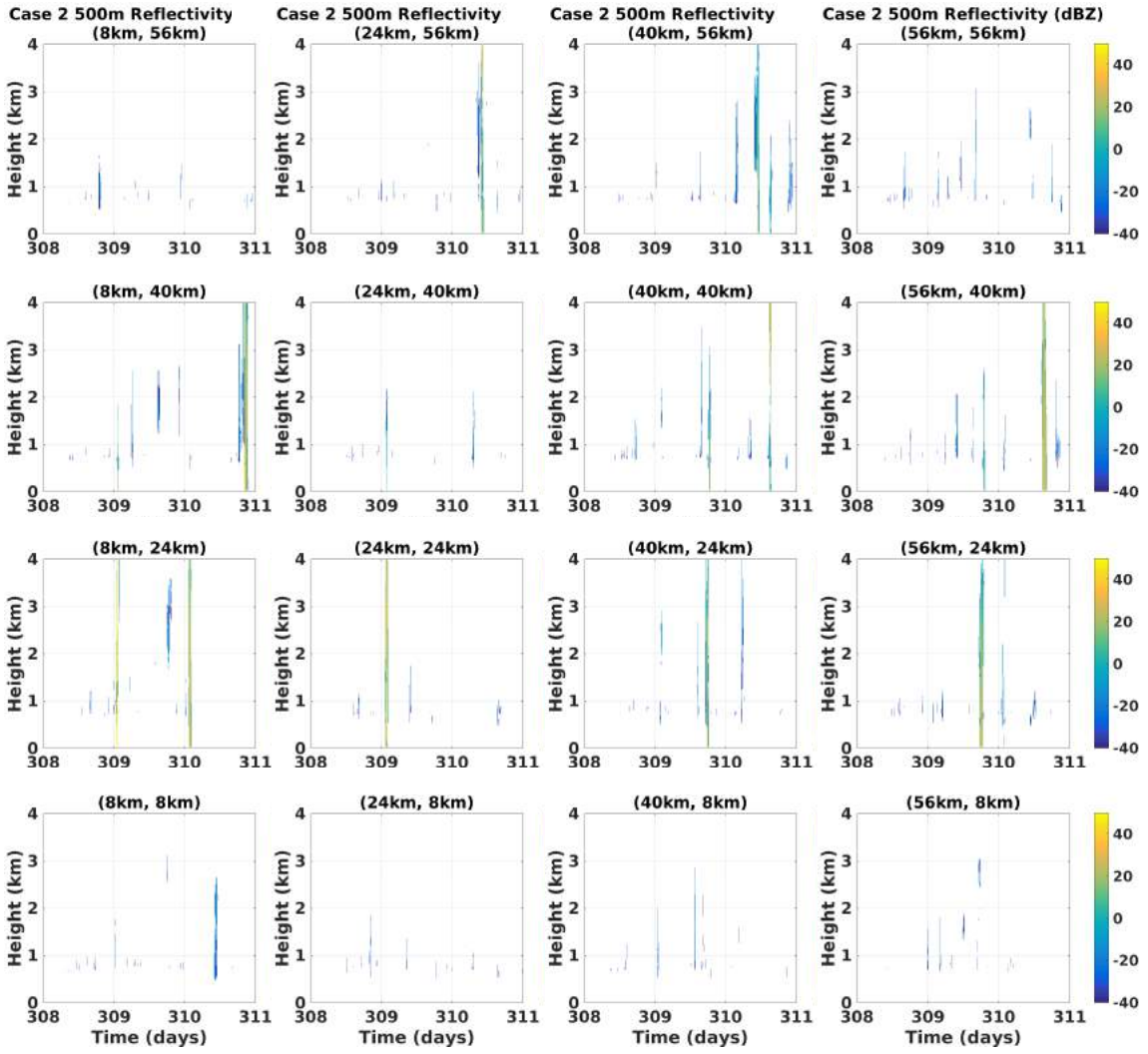

Figure 5.19. Time-height reflectivity from 16 evenly spaced points for the 0.5 km grid Case 2 model run.

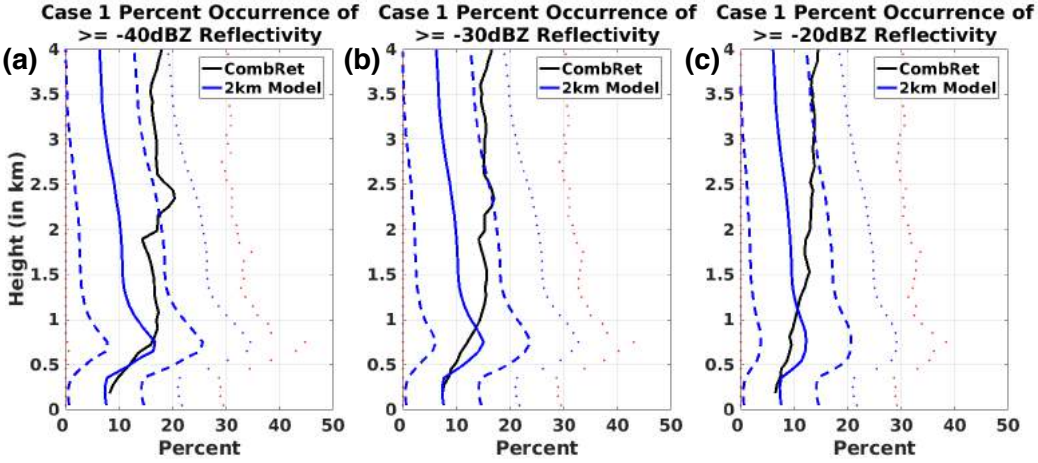

Figure 5.20. Reflectivity exceedance percentage (REP) profiles for the 2 km Case 1 CombRet (black line), model mean (blue line), model mean +- 1 standard deviation (blue dashes), model mean +- 2 standard deviations (blue dots), and model max/min (red dots) for a) -40 dBZ, b) -30 dBZ, and c) -20 dBZ minimum reflectivity thresholds.

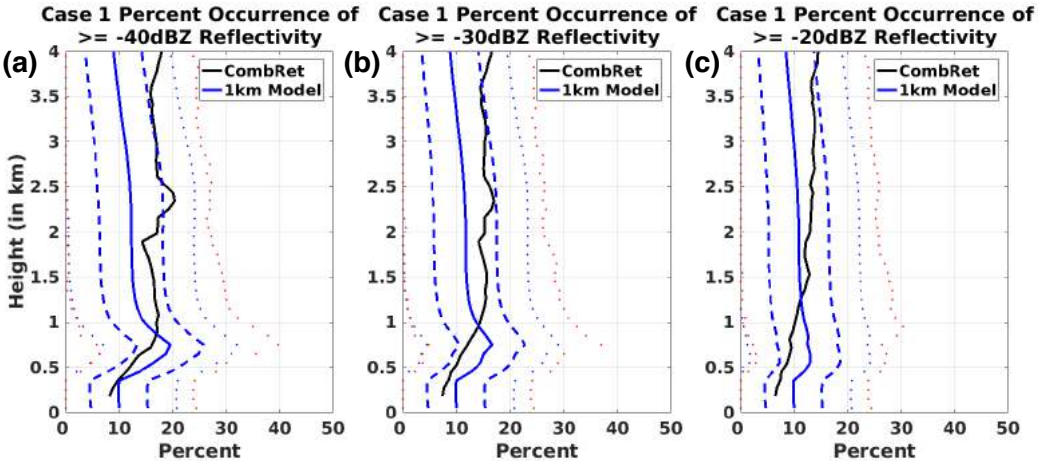

Figure 5.21. REP profiles for the 1 km Case 1 CombRet (black line), model mean (blue line), model mean +- 1 standard deviation (blue dashes), model mean +- 2 standard deviations (blue dots), and model max/min (red dots) for a) -40 dBZ, b) -30 dBZ, and c) -20 dBZ minimum reflectivity thresholds.

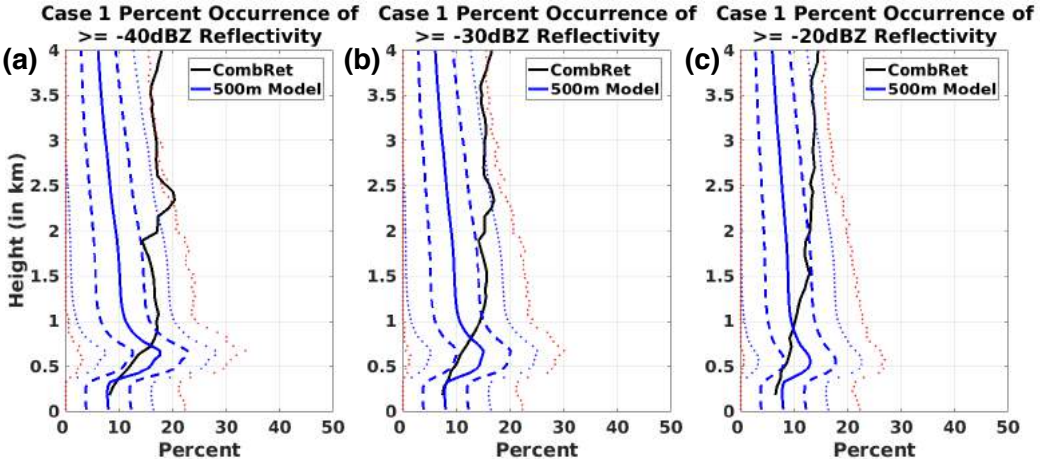

Figure 5.22. REP profiles for the 0.5 km Case 1 CombRet (black line), model mean (blue line), model mean +- 1 standard deviation (blue dashes), model mean +- 2 standard deviations (blue dots), and model max/min (red dots) for a) -40 dBZ, b) -30 dBZ, and c) -20 dBZ minimum reflectivity thresholds.

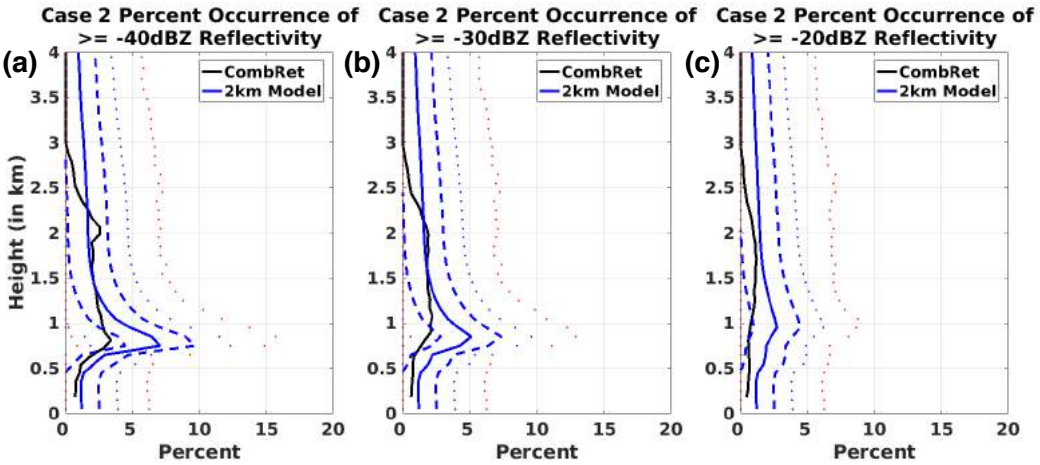

Figure 5.23. REP profiles for the 2 km Case 2 CombRet (black line), model mean (blue line), model mean +- 1 standard deviation (blue dashes), model mean +- 2 standard deviations (blue dots), and model max/min (red dots) for a) -40 dBZ, b) -30 dBZ, and c) -20 dBZ minimum reflectivity thresholds.

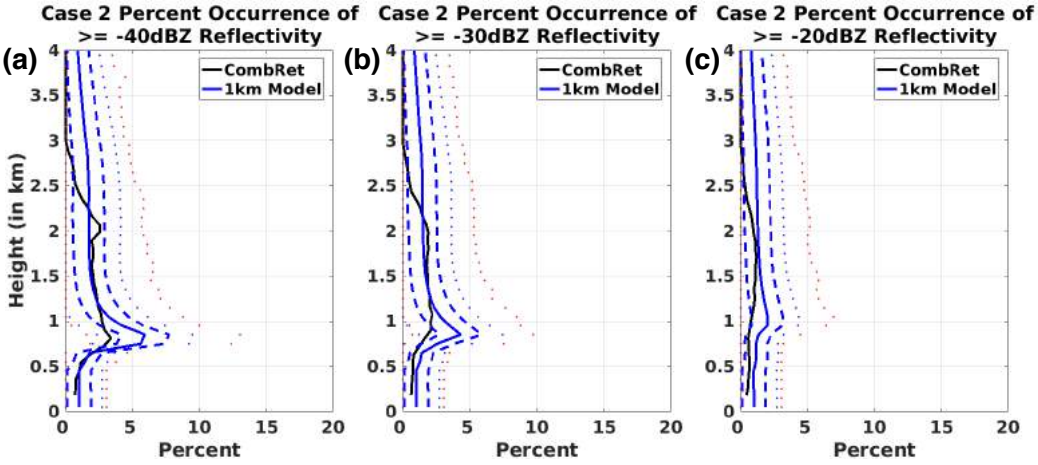

Figure 5.24. REP profiles for the 1 km Case 2 CombRet (black line), model mean (blue line), model mean +- 1 standard deviation (blue dashes), model mean +- 2 standard deviations (blue dots), and model max/min (red dots) for a) -40 dBZ, b) -30 dBZ, and c) -20 dBZ minimum reflectivity thresholds.

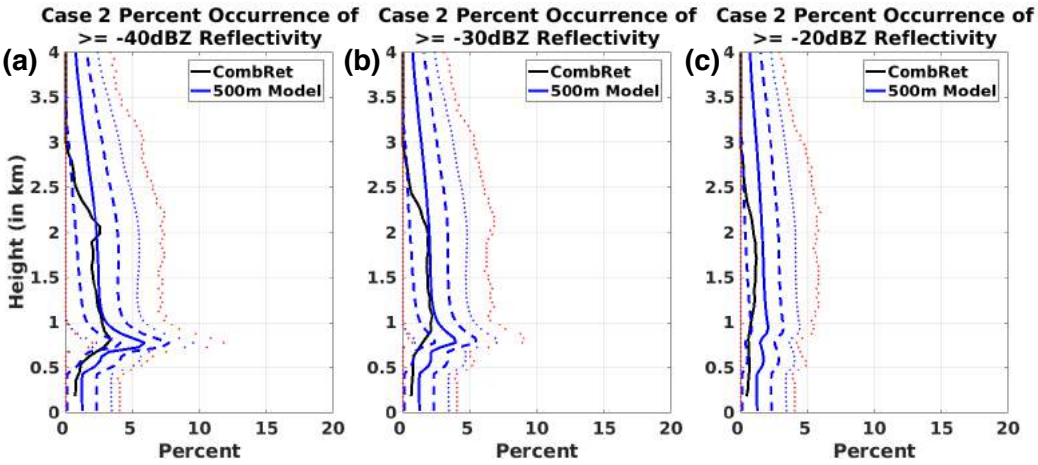

Figure 5.25. REP profiles for the 0.5 km Case 2 CombRet (black line), model mean (blue line), model mean +- 1 standard deviation (blue dashes), model mean +- 2 standard deviations (blue dots), and model max/min (red dots) for a) -40 dBZ, b) -30 dBZ, and c) -20 dBZ minimum reflectivity thresholds.

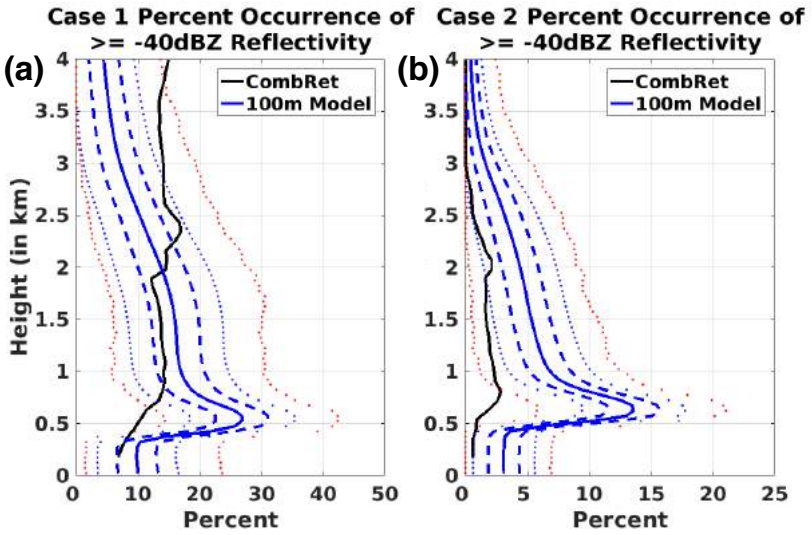

Figure 5.26. REP profiles for the 100 m CombRet (black line), model mean (blue line), model mean +- 1 standard deviation (blue dashes), model mean +- 2 standard deviations (blue dots), and model max/min (red dots) with a -40 dBZ minimum reflectivity threshold for a) Case 1 and b) Case 2.

CHAPTER 6

CONCLUSIONS

6.1 Overall Findings

The three studies, CONSTRAIN, RCE, and DYNAMO, sought to evaluate the dependence of cloud and precipitation variables on model changes such as turbulence parameterization scheme, microphysics scheme, SST, and grid spacing.

The CONSTRAIN case had only a few model combinations (no ice sedimentation and larger grid spacing SHOC full physics) which resulted in a steady transition from stratocumulus to cumulus similar to the observations that the case was based on. Most model configurations resulted in either rapid reductions in cloud fraction or near overcast conditions throughout the simulation. Connections were shown between ice sedimentation and cloud processes. For example, shutting off sedimentation led to reductions in precipitation, increases in clouds and increases in TKE and entrainment. The runs with the highest cloud water path were those with little to no ice water path, similar to conditions in the North Atlantic where supercooled water is common.

In RCE, 301 K SHOC runs with increasing grid sizes did not exhibit substantial changes in cloud water path and low cloud fraction, a result that would suggest little grid spacing dependence, except that this result was not duplicated by 305 K SHOC runs. Using cloud radiative kernels, net cloud feedback values were found to range from -0.36 W m^{-2} K^{-1} for 1M SHOC to +0.52 W m^{-2} K^{-1} for 1M NOSHOC. Other studies have found a net radiative feedback of 0.57 W m^{-2} K^{-1} globally for a doubling of CO_2 (Zelinka et al., 2012a) and a 0.20 ± 0.21 W m^{-2} K^{-1} interannual net radiative feedback for global cirrus clouds (Zhou et al., 2015).

For DYNAMO, cases of widespread shallow cumulus proved to be limited in number over Gan Island. Two cases were selected from over a month of data and were able to be reasonably simulated by SAM with grid spacings from 0.5 km to 2 km. The highest resolution model run overestimated shallow cumulus fraction in both cases.

Both the CONSTRAIN case and RCE had a strong cloud/ice water path dependence on the microphysics scheme. In CONSTRAIN, the double-moment microphysics run had virtually no cloud ice. In RCE, ice water path existed in the double-moment microphysics runs; however, it was at a much lower level than in the single-moment microphysics runs. It would appear that supercooled water is more frequent in diverse regions with double-moment microphysics rather than cloud ice generated in single-moment microphysics.

For the CONSTRAIN case, the LES model runs were considered to be truth for each set of runs varying by grid spacing, but for the DYNAMO case, the LES scale runs were the least successful at representing shallow cumulus.

One of the results in RCE was a decreasing low cloud fraction as grid size decreased. This was the case for all model combinations (SHOC/NOSHOC, 1M/2M, 301/305 K). On the other hand, DYNAMO had its highest shallow cumulus cloud fractions in the lowest grid spacing, 0.1 km. These results would suggest something else is at play yielding this result since both are tropical oceanic environments.

These three modeling studies looked at the grey zone range of model resolutions and in all three cases there were clearly superior and inferior model physics and grid size selections. The choice of parameterization scheme, microphysics scheme, and grid spacing will continue to be a significant part of the decision making process in atmospheric modeling.

6.2 Future Work

The CONSTRAIN case was done as part of an intercomparison project, on which a paper is currently being written by Stephan de Roode. Considering the results from SAM and SHOC and how models with complex microphysics in other studies (Morrison and Pinto, 2006; Klein et al., 2009) were better able to represent the supercooled liquid water that is prevalent in cold air outbreak events, a focus on double-moment microphysics schemes may be more successful at modeling the complicated mixed-phase cases as opposed to being the last option tested in this study. Additionally, the results with NOSHOC versus SHOC could use another higher latitude case study to further evaluate the capability of SHOC in handling this type of case.

In the RCE case, the effects of changes in domain size could be explored as another layer of comparison. Additionally, the change in sign of net cloud radiative feedback between

single-moment NOSHOC runs and SHOC runs with either microphysics scheme was an unexpected result. The varying sign of a net cloud radiative feedback in a cirrus dominated tropical RCE simulation leaves open the question of whether a global climate model would find a similar disparity in sign between various SHOC and microphysics setups. A global climate model based on the multiscale modeling framework (MMF) could potentially be used for this kind of assessment. This would also open up the possibility of more direct comparisons to the net cloud radiative feedback values in other kernel studies.

For DYNAMO, further exploration of larger grid spacings is worth looking into since the upper limit of model grid spacing leading to reasonable results does not appear to have been reached at 2 km in this study. Determining the cause of the LES simulations overestimating shallow cumulus is another important issue one could look at. Expanding beyond a focus on brief shallow cumulus events is also an option. Models have shown a tendency to underestimate the moistening during the suppressed convection phase which leads to the building up moisture in the congestus and deep convection phases (Del Genio et al., 2012). Analyzing the span from early in the suppressed period through to the deep convection phase with a variety of model physics setups could evaluate which perform better at properly moistening the atmosphere.

REFERENCES

ARM Climate Research Facility, 2011a: PNNL Combined Remote Sensor (gan2combret7fengM1) 2011-10-12 to 2011-10-15 and 2011-11-3 to 2011-11-7. ARM Mobile Facility (GAN) Gan Airport, Gan Island, Maldives, Atmospheric Radiation Measurement (ARM) Climate Research Facility Data Archive: Oak Ridge, Tennessee, USA. Data set accessed 26 April 2017.

ARM Climate Research Facility, 2011b: Total Sky Imager (TSISKYIMAGE) 2011-10-9 to 2011-12-7. ARM Mobile Facility (GAN) Gan Airport, Gan Island, Maldives; AMF2 (M1), Compiled by: V. Morris. Atmospheric Radiation Measurement (ARM) Climate Research Facility Data Archive: Oak Ridge, Tennessee, USA. Data set accessed 26 April 2017, doi:10.5439/1025309.

Avramov, A. and J. Y. Harrington, 2010: The influence of parameterized ice habit on simulated mixed-phase Arctic clouds. *J. Geophys. Res.*, **115**, D03205, doi:10.1029/2009JD012108.

Barnes, W. L., T. S. Pagano, and V. V. Salomonson, 1998: Prelaunch characteristics of the Moderate Resolution Imaging Spectroradiometer (MODIS) on EOS-AM1. *IEEE Trans. Geosci. Remote Sens.*, **36**, 1088–1100, doi:10.1109/36.700993.

Benedict, J. J. and D. A. Randall, 2007: Observed characteristics of the MJO relative to maximum rainfall. *J. Atmos. Sci.*, **64**, 2332–2354, doi:10.1175/JAS3968.1.

Bladé, I. and D. L. Hartmann, 1993: Tropical intraseasonal oscillations in a simple nonlinear model. *J. Atmos. Sci.*, **50**, 2922–2939, doi:10.1175/1520-0469(1993)050<2922:TIOIAS>2.0.CO;2.

Bogenschutz, P. A. and S. K. Krueger, 2013: A simplified PDF parameterization of subgrid-scale clouds and turbulence for cloud-resolving models. *J. Adv. Model. Earth Syst.*, **5**, 195–211., doi:10.1002/jame.20018.

Bogenschutz, P. A., S. K. Krueger, and M. Khairoutdinov, 2010: Assumed probability density functions for shallow and deep convection. *J. Adv. Model. Earth Syst.*, **2**, 24 pp., doi:10.3894/JAMES.2010.2.10.

Boutle, I. A., J. E. J. Eyre, and A. P. Lock, 2014: Seamless stratocumulus simulation across the turbulent gray zone. *Mon. Wea. Rev.*, **142**, 1655–1668., doi:10.1175/MWR-D-13-00229.1.

Bretherton, C. S., P. N. Blossey, and M. Khairoutdinov, 2005: An energy-balance analysis of deep convective self-aggregation above uniform SST. *J. Atmos. Sci.*, **62**, 4273–4292., doi:10.1175/JAS3614.1.

Bretherton, C. S., J. R. McCaa, and H. Grenier, 2004: A new parameterization for shallow cumulus convection and its application to marine subtropical cloud-topped

boundary layers. Part I: Description and 1D results. *Mon. Wea. Rev.*, **132**, 864–882., doi:10.1175/1520-0493(2004)132<0864:ANPFSC>2.0.CO;2.

Brown, A. R. and Coauthors, 2002: Large-eddy simulation of the diurnal cycle of shallow cumulus convection over land. *Quart. J. Roy. Meteor. Soc.*, **128**, 1075–1093., doi:10.1256/003590002320373210.

Brümmer, B., 1996: Boundary-layer modification in wintertime cold-air outbreaks from the Arctic sea ice. *Bound.-Layer Meteor.*, **80**, 109–125, doi:10.1007/BF00119014.

Brümmer, B., 1999: Roll and cell convection in wintertime Arctic cold-air outbreaks. *J. Atmos. Sci.*, **56**, 2613–2636, doi:10.1175/1520-0469(1999)056<2613:RACCIW>2.0.CO;2.

Brümmer, B. and S. Pohlmann, 2000: Wintertime roll and cell convection over Greenland and Barents Sea regions: A climatology. *J. Geophys. Res.*, **105(D12)**, 15559–15566, doi:10.1029/1999JD900841.

Burrows, S. M., C. Hoose, U. Pöschl, and M. G. Lawrence, 2013: Ice nuclei in marine air: Biogenic particles or dust?. *Atmos. Chem. Phys.*, **13**, 245–267, doi:10.5194/acp-13-245-2013.

Canuto, V. M., Y. Cheng, and A. Howard, 2001: New third-order moments for the convective boundary layer. *J. Atmos. Sci.*, **58**, 1169–1172., doi:10.1175/1520-0469(2001)058<1169:NTOMFT>2.0.CO;2.

Cess, R. D. and Coauthors, 1996: Cloud feedback in atmospheric general circulation models: An update. *J. Geophys. Res.*, **101**, 12791–12794., doi:10.1029/96JD00822.

Cheng, A., K.-M. Xu, and B. Stevens, 2010: Effects of resolution on the simulation of boundary-layer clouds and the partition of kinetic energy to subgrid scales. *J. Adv. Model. Earth Syst.*, **2**, 21 pp., doi:10.3894/JAMES.2010.2.3.

Chubb, H. T., J. B. Jensen, S. T. Siems, and M. J. Manton, 2013: In situ observations of supercooled liquid clouds over the Southern Ocean during the HIAPER Pole-to-Pole Observation (HIPPO) campaigns. *Geophys. Res. Lett.*, **40**, 5280–5285, doi:10.1002/grl.50986.

Clothiaux, E. E., T. P. Ackerman, G. G. Mace, K. P. Moran, R. T. Marchand, M. A. Miller, and B. E. Martner, 2000: Objective determination of cloud heights and radar reflectivity's using a combination of active remote sensors at the ARM CART sites. *J. Appl. Meteor.*, **39**, 645–665., doi:10.1175/1520-0450(2000)039<0645:ODOCHA>2.0.CO;2.

Clothiaux, E. E. and Coauthors, 2001: The ARM millimeter wave cloud radars (MMCRs) and the active remote sensing of clouds (ARSCL) value added product (VAP). Tech. rep., DOE Tech. Memo, ARM VAP-002.1, 38 pp. doi: www.arm.gov/publications/tech_reports/arm-vap-002-1.pdf.

Collins, W. D. and Coauthors, 2004: Description of the NCAR Community Atmospheric Model (CAM 3.0). Tech. rep., NCAR Tech. Note, Note NCAR/TN-464+STR, 226 pp. doi:10.5065/D63N21CH.

Comstock, J. M., A. Protat, S. A. McFarlane, J. Delanoë, and M. Deng, 2013: Assessment of uncertainty in cloud radiative effects and heating rates through retrieval algorithm differences: Analysis using 3-years of ARM data at Darwin, Australia. *J. Geophys. Res.*, **118**, 4549–4571., doi:10.1002/jgrd.50404.

de Szoeke, S. P., J. B. Edson, J. R. Marion, C. W. Fairall, and L. Bariteau, 2015: The MJO and air-sea interaction in TOGA COARE and DYNAMO. *J. Climate*, **28**, 597–622., doi:10.1175/JCLI-D-14-00477.1.

Del Genio, A. D., Y. Chen, D. Kim, and M.-S. Yao, 2012: The MJO transition from shallow to deep convection in CloudSat/CALIPSO data and GISS GCM simulations. *J. Climate*, **25**, 3755–3770, doi:10.1175/JCLI-D-11-00384.1.

Deng, M. and Coauthors, 2014: Stratiform and convective precipitation observed by multiple radars during the DYNAMO/AMIE experiment. *J. Appl. Meteor. Climatol.*, **53**, 2503–2523., doi:10.1175/JAMC-D-13-0311.1.

Feng, Z., X. Dong, and B. Xi, 2009: A method to merge WSR-88D data with ARM SGP millimeter cloud radar data by studying deep convective systems. *J. Atmos. Oceanic Technol.*, **26**, 958–971, doi:10.1175/2008JTECHA1190.1.

Feng, Z., S. McFarlane, C. Schumacher, S. Ellis, J. Comstock, and N. Bharadwaj, 2014: Constructing a merged cloud-precipitation radar dataset for tropical convective clouds during the DYNAMO/AMIE experiment at Addu Atoll. *J. Atmos. Oceanic Technol.*, **31**, 1021–1042, doi:10.1175/JTECH-D-13-00132.1.

Field, P. R., R. J. Cotton, K. McBeath, A. P. Lock, S. Webster, and R. P. Allan, 2014: Improving a convection-permitting model simulation of a cold air outbreak. *J. Atmos. Sci.*, **140**, 124–138., doi:10.1002/qj.2116.

Fletcher, J., S. Mason, and C. Jakob, 2016a: The climatology, meteorology, and boundary layer structure of marine cold air outbreaks in both hemispheres. *J. Climate*, **29**, 1999–2014., doi:10.1175/JCLI-D-15-0268.1.

Fletcher, J., S. Mason, and C. Jakob, 2016b: A climatology of clouds in marine cold air outbreaks in both hemispheres. *J. Climate*, **29**, 6677–6692., doi:10.1175/JCLI-D-15-0783.1.

Fu, Q. and K. N. Liou, 1992: On the correlated *k*-distribution method for radiative transfer in nonhomogeneous atmospheres. *J. Atmos. Sci.*, **49**, 2139–2156., doi:10.1175/1520-0469(1992)049<2139:OTCDMF>2.0.CO;2.

Fu, Q. and K. N. Liou, 1993: Parameterization of the radiative properties of cirrus clouds. *J. Atmos. Sci.*, **50**, 2008–2025., doi:10.1175/1520-0469(1993)050<2008:POTRPO>2.0.CO;2.

Golaz, J. C., V. E. Larson, and W. R. Cotton, 2002a: A PDF-based model for boundary layer clouds. Part I: Method and model description. *J. Atmos. Sci.*, **59**, 3540–3551., doi:10.1175/1520-0469(2002)059<3540:APBMFB>2.0.CO;2.

Golaz, J. C., V. E. Larson, and W. R. Cotton, 2002b: A PDF-based model for boundary layer clouds. Part II: Model results. *J. Atmos. Sci.*, **59**, 3552–3571., doi:10.1175/1520-0469(2002)059<3552:APBMFB>2.0.CO;2.

Grabowski, W. W., 2001: Coupling cloud processes with the large-scale dynamics using the Cloud-Resolving Convection Parameterization. *J. Atmos. Sci.*, **58**, 978–997., doi:10.1175/1520-0469(2001)058<0978:CCPWTL>2.0.CO;2.

Hannah, W. M., B. E. Mapes, and G. S. Elsaesser, 2016: A Lagrangian view of moisture dynamics during DYNAMO. *J. Atmos. Sci.*, **73**, 1967–1985., doi:10.1175/JAS-D-15-0243.1.

Harrington, J. Y., T. Reisin, W. R. Cotton, and S. M. Kreidenweis, 1999: Cloud resolving simulations of Arctic stratus Part II: Transition-season clouds. *Atmos. Res.*, **51**, 45–75., doi:10.1016/S0169-8095(98)00098-2.

Hartmann, D. L. and K. Larson, 2002: An important constraint on tropical cloud-climate feedback. *Geophys. Res. Lett.*, **29**, 1951., doi:10.1029/2002GL015835.

Hartmann, D. L., L. A. Moy, and Q. Fu, 2001: Tropical convection and the energy balance at the top of the atmosphere. *J. Climate*, **14**, 4495–4511., doi:10.1175/1520-0442(2001)014<4495:TCATEB>2.0.CO;2.

Hobbs, P. V. and A. L. Rangno, 1998: Microstructures of low and middle-level clouds over the Beaufort Sea. *Q. J. R. Meteorol. Soc.*, **124**, 2035–2071., doi: 10.1002/qj.49712455012.

Huang, Y., S. T. Siems, M. J. Manton, and G. Thompson, 2014: An evaluation of WRF simulations of clouds over the Southern Ocean with A-Train observations. *Mon. Wea. Rev.*, **142**, 647–667., doi:10.1175/MWR-D-13-00128.1.

Hubbert, J. C., M. Dixon, and S. M. Ellis, 2009a: Weather radar ground clutter. Part II: Real-time identification and filtering. *J. Atmos. Oceanic Technol.*, **26**, 1181–1197., doi:10.1175/2009JTECHA1160.1.

Hubbert, J. C., M. Dixon, S. M. Ellis, and G. Meymaris, 2009b: Weather radar ground clutter. Part I: Identification, modeling, and simulation. *J. Atmos. Oceanic Technol.*, **26**, 1165–1180., doi:10.1175/2009JTECHA1159.1.

Iacono, M. J., J. S. Delamere, E. J. Mlawer, M. W. Shephard, S. A. Clough, and W. D. Collins, 2008: Radiative forcing by long-lived greenhouse gases: Calculations with the AER radiative transfer models. *J. Geophys. Res.*, **113**, D13103, doi: 10.1029/2008JD009944.

Jeevanjee, N. and D. M. Romps, 2013: Convective self-aggregation, cold pools, and domain size. *Geophys. Res. Lett.*, **40**, 994–998, doi:10.1002/grl.50204.

Johnson, R. H. and P. E. Ciesielski, 2013: Structure and properties of Madden-Julian oscillations deduced from DYNAMO sounding arrays. *J. Atmos. Sci.*, **70**, 3157–3179., doi:10.1175/JAS-D-13-065.1.

Johnson, R. H., P. E. Ciesielski, J. H. Ruppert Jr., and M. Katsumata, 2015: Sounding-based thermodynamic budgets for DYNAMO. *J. Atmos. Sci.*, **72**, 598–622., doi: 10.1175/JAS-D-14-0202.1.

Keeler, J. R., J. Lutz, and J. Vivekanandan, 2000: S-Pol: NCAR's polarimetric Doppler research radar. *IGARS 2000: IEEE 2000 International Geoscience and Remote Sensing Symposium.*, **4**, 1570–1573., doi:10.1109/IGARSS.2000.857275.

Khairoutdinov, M. and Y. L. Kogan, 1999: A large-eddy simulation model with explicit microphysics: Validation against aircraft observations of a stratocumulus-topped boundary layer. *J. Atmos. Sci.*, **56**, 2115–2131., doi:10.1175/1520-0469(1999)056<2115:ALESMW>2.0.CO;2.

Khairoutdinov, M. and Y. L. Kogan, 2000: A new cloud physics parameterization in a large-eddy simulation model of marine stratocumulus. *Mon. Wea. Rev.*, **128**, 229–243., doi:10.1175/1520-0493(2000)128<0229:ANCPPI>2.0.CO;2.

Khairoutdinov, M. and D. Randall, 2003: Cloud resolving modeling of the ARM summer 1997 IOP: Model formulations, results, uncertainties, and sensitivities. *J. Atmos. Sci.*, **60**, 607–625., doi:10.1175/1520-0469(2003)060<0607:CRMOTA>2.0.CO;2.

Kiehl, J. T., J. J. Hack, G. B. Bonan, B. A. Boville, D. L. Williamson, and P. J. Rasch, 1998: The National Center for Atmospheric Research Community Climate Model: CCM3. *J. Climate*, **11**, 1131–1149., doi:10.1175/1520-0442(1998)011<1131:TNCFAR>2.0.CO;2.

Klein, S. A. and C. Jakob, 1999: Validation and sensitivities of frontal clouds simulated by ECMWF model. *Mon. Wea. Rev.*, **127**, 2514–2531., doi:10.1175/1520-0493(1999)127<2514:VASOFC>2.0.CO;2.

Klein, S. A. and Coauthors, 2009: Intercomparison of model simulations of mixed-phase clouds observed during the ARM Mixed-Phase Arctic Cloud Experiment. I: Single-layer cloud. *Q. J. R. Meteorol. Soc.*, **135**, 979–1002., doi:10.1002/qj.416.

Kollias, P., B. A. Albrecht, E. E. Clothiaux, M. A. Miller, K. L. Johnson, and K. P. Moran, 2005: The Atmospheric Radiation Measurement Program cloud profiling radars: An evaluation of signal processing and sampling strategies. *J. Atmos. Oceanic Technol.*, **22**, 930–948., doi:10.1175/JTECH1749.1.

Kollias, P. and Coauthors, 2016: Development and applications of ARM millimeter-wavelength cloud radars. *The Atmospheric Radiation Measurement (ARM) Program: The First 20 Years, Meteor. Monogr.*, No. 57, Amer. Meteor. Soc., doi: 10.1175/AMSMONOGRAPHS-D-15-0037.1.

Krueger, S. K., 1988: Numerical simulation of tropical cumulus clouds and their interaction with the subcloud layer. *J. Atmos. Sci.*, **45**, 2221–2250., doi:10.1175/1520-0469(1988)045<2221:NSOTCC>2.0.CO;2.

Krueger, S. K., H. Morrison, and A. M. Fridlind, 2016: Cloud-resolving modeling: ARM and the GCSS story. *Meteorol. Monogr.*, **57**, 25.1–25.16., doi: 10.1175/AMSMONOGRAPHS-D-15-0047.1.

Kuang, Z. and D. L. Hartmann, 2007: Testing the fixed anvil temperature hypothesis in a cloud-resolving model. *J. Climate*, **20**, 2051–2057., doi:10.1175/JCLI4124.1.

Larson, V. E., J.-C. Golaz, and W. R. Cotton, 2002: Small-scale and mesoscale variability in cloudy boundary layers: Joint probability density functions. *J. Atmos. Sci.*, **59**, 3519–3539., doi:10.1175/1520-0469(2002)059<3519:SSAMVI>2.0.CO;2.

Lin, R.-F., D. Starr, P. J. DeMott, R. Cotton, K. Sassen, E. Jensen, B. Kärcher, and X. Liu, 2002: Cirrus parcel model comparison project. Phase 1: The critical components to simulate cirrus initiation explicitly. *J. Atmos. Sci.*, **59**, 2305–2319., doi:10.1175/1520-0469(2002)059¡2305:CPMCPP¿2.0.CO;2.

Madden, R. A. and P. R. Julian, 1972: Description of global-scale circulation cells in the tropics with a 40-50 day period. *J. Atmos. Sci.*, **29**, 1109–1123., doi:10.1175/1520-0469(1972)029<1109:DOGSCC>2.0.CO;2.

Manabe, S. and R. F. Strickler, 1964: Thermal equilibrium of the atmosphere with a convective adjustment. *J. Atmos. Sci.*, **21**, 361–385., doi:10.1175/1520-0469(1964)021<0361:TEOTAW>2.0.CO;2.

Manabe, S. and R. T. Wetherald, 1967: Thermal equilibrium of the atmosphere with a given distribution of relative humidity. *J. Atmos. Sci.*, **24**, 241–259., doi:10.1175/1520-0469(1967)024<0241:TEOTAW>2.0.CO;2.

Martin, G. M., D. W. Johnson, and A. Spice, 1994: The measurement and parameterization of effective radius of droplets in warm stratocumulus clouds. *J. Atmos. Sci.*, **51**, 1823–1842., doi:10.1175/1520-0469(1994)051<1823:TMAPOE>2.0.CO;2.

McBeath, K., P. R. Field, and R. J. Cotton, 2014: Using operational weather radar to assess high-resolution numerical weather prediction over the British Isles for a cold air outbreak case-study. *Q. J. R. Meteorol. Soc.*, **140**, 225–239., doi:10.1002/qj.2123.

Mlawer, E. J., S. J. Taubman, P. D. Brown, M. J. Iacono, and S. A. Clough, 1997: Radiative transfer for inhomogeneous atmosphere: RRTM, a validated correlated-*k* model for the longwave. *J. Geophys. Res.*, **102**, 16663–16682., doi:10.1029/97JD00237.

Morris, V. R., 2005: Total Sky Imager (TSI) handbook. ARM TR-017, doi:Available at http://www.arm.gov/publications/tech_reports/handbooks/tsi_handbook.pdf.

Morrison, A. E., S. T. Siems, and M. J. Manton, 2011: A three-year climatology of cloud-top phase over the Southern Ocean and North Pacific. *J. Climate*, **24**, 2405–2418., doi:10.1175/2010JCLI3842.1.

Morrison, H., J. A. Curry, and V. I. Khvorostyanov, 2005: A new double-moment microphysics parameterization for application in cloud and climate models. Part I: Description. *J. Atmos. Sci.*, **62**, 1665–1677., doi:10.1175/JAS3446.1.

Morrison, H. and J. O. Pinto, 2006: Intercomparison of bulk cloud microphysics schemes in mesoscale simulations of springtime Arctic mixed-phase stratiform clouds. *Mon. Wea. Rev.*, **134**, 1880–1900., doi:10.1175/MWR3154.1.

Morrison, H., G. Thompson, and V. Tatarskii, 2009: Impact of cloud microphysics on the development of trailing stratiform precipitation in a simulated squall line: Comparison of One- and Two-Moment schemes. *Mon. Wea. Rev.*, **137**, 991–1007., doi:10.1175/2008MWR2556.1.

Muller, C. J. and I. M. Held, 2012: Detailed investigation of the self-aggregation of convection in cloud-resolving simulations. *J. Atmos. Sci.*, **69**, 2551–2565., doi: 10.1175/JAS-D-11-0257.1.

Myhre, G. and Coauthors, 2013: Anthropogenic and natural radiative forcing. *Climate Change 2013: The Physical Science Basis. Contribution of Working Group I to the Fifth Assessment Report of the Intergovernmental Panel on Climate Change*, T. F. Stocker, D. Qin, G.-K. Plattner, M. Tignor, S. K. Allen, J. Boschung, A. Nauels, Y. Xia, V. Bex, and P. M. Midgley (eds.), Cambridge University Press, Cambridge, United Kingdom and New York, NY, USA.

Pielke, R. A., 1974: A three-dimensional numerical model of the sea breezes over South Florida. *Mon. Wea. Rev.*, **102**, 115–139., doi:10.1175/1520-0493(1974)102<0115:ATDNMO>2.0.CO;2.

Randall, D. A., M. Khairoutdinov, A. Arakawa, and W. Grabowski, 2003: Breaking the cloud-parameterization deadlock. *Bul. Amer. Meteor. Soc.*, **84**, 1547–1564., doi: 10.1175/BAMS-84-11-1547.

Redelsperger, J. L. and G. Sommeria, 1986: Three-dimensional simulation of a convective storm: Sensitivity studies on subgrid parameterization and spatial resolution. *J. Atmos. Sci.*, **43**, 2619–2635., doi:10.1175/1520-0469(1986)043<2619:TDSOAC>2.0.CO;2.

Reed, K. A., B. Medeiros, J. T. Bacmeister, and P. H. Lauritzen, 2015: Global radiative-convective equilibrium in the Community Atmosphere Model, Version 5. *J. Atmos. Sci.*, **72**, 2183–2197., doi:10.1175/JAS-D-14-0268.1.

Reynolds, R. W., 2009: What's new in version 2. Tech. rep., NOAA/NCDC Rep., 10 pp. doi:www.ncdc.noaa.gov/sites/default/files/attachments/Reynolds2009_oisst_daily_v02r00_version2-features.pdf.

Reynolds, R. W., T. M. Smith, C. Liu, D. B. Chelton, K. S. Casey, and M. G. Schlax, 2007: Daily high-resolution-blended analyses for sea surface temperature. *J. Climate*, **20**, 5473–5496., doi:10.1175/2007JCLI1824.1.

Shin, H. H. and S.-Y. Hong, 2015: Representation of the subgrid-scale turbulent transport in convective boundary layers at gray-zone resolutions. *Mon. Wea. Rev.*, **143**, 250–271., doi:10.1175/MWR-D-14-00116.1.

Silvers, L. G., B. Stevens, T. Mauritsen, and M. Giorgetta, 2016: Radiative convective equilibrium as a framework for studying the interaction between convection and its large-scale environment. *J. Adv. Model. Earth Syst.*, **8**, 15 pp., doi: 10.1002/2016MS000629.

Smith, P. L., 1984: Equivalent radar reflectivity factors for snow and ice particles. *J. Climate Appl. Meteor.*, **23**, 1258–1260., doi:10.1175/1520-0450(1984)023<1258:ERRFFS>2.0.CO;2.

Smolarkiewicz, P. K. and W. W. Grabowski, 1990: The multi-dimensional positive definite advection transport algorithm: Non-oscillatory option. *J. Comput. Phys.*, **86**, 355–375., doi:10.1016/0021-9991(90)90105-A.

Soden, B. J., I. M. Held, R. Colman, K. M. Shell, J. T. Kiehl, and C. A. Shields, 2008: Quantifying climate feedbacks using radiative kernals. *J. Climate*, **21**, 3504–3520., doi: 10.1175/2007JCLI2110.1.

Sohlberg, R., J. Descloitres, and T. Bobbe, 2001: MODIS Land Rapid Response: operational use of Terra data for USFS wildlife management. *Earth Obs.*, **13**, 8–10., doi:https://eospso.gsfc.nasa.gov/sites/default/files/eo_pdfs/Sept_Oct01.pdf.

Stanford, M. W., 2016: Evaluation of simulated tropical convective updraft hydrometeor properties using aircraft observations. *Thesis, Department of Atmospheric Sciences, University of Utah, Salt Lake City.*, 101 pp.

Sun, Y., L. Yi, Z. Zhong, and Y. Ha, 2014: Performance of a new convective parameterization scheme on model convergence in simulations of a tropical cyclone at grey-zone resolutions. *J. Atmos. Sci.*, **71**, 2078–2088., doi:10.1175/JAS-D-13-0285.1.

Teixeira, J. and S. Cheinet, 2004: A simple mixing length formulation for the eddy-diffusivity parameterization of dry convection. *Bound.-Layer Meteor.*, **110**, 435–453., doi:10.1023/B:BOUN.0000007230.96303.0d.

UCAR/NCAR - Earth Observing Laboratory, 2012: METEOSAT7 Ch1 Visible Satellite Imagery. Version 1.0., UCAR/NCAR - Earth Observing Laboratory., https://data.eol.ucar.edu/dataset/347.061. Data set accessed 26 January 2017.

Varble, A. C., 2013: Using Tropical Warm Pool-International Cloud Experiment observations to evaluate and improve high resolution simulations of tropical convective precipitation systems. *Dissertation, Department of Atmospheric Sciences, University of Utah, Salt Lake City.*, 239 pp.

Wang, S., A. H. Sobel, F. Zhang, Y. Q. Sun, Y. Yue, and L. Zhou, 2015: Regional simulation of the October and November MJO events during the CINDY/DYNAMO field campaign at gray zone resolution. *J. Climate.*, **28**, 2097–2119., doi:10.1175/JCLI-D-14-00294.1.

Xie, S., et al., 2005: Simulations of midlatitude frontal clouds by single-column and cloud-resolving models during the Atmospheric Radiation Measurement March 2000 cloud intensive operational period. *J. Geophys. Res.*, **110**, D15S03., doi: 10.1029/2004JD005119.

Xu, K.-M. and Coauthors, 2002: An intercomparison of cloud-resolving models with the Atmospheric Radiation Measurement summer 1997 Intensive Observation Period data. *Quart. J. Roy. Meteor. Soc.*, **128**, 593–624., doi:10.1256/003590002321042117.

Yamada, T. and G. Mellor, 1975: A simulation of the Wangara atmospheric boundary layer data. *J. Atmos. Sci.*, **32**, 2309–2329., doi:10.1175/1520-0469(1975)032<2309:ASOTWA>2.0.CO;2.

Zelinka, M. D., S. A. Klein, and D. L. Hartmann, 2012a: Computing and partitioning cloud feedbacks using cloud property histograms. Part I: Cloud radiative kernels. *J. Climate*, **25**, 3715–3735., doi:10.1175/JCLI-D-11-00248.1.

Zelinka, M. D., S. A. Klein, and D. L. Hartmann, 2012b: Computing and partitioning cloud feedbacks using cloud property histograms. Part II: Attribution to changes in cloud amount, altitude, and optical depth. *J. Climate*, **25**, 3736–3754., doi:10.1175/JCLI-D-11-00249.1.

Zhang, M. H. and J. L. Lin, 1997: Constrained variational analysis of sounding data based on column-integrated conservations of mass, heat, moisture, and momentum: Approach and application to ARM measurements. *J. Atmos. Sci.*, **54**, 1503–1524., doi:10.1175/1520-0469(1997)054<1503:CVAOSD>2.0.CO;2.

Zhang, M. H., J. L. Lin, R. T. Cederwall, J. J. Yio, and S. C. Xie, 2001: Objective analysis of ARM IOP data: Method and sensitivity. *Mon. Wea. Rev.*, **129**, 295–311., doi:10.1175/1520-0493(2001)129<0295:OAOAID>2.0.CO;2.

Zhao, C. and Coauthors, 2012: Toward understanding of differences in current cloud retrievals of ARM ground-based measurements. *J. Geophys. Res.*, **117**, D10 206, doi:10.1029/2011JD016792.

Zhou, C., A. E. Dessler, M. D. Zelinka, P. Yang, and T. Wang, 2015: Cirrus feedback on interannual climate fluctuations. *Geophys. Res. Lett.*, **41**, 9166–9173., doi:10.1002/2014GL062095.

Zhou, C., M. D. Zelinka, A. E. Dessler, and P. Yang, 2013: An analysis of the short-term cloud feedback using MODIS data. *J. Climate*, **26**, 4803–4815., doi:10.1175/JCLI-D-12-00547.1.